Universitat Autònoma de Barcelona

La doble vessant del dany per radiació: de les estratègies per a reduir-lo al seu ús en l'estudi de l'Aldosa Reductasa en condicions d'estrès oxidatiu

ALBERT CASTELLVÍ TOLEDO

Universitat Autònoma de Barcelona

La doble vessant del dany per radiació: de les estratègies per a reduir-lo al seu ús en l'estudi de l'Aldosa Reductasa en condicions d'estrès oxidatiu

Memòria presentada per

ALBERT CASTELLVÍ TOLEDO

Llicenciat en Física,

per a optar al Grau de Doctor en Bioquímica, Biologia Molecular i Biomedicina

Treball realitzat al Sincrotró ALBA, sota la direcció de la Doctora

JUDITH JUANHUIX GIBERT

Judith Juanhuix Gibert **Albert Castellví Toledo**

Bellaterra, 12 de Març de 2019

A l'Olga, en Lluc i en Guim

Agraïments

Aquests darrers anys han sigut apassionants treballant a ALBA. De debò. He gaudit moltíssim de la ciència i de la gent que corre per aquí. Per això, en primer lloc, haig de donar les gràcies a la Judith Juanhuix, per haver-me donat l'oportunitat de gaudir d'aquesta experiència i per la confiança que sempre ha d**E**positat en mi. Moltes gràcies, Jefa! Ha sigut un autèntic plaer poder treballar al teu costat.

En segundo lugar debo de dar las gracias a Jo**Z**é A. Gavira (Pisha!) y a Ana Cámara-Artigas por haberme ayudado TANTO. Qué paliza os he pegado a lo largo de este tiempo! Siempre habéis tenido la respuesta adecuada y, de manera increíblemente generosa, me habéis permitido aprender un montón de vosotros. Gracias de nuevo! Os seguiré dando la brasa! ;)

També, al *Radiation Damage team*. A l'Eva Crosas i a l'Isidro Crespo, per la feina feta conjuntament i pels bons moments plegats (Déu ni do eh?). Gràcies Eva, seria brutal poder tornar a treballar amb tu. Gràcies Isidro, per haver-me ensenyat tota la bioquímica que sé, ets un *crack*!

A la gent de la oficina, que sense l'ambient brutal que hi ha, això hauria sigut una mica més feixuc. A en Harold Moreno (casi debería de citarte en los "Desagradecimientos", por tanto tiempo útil perdido con tigo riendo como un loco, parsero!), a la Laia Torres (algun dia aconseguiràs la taula dels deus somnis, XD!), a l'Isidro Crespo, a l'Anna Mandziak i a en Daniel Ruano. A la gent amb la que he tingut el plaer de compartir el laboratori de biologia: Nerea Bernardo (epa!), Anna Cuppari (estás loca), Anabel Alonso, Cristina Sánchez, Carla Prats, Mari Carmen, Alba Descarga, Carla Segura, Robert Oliete, Tibisay Guevara (hola Tibi!!)... A la gent de MX: Daniel Fullà (fonamental!!), Xavi Carpena (pagesot!), Bárbara Machado, Fernando Gil, Roeland Boer i Damià Garriga. A en Marc Malfois, pels beamtimes a NCD-SWEET. A en Miguel A. G. Aranda, per la seva iniciativa i persistència en l'inici del projecte. A en Manel Sabés i a l'Inmaculada Ramos, per l'interès constant que han mostrat per mi. A tota la gent d'ALBA que, d'alguna manera o altre, m'han ajudat al llarg dels 7 anys que ja porto rondant per aquí y que no m'arrisco a citar una per una . Sento fer servir aquest truc, no m'agradaria deixar-me a ningú...

Als meus pares que, evidentment, sense l'ajuda constant per part d'ells no hauria pogut fer el que he fet.

I per últim, a l'Olga Mingo i als meus dos nens, en Lluc Castellví i en Guim Castellví. Per la infinita paciència i amor que han tingut cap a mi. Us estimo moltíssim! Seguim!

GRÀCIES a tothom, de tot cor.

Resum

En aquest treball el terme *dany per radiació*, aplicat a sistemes biològics macromoleculars, fa referència a totes les modificacions, tant estructurals com químiques, induïdes pels raigs X en interaccionar amb la mostra experimental.

En aquesta Tesi s'ha estudiat el dany per radiació en diferents sistemes biològics macromoleculars en dues vessants oposades. Per una banda, s'han caracteritzat diversos compostos *scavenger* nous, que poden ser útils per reduir els efectes del dany per radiació en experiments de cristal·lografia de proteïnes i dispersió de raigs X a angles baixos. Per altra banda, els mateixos efectes provocats pel dany per radicació s'han fet servir per a simular, de manera controlada, condicions d'estrès oxidatiu.

Els resultats obtinguts en aquesta Tesi s'han distribuït en quatre capítols diferents. En el Capítol 1 es caracteritza la uridina com a compost *scavenger* en experiments de cristal·lografia de macromolècules a temperatura ambient. El poder mitigador de la uridina contra el dany per radiació en aquesta tècnica assenyala la potència d'aquest compost en els experiments de dispersió de raigs X a angles baixos publicats per Crosas *et al.* (2017). En el Capítol 2 s'estenen els resultats obtinguts a més nucleòsids i bases nitrogenades en experiments de dispersió de raigs X a angles baixos: 5-metil uridina, citidina, uridina i citosina. Aquests additius, que són els més potents reportats mai en la literatura, permeten mitigar el dany per radiació de manera molt significativa, millorar la qualitat de les dades i la informació continguda en solucions de proteïnes poc concentrades o amb baixos pesos moleculars, fet que estén el rang d'aplicació de la tècnica de SAXS. El Capítol 3 presenta els estudis de dany per radiació fets en cristalls de lisozim crescuts en presència de l'hidrogel peptídic Fmoc-CF, que es mostra com un compost *scavenger* efectiu contra el dany per radiació en experiments de cristal·lografia de proteïnes a temperatura ambient. A més, es proposa un nou mètode d'escalat de dades que permet corregir l'error sistemàtic provocat pel dany per radiació global a temperatura ambient. Per últim, en el Capítol 4, es presenten els resultats obtinguts en irradiar l'enzim Aldosa Reductasa, d'interès biomèdic en diabetis. Aquests resultats, publicats a Castellví *et al.* (2019), permeten aclarir quins són els canvis estructurals de la forma activada de la proteïna respecte de la nativa, i aclareixen perquè molts dels inhibidors farmacològics d'aquest enzim perden potència en tests *in vivo*.

Abstract

The term *radiation damage* in this work is applied to biological macromolecular systems and is defined as the structural and chemical modifications induced by X-rays when interacting with the sample under study.

This PhD Thesis approaches the effects of the radiation damage in biological macromolecules in two very different ways. In one side, several new scavenger compounds have been characterized to mitigate the radiation damage effects in macromolecular crystallography and small-angle x-ray scattering, which in turn may enlarge the scientific cases in which these techniques can be used. In the other side, the effects produced by the radiation damage are used to mimic oxidative stress conditions in protein solutions.

The results obtained in this Thesis are distributed in four chapters. In chapter 1 nucleoside uridine is characterized as a scavenger compound in macromolecular crystallography experiments at room temperature. The scavenging effect of uridine against radiation damage in this technique is in line with the high scavenging power in small angle x-ray experiments reported by Crosas *et al.* (2017). In chapter 2 the results are extended to more nucleosides and nitrogenous bases in small angle x-ray experiments. These additives, 5-methyl uridine, cytidine, uridine and cytosine, have the highest scavenging power ever reported, improve significantly the quality of the data and the meaningful information obtained in SAXS experiments, allow extending the technique to low molecular weight protein and to highly diluted protein solutions. Chapter 3 characterizes and assesses the radiation scavenging properties of composite lysozyme crystals grown in the hydropeptidic Fmoc-CF gel in macromolecular crystallography experiments at room temperature. Moreover, we propose a new method to scale the crystallographic data which corrects the systematic error induced by global radiation damage at room temperature. Finally, chapter 4 studies the effect of irradiation on aldose reductase, an enzyme which has a biomedical interest in diabetes. The study, which is published in Castellví *et al.* (2019), identifies the structural changes of the activated form of the protein with respect to the native form, and clarifies the reason why many drugs targeting the protein had their potency decreased in *in vivo* tests.

Índex

Abreviatures

DR: Dany per Radiació

MX: *Macromolecular Crystallography*

SAXS: *Small Angle X-ray Scattering*

ROS: *Reactive Oxygen Species*

XFEL: *X-ray Free Electron Laser*

ESR: *Electron Spin Resonance*

LET: *Linear Energy Transfer*

XF: *X-ray Footprinting*

SASBDB: *Small Angle Scattering Biological Data Bank*

PDB: *Protein Data Bank*

TCEP: tris(2-carboxyethyl)phosphine

DTT: dithiothreitol

Fmoc: Fluorenylmethyloxicarbonyl

GS: glutahtione

GSH: glutathione reduced

GPx: glutathione peroxidase

GR: glutathione reductase

Introducció

El dany per radiació (DR) és sovint un inconvenient a l'hora de caracteritzar estructuralment sistemes biològics macromoleculars mitjançant tècniques experimentals basades en l'ús de raigs X. Dos casos paradigmàtics són els experiments de cristal·lografia macromolecular (*Macromolecular Crystallography*, MX) i de dispersió de raigs X a angles baixos (*Small Angle X-ray Scattering,* SAXS), en els que la qualitat i la quantitat de les dades obtingudes es veuen clarament limitades pel dany que pateixen les mostres per causa de la irradiació. Aquest fet s'accentua de manera especial quan es treballa amb fonts de llum tan intenses com les que proporcionen els sincrotrons. Pot ser encara més rellevant que la limitació en l'abast de l'experiment, el DR pot donar lloc a conclusions errònies en els models resultants. El control de la dosi incident sobre la mostra és, per tant, sempre recomanables i, molt sovint, necessari. Prova d'això és la gran quantitat de congressos, *workshops* i literatura dedicats específicament als efectes nocius del DR[1–6].

Malgrat els aspectes generalment negatius dels efectes de la radiació, en alguns casos el DR por ajudar a induir algunes reaccions químiques de manera controlada. En particular, es pot aprofitat el fet conegut que la irradiació de solucions aquoses oxigenades amb raig X dona lloc a la generació de les mateixes espècies reactives de l'oxigen (*Reactive Oxygen Species*, ROS) que es troben en ambients cel·lulars sotmesos a estrès oxidatiu. En aquest context, la irradiació de solucions de macromolècules biològiques amb raigs X pot esdevenir per tant un bon banc de proves per a l'estudi de les modificacions induïdes per ROS, sense la necessitat d'afegir cap reactiu químic que pugui emmascarar la correcta interpretació dels resultats.

Així doncs, ja sigui per mitigar els inconvenients del DR en experiments de MX o SAXS, o bé per induir ROS de manera controlada, tenir un ampli coneixement dels efectes del DR és necessari per saber com treballar correctament en ambdues situacions. Per això, la present part introductòria es divideix en tres parts clarament diferenciades, amb la finalitat de contextualitzar tots els resultats que es mostraran en aquesta Tesi.

1. Fonaments del dany per radiació en biomolècules

El terme *dany per radiació* (DR) aplicat a sistemes biològics macromoleculars fa referència a totes les modificacions, tan estructurals com químiques, induïdes pels raigs X en interaccionar amb la mostra experimental.

El DR és, per tant, una conseqüència inherent a l'ús dels raigs X en l'estudi de la matèria que ha de ser tinguda en compte en qualsevol estudi què hi intervingui.

En aquesta primera part introductòria es posaran els fonaments del DR. En primer lloc es revisen de manera general les principals interaccions entre raigs X i matèria (Secció 1.1) i es particularitza pel rang d'energies utilitzat en aquest treball així com també pels principals àtoms constituents dels sistemes biològics (Secció 1.2). Un cop descrites les interaccions es presentaran les diferents maneres de classificar al DR segons si és primari o secundari (Secció 1.3) o bé segons si és directe (Secció 1.4) o indirecte (Secció 1.5). En l'apartat on es descriu el DR indirecte s'aprofundeix en un subapartat extens en la química de la radiació de l'aigua. Aquest subapartat, a banda de ser necessari per a entendre el DR indirecte, és clau per a entendre com i per què la irradiació de solucions aquoses pot esdevenir un bon banc de proves per a l'estudi de proteïnes en presència de ROS, que es tractarà en la tercera part de la introducció.

1.1. Interacció entre raigs X i matèria

La llum interacciona en multitud de maneres amb la matèria, totes elles basades en processos fonamentals que depenen en gran mesura, entre d'altres factors, de la longitud d'ona de la llum que interactua. En el rang de l'espectre d'estudi d'aquest treball, els raigs X, les interaccions amb la matèria es produeixen principalment sobre els electrons dels àtoms que conformen la matèria d'estudi, és a dir, la mostra. Els canals fonamentals d'interacció amb els electrons són: la dispersió Rayleigh, l'efecte fotoelèctric, la dispersió Compton i la creació de parells electró-positró.

Dispersió Rayleigh

En la dispersió Rayleigh, també anomenada dispersió elàstica, un fotó és dispersat per un dels electrons orbitals més externs (Figura 1a). Tant l'energia com el mòdul del moment del fotó es conserven al llarg de tota la interacció. L'efecte de la interacció és un canvi en la direcció del fotó dispersat. La dispersió Rayleigh és la interacció que dóna accés a la informació estructural en les mostres i en la que es basa la pràctica totalitat de les tècniques experimentals en biologia estructural.

Efecte fotoelèctric

En l'efecte fotoelèctric un fotó incident és absorbit per un dels electrons que es troba orbitant al voltant del nucli, de manera més probable en el cas els raigs X, en les capes més internes (capes K o L) (Figura 1b). Com a resultat, l'electró (també anomenat *fotoelectró*) és emès per l'àtom amb una energia cinètica igual a la diferència entre l'energia del fotó incident i la seva energia d'enllaç. Un cop emès el fotoelectró, l'àtom queda en un estat inestable amb la vacant en les capes les capes més internes que ha deixat el fotoelectró. Ràpidament la vacant és reocupada de nou per un electró que ocupa un orbital d'energia més elevada (amb menys energia d'enllaç). En aquest procés de reocupació s'allibera una energia que es canalitza via processos radiatius o bé no radiatius. En el cas dels processos radiatius, la diferència d'energia entre els dos orbitals electrònics és emesa en forma de fotó (*fluorescència de raigs X*) mentre que, per als no radiatius, la diferència d'energia és transferida a un altre electró d'orbital més extern donant lloc a l'emissió d'aquest (*efecte Auger*).

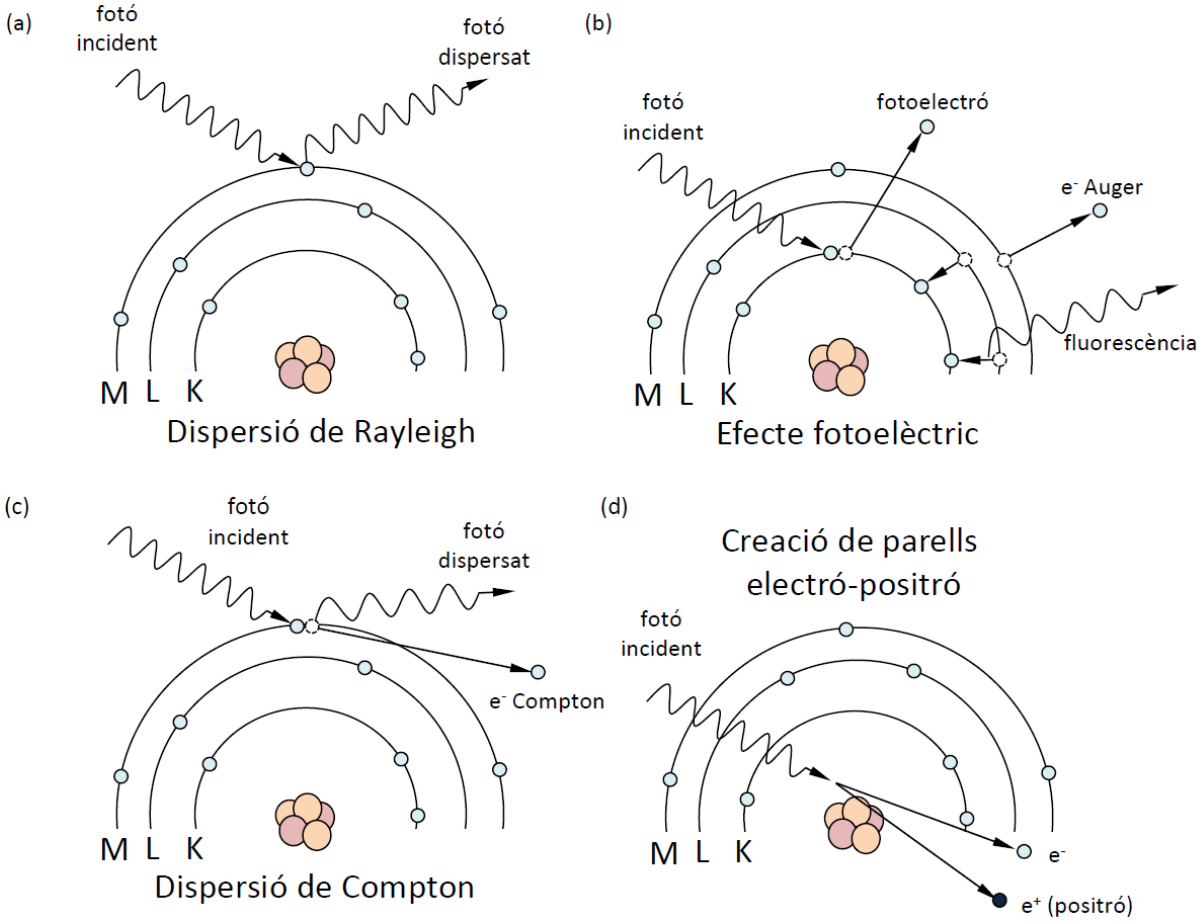

Figura 1 | *Interaccions entre els raigs X i la matèria. Un fotó incideix sobre un electró que orbita al voltant del nucli atòmic donant lloc a quatre possibles interaccions: la dispersió de Rayleigh (a), l'efecte fotoelèctric (b), la dispersió de Compton (c) o la creació de parells electró-positró (d).*

Dispersió Compton

En la dispersió Compton, també anomenada dispersió inelàstica, un fotó interacciona amb un dels electrons de les capes electròniques més externes (Figura 1c). Com a conseqüència d'aquesta interacció el fotó surt dispersat amb una energia menor a la incident i l'electró (electró Compton) és expulsat del seu orbital amb una energia igual a la diferència entre l'energia del fotó incident i l'energia del fotó dispersat. Aquest canal d'interacció llum-matèria és poc utilitzat en tècniques experimentals degut al major nombre de paràmetres que cal determinar.

Creació de parells electró-positró

En el procés de producció d'un parell electró-positró un fotó interacciona amb un nucli atòmic pesat donant lloc a la creació espontània d'un parell electró-positró (Figura 1d). L'energia mínima incident per a que aquesta interacció es pugui donar és dues vegades l'energia en repòs de l'electró (2 × 0.511 MeV). Aquesta energia mínima del foto és molt superior a la que utilitzem típicament ens els experiments de raigs X i, per tant, no intervé en el nostre estudi.

1.2. Interaccions predominants entre fotons incidents amb energies entre 5 i 20 keV i els bioelements

L'energia dels fotons condiciona la interacció entre aquests i la matèria. És per això que, en el context d'aquesta Tesi, només es considerarà la franja de l'espectre electromagnètic compresa entre 5 i 20 keV d'energia (2.4 i 0.58 Å de longitud d'ona, respectivament), rang en el qual es mouen la majoria de línies de llum en instal·lacions de llum de sincrotró destinades a la determinació estructural de macromolècules. En particular, els resultats experimentals obtinguts en aquest treball estaran recollits entre 10 i 13.75 keV (equivalent a 1.24 i 0.902 Å, respectivament).

En comparació amb altres tipus de radiació, els raigs X interaccionen poc amb la matèria. Com a referència, depenent de la mida de la mostra, en un experiment típic de MX en sincrotró només entre un 2 i un 5% del feix incident interacciona amb el cristall[7]. En Física, la probabilitat d'interacció entre un projectil i el seu blanc és directament proporcional al paràmetre *secció eficaç* (σ). Alhora, la secció eficaç d'una interacció depèn de l'energia del projectil i del tipus d'àtom del que estigui format el blanc (Figura 2a). En el cas que ens ocupa, els projectils a considerar són fotons d'energia entre 5 i 20 keV i el blancs són els àtoms que conformen els sistemes biològics macromolecular, és a dir, principalment àtoms de H, C, N, O i S. Aquests bioelements tenen tots ells en comú un pes molecular relativament baix. En la Figura 2b es mostren les seccions eficaces de les interaccions descrites anteriorment en els elements H, C, N, O i S així com també el Fe, un dels àtoms que, malgrat ser menys abundant, és essencial per a la vida. De la Figura 2 se'n pot desprendre que la creació de parells electró-positró no és possible per sota del MeV, que

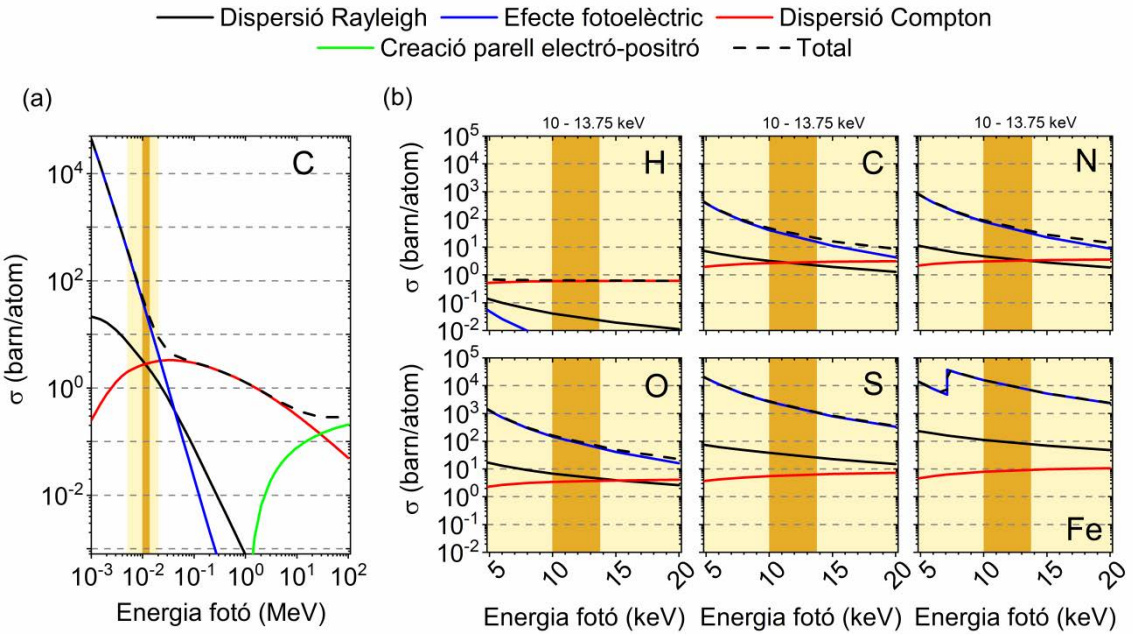

Figura 2 | *Seccions eficaces de les interaccions entre raigs X i la matèria. (a) Seccions eficaces per a l'àtom de carboni en un rang d'energies comprès entre 1 keV i 100 MeV. (b) Seccions eficaces per als àtoms de H, C, N, O, S i Fe en el rang d'energies comprès entre 5 i 20 keV, el rang d'energies típic en experiments de biologia estructural en sincrotrons. El rang d'energies emprat en aquest treball (10 – 13.75 keV) és marcat en taronja. Nota: 1 barn equival a 10^{-24} m. Dades extretes de "XCOM: Photon Cross Sections Database"*[8].

totes les seccions eficaces són directament proporcionals al nombre atòmic i, també, que la interacció predominant en el rang d'energies establert és l'efecte fotoelèctric (amb l'excepció del H). Quantitativament, l'efecte fotoelèctric a 10 keV constitueix entre el 87 i el 98% de les interaccions que es poden donar en àtoms de C, N, O i S (99% en àtoms de Fe).

Un cop emès un fotoelectró, hi ha dos processos competitius de relaxació de l'àtom excitat, l'efecte Auger i la fluorescència, amb probabilitats relatives que depenen de l'element (Figura 3). El procés més probable en àtoms lleugers és l'efecte Auger, mentre que pels àtoms més pesats el canal més provable és la fluorescència. En el nostre cas l'emissió d'electrons Auger en d'àtoms de H, C, N, O i S representa més del

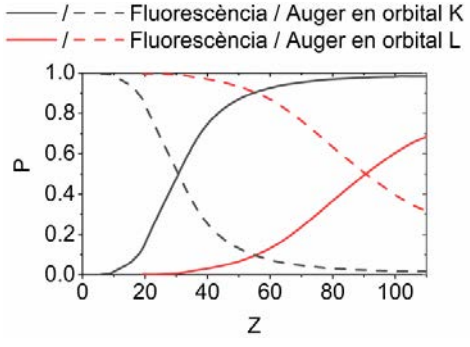

Figura 3 | *Probabilitats d'ocupació d'orbitals buits via fluorescència o via efecte Auger. Probabilitat de fluorescència o de efecte Auger per un fotoelectró emès en l'orbital K o en l'orbital L en funció del nombre atòmic. Les corbes relatives a l'emissió d' un fotoelectró en l'orbital L representa la mitjana dels suborbitals L_1, L_2 i L_3. Les dades han sigut extretes de "X-ray Data Booklet"*[9].

95% dels casos. En canvi, pels àtoms amb nombre atòmic més alt com ara el Fe (Z = 26) o el Au (Z = 79), la fluorescència representa el 30 i el 95% del casos, respectivament.

1.3. El dany per radiació primari i secundari

Les principals interaccions entre raigs X i matèria capaces de ionitzar la matèria i, per tant, modificar-la, són l'efecte fotoelèctric i la dispersió Compton. Les ionitzacions resultants d'ambdues interaccions són doncs els primers esdeveniments que donen lloc al que s'anomena *dany per radiació primari*[10]. La dispersió de Rayleigh, al ser un procés elàstic on l'energia del fotó incident no canvia, no dóna lloc a modificacions en la configuració electrònica de l'àtom i, per tant, no contribueix al DR, si bé pot contribuir al seu anàlisi.

El dany per radiació té continuació més enllà del dany primari causat per l'efecte fotoelèctric i la dispersió Compton. D'una banda tenim encara grans quantitats de fotoelectrons i electrons Auger i, per altra, encara que en menys mesura, tenim també electrons Compton. Tot aquest conjunt d'electrons emesos continuaran produint noves ionitzacions al llarg de les seves trajectòries, donant lloc a una cascada d'esdeveniments ionitzants secundaris (Figura 4). Aquesta cascada de ionitzacions secundàries finalitzarà quan finalment tots els electrons acabin perdent les seves energies.

Anomenem doncs *dany per radiació secundari* al conjunt de totes les modificacions finals en la mostra causades per totes les ionitzacions secundàries al llarg de la irradiació[10].

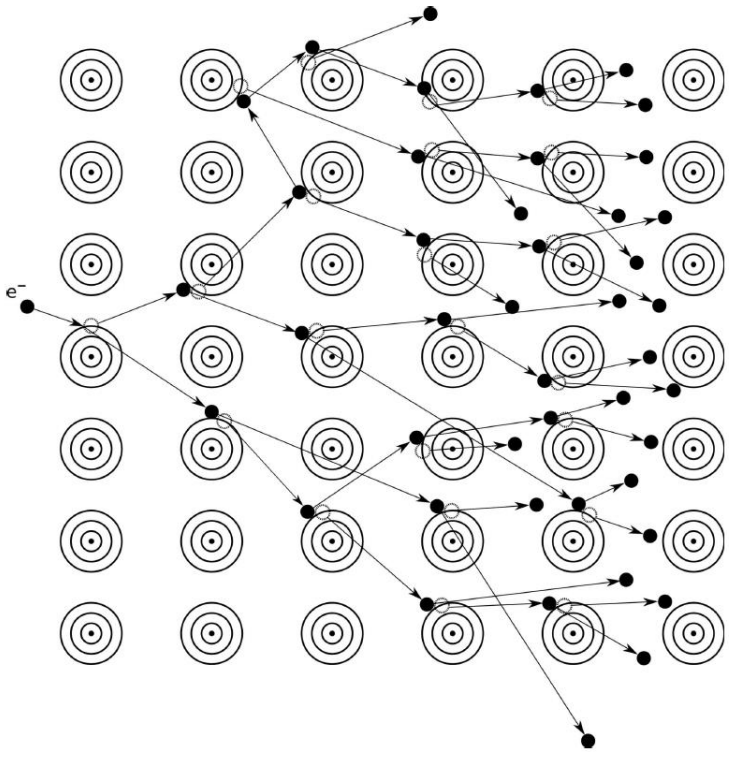

Figura 4 | *Dany per radiació secundari induït per un fotoelectró, un electró Auger o un electró Compton. El resultat d'una ionització primària és una cascada de ionitzacions secundàries. Figura extreta de Nass (2019)*[11].

Fotoelectrons i electrons Auger contribueixen en diferent grau al dany per radiació secundari. Les principals diferències entre ambdós processos rauen principalment en les diferents escales temporals i corresponents energies d'emissió. El temps d'emissió d'un fotoelectró es de l'ordre del attosegon (1 as = 10^{-18} s), mentre que un electró Auger emès per àtoms de C, N, O i S s'emet en 1^{-10} femtosegons (1 fs = 10^{-15} s)[12]. Les energies típiques d'unió dels electrons dels orbitals K varien entre 248 eV per àtoms de C fins a 2.472 keV per als àtoms de S. Així, per a fotons incidents amb energies entre 5 i 20 keV, els fotoelectrons són emesos amb energies molt properes a la del fotó incident. En canvi, les energies típiques en l'emissió d'electrons Auger estan en l'ordre del centenar d'eV, entre 250 eV per àtoms de C i 500 eV per àtoms de O, és a dir, dos ordres de magnitud per sota de les energies dels fotons incidents, donat que aquesta és la diferència d'energia entre orbitals atòmics. Atès que l'energia dels fotoelectrons és molt més elevada que la dels electrons Auger, les característiques dels núvols electrònics generats en les ionitzacions secundàries d'ambdós efectes seran també diferents. Simulacions en cristalls d'urea (CH_4N_2O) infinitament grans mostren precisament aquestes diferències[13]. Els resultats que se'n desprenen de l'estudi són: i) el radi del núvol electrònic generat per un sol fotoelectró de 8 keV és 300 nm, mentre que pel cas d'un sol electró Auger emès per àtom de nitrogen és de 8 nm (Figura 5), ii) després de 20 fs no hi ha més ionitzacions secundàries (d'un total de 390) en la cascada generada pel fotoelectró, mentre que per al cas de l'electró Auger les ionitzacions secundaries finalitzen després de 5 fs (d'un total de 18 ionitzacions)[13].

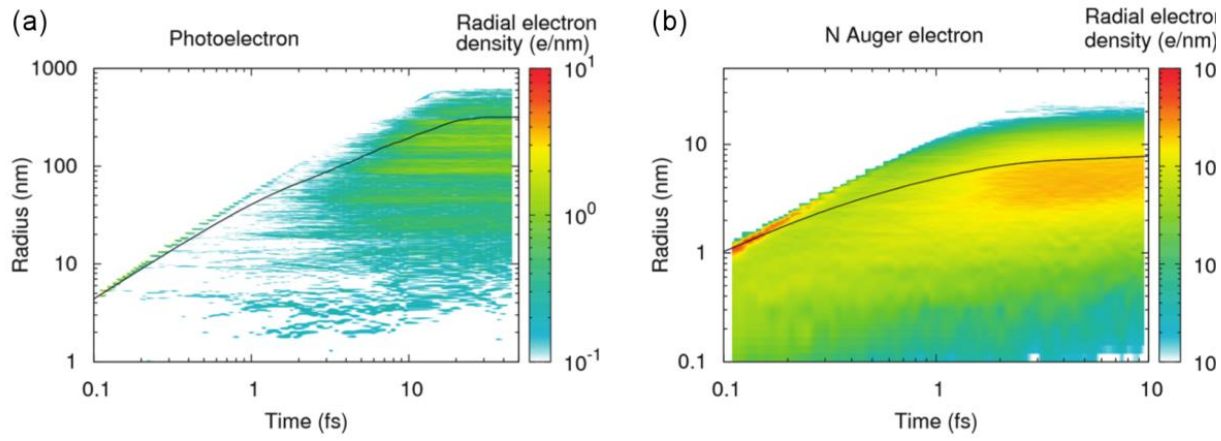

Figura 5 | *Simulacions dels perfils de densitat electrònica radial en funció del temps del núvol d'electrons secundaris en cristalls d'urea infinitament grans. (a) Núvol d'electrons secundaris generat per un fotoelectró de 8 keV d'energia. (b) Núvol d'electrons secundaris generat per un electró Auger emès per un àtom de nitrogen*[13]*. Figura extreta de Caleman et al. (2011)*[13].

Tot i que en molt menor mesura, els electrons Compton també donen lloc a cascades de ionitzacions secundàries. L'abast i les característiques físiques de les cascades Compton també, com en el cas dels fotoelectrons i dels electrons Auger, dependrà de l'energia de l'electró emès. Com a referència, l'energia cinètica d'un electró lliure dispersat per un fotó de 12 keV està compresa dins del rang entre 0 i 0.538 keV. Així doncs, els electrons Compton donaran lloc a cascades de ionitzacions secundàries amb poques de ionitzacions i de més curt abast. Això, juntament amb el fet que l'efecte Compton és minoritari en el rang

d'energies entre 5 i 20 keV, fa que els efectes secundaris d'aquesta interacció siguin negligibles i, per tant, no els tindrem en compte en l'estudi del dany per radiació secundari.

1.3.1. Estratègies per a la mitigació del dany per radiació primari i secundari

L'escala temporal dels processos d'emissió de fotoelectrons i d'electrons Auger fa que tant el dany per radiació primari com el secundari siguin complicats d'evitar. Un dels principals inconvenients és la incapacitat de generar polsos de llum suficientment curs com per que el dany primari i secundari puguin avançar. No obstant, es disposen d'algunes estratègies per a la mitigació del DR, moltes de les quals es basen la reducció del nombre d'ionitzacions secundàries dins de la mostra. Algunes d'aquestes estratègies, fortament dependents de les característiques de la font de raigs X, són:

- l'ús de polsos de raigs X més curts que el temps necessari per a que evolucionin totes les ionitzacions secundàries[14,15]. Aquesta estratègia és utilitzada essencialment en *X-ray Free Electron Lasers* (X-FELS)[14].
- la irradiació de mostres més petites que el recorregut mitjà dels fotoelectrons, de manera que aquests escapin i no es generin cascades d'ionitzacions secundàries dins la mostra[13]. Les línies de llum de sincrotró *microfocus*[16] i els X-FELS[14,15,17] poden dur a terme aquest punt.
- la irradiació de la mostra aplicant la menor dosi absorbida possible (energia absorbida per unitat de massa)[18]. Les fonts de raigs X convencionals i qualsevol línia de llum en sincrotrons poden dur a terme aquesta estratègia.
- la irradiació de la mostra amb feixos de raigs X més petits que el recorregut mitjà dels fotoelectrons, per tal que una fracció significativa dels fotoelectrons induïts provoquin cascades d'ionitzacions secundàries fora de la part il·luminada de la mostra[16,19]. Les línies microfocus són les més adequades per a assolir a aquest punt.

1.4. El dany per radiació directe

Durant la irradiació amb raigs X s'alliberen grans quantitats d'electrons provinents de les ionitzacions generades al llarg de la mostra. D'una banda, aquestes ionitzacions donen lloc a la creació de centres de pèrdua d'electrons (forats) mentre que, per l'altra, alguns dels electrons lliures poden ser capturats per centres de captura d'electrons. Quan aquests centres de captura pertanyen als residus de la proteïna aquests es poden veure radicalitzats en capturar electrons, de manera que el residu acaba essent alterat químicament.

S'anomena doncs *dany per radiació directe* al conjunt de totes les modificacions sorgides com a conseqüència de la creació de centres de pèrdua o de captura electrònica directament en els àtoms de la proteïna.

1.4.1. Modificacions de proteïnes per dany directe

Els centres de pèrdua i de captura d´electrons tant poden estar en la part proteica de la mostra com en la part del solvent. La irradiació del solvent també dona lloc a espècies moleculars i radicals que, indirectament, poden reaccionar amb la part proteica de la mostra (Secció 1.5). Per això, per tal de cancel·lar la contribució indirecta del solvent, la major part dels estudis de dany per radiació directe són duts a terme a temperatures entre 77 i 110K: a aquestes temperatures la difusió de les espècies moleculars generades en el solvent es veu minimitzada, mentre que la difusió dels electrons lliures i dels centres de pèrdua i de captura d'electrons es veu inalterada[20–23]. A continuació es presenten algunes de les modificacions resultants de la generació tan de centre de captura com de pèrdua d'electrons.

L'espècie radical majoritària generada en solucions proteiques per la pèrdua d'electrons és el radical amido, com ho demostren els estudis de ressonància d'espín electrònic (*Electron Spin Resonance*, ESR)[21], seguint la següent cadena de reaccions:

$$(\mathrm{p}) - \mathrm{CHR} - \mathrm{CHNO} - \mathrm{CHR} - (\mathrm{p}) \xrightarrow{-\mathrm{e}^-} (\mathrm{p}) - \mathrm{CHR} - \mathrm{CHN}^{\bullet}\mathrm{O}^{+} - \mathrm{CHR} - (\mathrm{p}) \rightarrow$$
$$\rightarrow (\mathrm{p}) - \mathrm{CHR} - \mathrm{CN}^{\bullet}\mathrm{O} - \mathrm{CHR} - (\mathrm{p}) + \mathrm{H}^{+}$$

essent (p) la resta de la cadena peptídica de la mostra. El radical amido es veu eficientment atrapat a temperatures criogèniques (77K)[21]. Per altra banda, els centres de captura d'electrons $-\mathrm{CHNO}^{\bullet-}-$ no deixen atrapat a l'electró a 77K i aquest és capaç de migrar per la cadena peptídica via efecte túnel fins trobar centres electrofílics[21]. Alguns d'aquestes centres electrofílics poden ser metalls, residus àcids i aromàtics (àcids aspàrtic i glutàmic, tirosines i triptòfans), cisteïnes o ponts disulfur. La captura electrònica per part de cisteïnes i ponts disulfur a 100K dona lloc a desulfuracions i a trencaments dels enllaços S-S[24,25], tal i com ho demostren els experiments de MX, ESR i de Raman sobre cristalls de proteïnes[24–26]. Els mecanismes proposats són els següents:

$$(\mathrm{p}) - \mathrm{CH_2SH} \xrightarrow{+\mathrm{e}^-} (\mathrm{p}) - \mathrm{CH_2^{\bullet}} + \mathrm{SH}^-$$

$$(\mathrm{p}) - \mathrm{CH_2SSCH_2} - (\mathrm{p}) \xrightarrow{+\mathrm{e}^-} (\mathrm{p}) - \mathrm{CH_2SS}^{\bullet-}\mathrm{CH_2} - (\mathrm{p}) \rightarrow (\mathrm{p}) - \mathrm{CH_2S}^- + (\mathrm{p}) - \mathrm{CH_2S}^{\bullet}$$

$$(\mathrm{p}) - \mathrm{CH_2SSCH_2} - (\mathrm{p}) \xrightarrow{+\mathrm{e}^-} (\mathrm{p}) - \mathrm{CH_2SS}^{\bullet-}\mathrm{CH_2} - (\mathrm{p}) \xrightarrow{+\mathrm{H}^+} (\mathrm{p}) - \mathrm{CH_2SH} + (\mathrm{p}) - \mathrm{CH_2S}^{\bullet}$$

La captura d'electrons a 100K també pot donar lloc a que aquests migrin fins a trobar-se amb els grups carbonil de la cadena peptídica. El resultat d'aquesta migració és el trencament de l'enllaç peptídic[27,28]:

$$(\mathrm{p}) - \mathrm{CHR} - \mathrm{CHNO} - \mathrm{CHR} - (\mathrm{p}) \xrightarrow{+\mathrm{e}^-} (\mathrm{p}) - \mathrm{CHR} - \mathrm{C}^{\bullet}\mathrm{HNO}^- - \mathrm{CHR} - (\mathrm{p}) \xrightarrow{+\mathrm{H}^+}$$
$$\xrightarrow{+\mathrm{H}^+} (\mathrm{p}) - \mathrm{CHR} - \mathrm{CH_2NO} + \mathrm{C}^{\bullet}\mathrm{HR} - (\mathrm{p})$$

Pel que fa a la creació de forats, el mecanisme majoritari entre 77 i 100K és la descarboxilació d'aspàrtics i glutàmics (Equació 2) i la creació del radical tirosil (Equació 3) [26,27]:

$$(\mathrm{p}) - \mathrm{CH_2CH_2COO^-} \xrightarrow{-\mathrm{e^-}} (\mathrm{p}) - \mathrm{CH_2C^{\bullet+}H_2COO^-} \rightarrow (\mathrm{p}) - \mathrm{CH_2CH_2^{\bullet}} + \mathrm{CO_2} \qquad \text{(Eq. 2)}$$

$$(\mathrm{p}) - \mathrm{CH_2C_6H_4OH} \xrightarrow{-\mathrm{e^-}} (\mathrm{p}) - \mathrm{CH_2C_6H_4OH^{\bullet+}} \rightarrow (\mathrm{p}) - \mathrm{CH_2C_6H_4O^{\bullet}} + \mathrm{H^+} \qquad \text{(Eq. 3)}$$

1.5. El dany per radiació indirecte

S'anomena *dany per radiació indirecte* al conjunt de totes les modificacions en la part proteica de la mostra resultants de la interacció entre aquesta i les espècies reactives generades en el solvent al llarg de la irradiació. Donat que el component principal constitutiu en les solucions aquoses tampó diluïdes és l'aigua, les espècies reactives generades en la part del solvent esdevindran majoritàriament dels productes de la radiòlisi de l'aigua.

1.5.1. Química de la radiació de l'aigua

A continuació es descriuen els mecanismes de generació de les espècies reactives provinents de la radiòlisi de l'aigua en condicions anaeròbiques i aeròbiques. La descripció es particularitza només per a fotons incidents amb energies entre 5 i 20 keV i té en compte la influència de la font de raigs X en els resultats finals. Cal notar que aquest apartat és una aproximació bàsica als processos que intervenen en la irradiació del solvent d'una solució proteica o del solvent d'un cristall de proteïnes. L'escenari real és un exercici extremadament complex i fora de l'abast d'aquest treball.

Influència en l'energia incident dels fotons

L'exposició d'una mostra experimental dona lloc a l'emissió de grans quantitats de fotoelectrons i d'electrons Compton. Tal i com hem vist en la Secció 1.2, la manera com els fotoelectrons i els electrons Compton dipositen gradualment l'energia al llarg de les seves trajectòries és molt diferent. Una manera de quantificar aquesta diferencia és mitjançant el paràmetre *transferència lineal d'energia* (*Linear Energy Transfer*, LET), definit com la quantitat d'energia mitja per unitat de longitud que un electró diposita en els àtoms que es vagi creuant al llarg de la seva trajectòria. En la Figura 6 es mostren els diferents valors de LET per a electrons incidents amb energies entre 10^1 i 10^6 eV impactant sobre aigua a 25ºC. Segons la figura, a un electró Compton emès per un àtom de carboni amb una energia de 250 eV li correspon un valor de LET al voltant de 30 keV/µm, mentre que a un fotoelectró amb una energia de 10 keV li correspon un valor de 2.3 keV/µm. L'energia dels fotoelectrons es repartirà, per tant, en un radi molt més gran que l'energia provinent dels electrons Compton. Aquest fet, concorda plenament amb les diferències que hi ha entre electrons Compton i fotoelectrons en relació a la quantitat de ionitzacions secundàries i l'abast final d'aquestes (Secció 1.2).

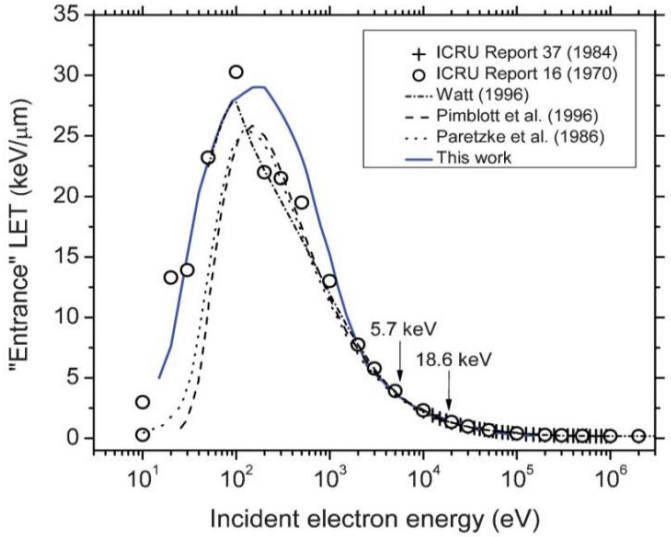

Figura 6 | *Valors de LET per a electrons. Simulació i valors experimentals de la transferència lineal d'energia (LET) per a electrons amb energies entre 10 i 10^6 eV incidents en aigua a 25ºC*[29]. *La línia contínua blava representa els valors de LET simulats per Kohan et al. (2013)*[29]*, la resta representen els valors de LET experimentals en altres treballs. Figura extreta de Kohan et al. (2013)*[29].

El LET de l'electró incident en aigua a 25ºC, a més de ser clau per entendre com es diposita la seva energia al llarg de la seva trajectòria, també afecta severament a l'estequiometria final dels productes radiolítics. Diferents valors de LET donen lloc a diferències en la distribució dels llocs on es perd part de l'energia de l'electró primari: els punts de deposició d'energia estan més ben separats de la trajectòria electrònica principal per a electrons amb valors baixos de LET (Figura 7a i 7c) dins del que s'anomenen *spurs* (en forma esfèrica), pel contrari, els punts de deposició d'energia per a electrons amb valors grans de LET estan més a prop els uns dels altres i donen lloc a un quasi-continu de punts (Figura 7b).

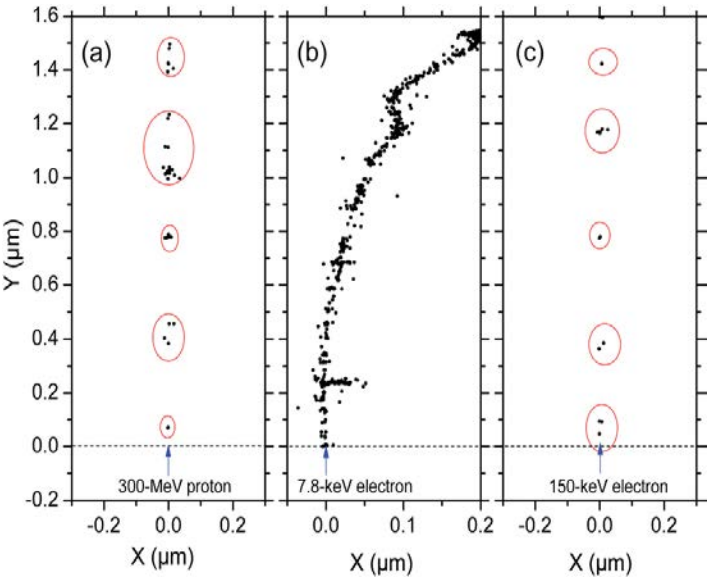

Figura 7 | *Influència en la distribució de les ionitzacions secundàries per partícules amb diferents LETs. Simulacions Monte Carlo de les trajectòries després de 10^{-13} s per un protó de 300 MeV (LET ~ 0.3 keV/ µm) (a), per a un electró de 7.8 keV (LET ~ 5 keV/ µm) (b) i per a un electró de 150 keV (LET~0.3 keV/ µm)*[30]*. Les simulacions són calculades en aigua a 25ºC. Els punts representen els llocs on l'electró primari ha dipositat part de la seva energia al llarg de la seva trajectòria. Els cercles vermells representen els spurs. Figura extreta de Mustaree et al. (2014)*[30].

D'aquesta manera, la concentració final dels productes de la radiòlisi de l'aigua es veu augmentada en el cas d'electrons amb valors de LET superiors a ~ 2.5 keV/µm o, equivalentment, en el cas de fotons incidents amb energies inferiors a ~ 15 keV, aproximadament.

La radiòlisi de l'aigua en condicions anaeròbiques

L'exposició de l'aigua als raigs X en condicions anaeròbiques dona lloc a la radiòlisi de les molècules d'aigua. Els productes radiolítics principals que en resulten són: electrons solvatats (e^-_{aq}), grups hidroxils (OH^-), radicals hidrogen ($H^\bullet$), hidrogen molecular (H_2), radical hidroxil ($^\bullet OH$) i peròxid d'hidrogen (H_2O_2)[29,31]. La següent equació descriu el fenomen:

$$G(-H_2O)H_2O \xrightarrow{X-ray} G(e^-_{aq})e^-_{aq} + G(OH^-)OH^- + G(H^\bullet)H^\bullet + G(H_2)H_2 + G(\,^\bullet OH)\,^\bullet OH + G(H_2O_2)H_2O_2 + \cdots \quad \text{(Eq. 4)}$$

essent G(X) el numero de molècules per cada 100 eV d'energia absorbida per la mostra. La conversió de molècules/100eV a µM/J es pot dur a terme mitjançant el factor de conversió molècules/100eV = 0.104 µM/J. En resum, els productes de l'Equació 4 es van generant al llarg de la trajectòria que segueixen els electrons primaris emesos durant l'exposició de la mostra als raigs X en els transcurs de tres etapes diferents. En la primera etapa, anomenada *etapa física*, l'energia dels fotons incidents és dipositada sobre les molècules d'aigua en ~10^{-16} s, donant lloc a ionitzacions i excitacions. Seguidament, en l'etapa *física-química* (de 10^{-16} fins a 10^{-12} s), les molècules d'aigua excitades o ionitzades relaxen les seves energies mitjançant diferents vies de dissociació. Al final de l'etapa física-química s'obtenen els següents productes: H^+_{aq}, $OH^\bullet$, e^-_{aq}, $H^\bullet$, H_2 i $O^\bullet$. Amb l'aparició d'aquestes espècies radicals comença l'anomenada etapa *química*, on els productes de l'anterior etapa difonen del lloc on han estat originats i comencen a reaccionar amb altres productes en una cascada complexa de reaccions. És en l'etapa química on l'energia dels fotons incidents influeix notablement. Per al cas de fotons amb energies entre 5 i 20 keV l'emissió de fotoelectrons relativament energètics (valors de LET ~ 5 keV/ µm, Figura 6 i Figura 7b) és majoritària i afavoreix la recombinació radical-radical, com per exemple,

$$e^-_{aq} + e^-_{aq} \rightarrow H_2 + 2\,OH^-$$

$$^\bullet OH + \,^\bullet OH \rightarrow H_2O_2$$

$$^\bullet OH + H^\bullet \rightarrow H_2O$$

$$H^\bullet + H^\bullet \rightarrow H_2$$

La recombinació de radicals dona lloc a un increment final en la quantitat de productes radiolítics no radicals. Finalment, l'etapa química es veu acabada en 10^{-6} s, quan tots els productes finals es dispersen apartant-se de la trajectòria de l'electró primari. Després de 1 µs i per a electrons amb una energia de 10 keV, els valors finals de G per a cadascun dels productes radiolítics de l'aigua en condicions anaeròbiques i 25ºC s'estima que és[32]:

$$G(\,^\bullet OH) = 2.1$$

$$G(e_{aq}^-) = 1.8$$

$$G(H^\bullet) = 1.2$$

$$G(H_2) = 1.2$$

$$G(H_2O_2) = 1.1$$

$$G(OH^-) = 0.7$$

Notar que aquests valors són totalment extrapolables per a fotons amb una energia de 10 keV, donat que l'energia dels fotoelectrons emesos, per exemple, en àtoms de carboni, serà de 9.752 keV.

La radiòlisi de l'aigua en condicions aeròbiques

En la majoria dels casos, les solucions en el laboratori estan en equilibri amb l'oxigen molecular present en l'atmosfera (~ 0.3 mM d'O_2). Encara que pugui semblar petita, aquesta presència d'oxigen molecular és suficient com per a que els productes radiolítics finals de l'aigua es puguin veure completament alterats. Més concretament, en la irradiació d'aigua en condicions aeròbiques l'O_2 actua com un compost que elimina els radicals (compost *scavenger*, veure Secció 2.2, 2.3 i 3.2.1) e_{aq}^- i $H^\bullet$ de manera que, en menys d'1 μs, aquestes dues espècies s'eliminen completament donant lloc a dues noves formes radicals, el radical hidroperoxil ($HO_2^\bullet$) i el radical superòxid ($O_2^{\bullet-}$):

$$e_{aq}^- + O_2 \rightarrow O_2^{\bullet-}$$

$$H^\bullet + O_2 \rightarrow HO_2^\bullet$$

Les quantitats finals d'ambdues espècies, en ser l'una la forma protonada de l'alta, venen determinades per l'acidesa del medi, segons la reacció:

$$O_2^{\bullet-} + H^+ \leftrightarrow HO_2^\bullet \ (pK_a = 4.9)$$

En base a aquestes reaccions, després d'1 μs, la quantitat de productes radiolítics finals de l'aigua en condicions aeròbiques i a 25ºC s'estima que són, per a electrons incidents amb 10 keV d'energia, les següents[33]:

$$G(H_{aq}^+) = 2.3$$

$$G(O_2^{\bullet-}) = 1.6$$

$$G(^\bullet OH) = 1.4$$

$$G(HO_2^\bullet) = 0.9$$

$$G(H_2O_2) = 0.8$$

$$G(OH^-) = 0.6$$

$$G(O_2) = 0.2$$

Influència de la taxa de dosi absorbida

La quantitat final de productes radiolítics de l'aigua es veu influenciada també tant pel tipus de font ionitzant considerada[29] com pel flux incident d'aquesta[34]. A mesura que augmenta el flux de fotons incidents sobre la mostra, els camins dels electrons emesos per les ionitzacions resultants comencen a solapar-se els uns amb els altres i es facilita la recombinació d'espècies radicals. Aquest efecte pot ser rellevant en un feix de llum tan brillant com el que proporciona un sincrotró i, per tant, cal revisar-ne la influència.

Els efectes de la llum de sincrotró s'han estudiat prenent com a referència l'anomenada solució dosimètrica de Fricke amb fotons incidents de 20 keV[34]. La solució de Fricke es composa de 0.4 M H_2SO_4, 6 mM $FeH_8N_2O_8S_2$ i 1 mM KCl, en condicions aeròbiques, i s'ha fet servir durant molts anys com a mesura indirecta de la dosi absorbida experimental en una mostra[35]. Els productes radiolítics finals de la solució dosimètrica de Fricke estan ben establerts i donen lloc a:

$$G(Fe^{3+}) \quad = 3G(e_{aq}^-) + 3G(H^\bullet) + G(\ ^\bullet OH) + \ 2G(H_2O_2)$$

Els resultats de la irradiació de la solució de Fricke amb llum de sincrotró de 20 keV en funció de diferents taxes de dosi absorbida condueixen a variacions en la quantitat final de Fe^{3+}. Concretament, a mesura que la taxa de dosi absorbida incrementa, la quantitat final de Fe^{3+} decau linealment amb un pendent de -0.37 ± 0.09 (nmol/J)/(Gy/s) [34].

Influència d'additius scavenger en la mostra experimental

En alguns casos, és interessant aïllar algunes de les espècies reactives generades en la radiòlisi de l'aigua. Per tal d'assolir aquest propòsit una opció usada correntment és fer ús d'additius *scavenger* per tal de decidir quines espècies reactives eliminar i quines afavorir.

L'òxid de nitrogen (N_2O) i el format de sodi (HCOONa) són dos dels *scavengers* més comuns a l'hora d'adoptar aquesta estratègia. Les solucions aquoses saturades amb N_2O donen lloc a l'eliminació de e_{aq}^- i afavoreixen la creació del radical $OH^\bullet$ via[36]:

$$e_{aq}^- + N_2O + H^+ \rightarrow N_2 + OH^\bullet$$

En canvi, la presència de HCOONa en solucions aquoses aeròbiques contribueix a l'eliminació de e_{aq}^-, $H^\bullet$ i $OH^\bullet$ i, alhora, afavoreix la creació de $O_2^{\bullet-}$:

$$e_{aq}^- + O_2 \rightarrow O_2^{\bullet-}$$

$$H^{\bullet} + HCOO^{-} \rightarrow H_2 + CO_2^{\bullet -}$$

$$OH^{\bullet} + HCOO^{-} \rightarrow H_2O + CO_2^{\bullet -}$$

$$CO_2^{\bullet -} + O_2 \rightarrow O_2^{\bullet -} + CO_2$$

El camp dels additius *scavengers* és molt ampli i les alternatives a seguir són molt diverses. Per exemple, sovint es fa ús de petites quantitats d'alcohol, de metanol o d'hidroquinones, entre d'altres, com a scavengers de $^{\bullet}OH$[37]. El nitrat de sodi ($NaNO_3$) i altres compostos amb àtoms de sofre (1,4-Dithiothreitol, cisteïnes, tiourea...) són sovint emprats també com a additius scavenger de e_{aq}^{-}[20,38]. Una completa revisió dels mecanismes d'eliminació de radicals (mecanismes *scavengers*) per a una gran llibreria d'additius químics es pot trobar en l'extens treball de Buxton *et al.* (1988)[31].

1.5.2. Modificacions en proteïnes per dany indirecte

Tal i com s'ha parlat anteriorment, l'exposició de la part del solvent d'un sistema biològic macromolecular dona lloc a la generació d'espècies molt reactives, principalment provinents de la radiòlisi de l'aigua. Aquestes espècies proveeixen al sistema biològic macromolecular en qüestió un ambient oxidant ric en espècies reactives de l'oxigen ($OH^{\bullet}$, $O_2^{\bullet -}/HO_2^{\bullet}$ i H_2O_2) i també en espècies reductores com el $H^{\bullet}$ i el e_{aq}^{-}.

L'estudi de les modificacions en solucions proteiques fent ús del dany per radiació indirecte és un camp àmpliament explorat[39–42]. La detecció d'aquestes modificacions majoritàriament es duu a terme mitjançant tècniques d'espectroscòpia de masses[39–42], tot i que, encara que menys mesura, en algunes ocasions també s'han pogut observar amb MX[43]. La quantitat de possibles modificacions i mecanismes del DR indirecte és molt extensa i, per tant, la completa descripció de totes elles s'escapa de l'abast d'aquesta tesi. No obstant, en base a la similitud amb alguns dels experiments que s'han realitzat al llarg d'aquesta tesi, a continuació es mostraran algunes de les principals modificacions que s'indueixen de manera rutinària en els experiments de X-ray footprinting (XF) (duts a terme en sincrotrons) pel que fa al radical $OH^{\bullet}$.

Les modificacions induïdes pel radical $OH^{\bullet}$ en solucions proteiques en condicions aeròbiques a temperatura ambient són la base dels experiments de XF en sincrotrons[39,42,44]. La tècnica de XF s'aprofita de la gran quantitat de radicals $OH^{\bullet}$ induïts per la radiació per a fer ús d'elles com a sondes per a reaccionar amb aquells aminoàcids accessibles al solvent i, posteriorment, marcar-los amb O_2. Un cop els aminoàcids han sigut marcats per l'O_2, aquests poden ser detectats fàcilment per espectrometria de masses i, per tant, es pot obtenir finalment un mapa complert de l'accessibilitat al solvent de la proteïna. Hi ha dos mecanismes de modificació de la cadena lateral via interacció amb $OH^{\bullet}$ i posterior marcatge amb O_2 . El primer mecanisme és l'eliminació d'un hidrogen en algun dels àtoms de carboni de la cadena lateral. El segon és l'atac nucleofílic directament en àtoms de sofre o dobles enllaços conjugats. L'eliminació

d'àtoms d'hidrogen es produeix principalment en la majoria de cadenes laterals alifàtiques i prolines, mentre que l'atac nucleofílic apareix principalment en cisteïnes, metionines, aminoàcids aromàtics i histidines (Figura 8). Després de la radicalització de les cadenes laterals per l'atac de $OH^{\bullet}$, en ambdós casos, els residus sofreixen l'eliminació dels grups hidroperoxils en presència de O_2 donant lloc a un adducte final de massa estable.

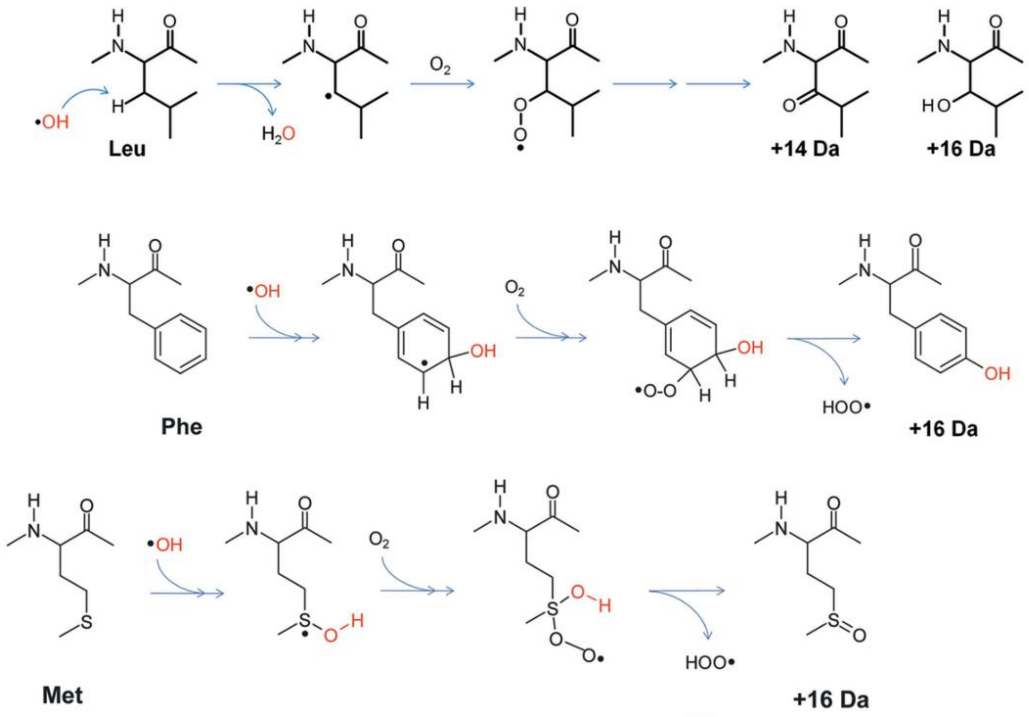

Figura 8 | *Mecanismes per a la modificació de cadenes laterals per $OH^{\bullet}$. Primera fila: les cadenes laterals d'hidrocarburs es veuen modificades principalment per l'eliminació d'un dels àtom d'hidrogen via interacció amb $OH^{\bullet}$. El resultat dona lloc a un radical centrat en un dels àtoms de carboni que, després, acabarà reaccionant amb O_2 i generant productes estables amb un increment de pes molecular de +14 o de +16 Da. Segona i tercera fila: els aminoàcids aromàtics o que contenen àtoms de sofre es veuen directament hidroxilats pel radical $OH^{\bullet}$ i, seguidament, reaccionen amb O_2 per a donar lloc a productes estables de pes molecular +16 Da*[42]. *Figura extreta de Gupta et al. (2016)*[42].

En aquest apartat només s'han descrit les principals modificacions induïdes pel radical $OH^{\bullet}$, l'espècie molecular més reactiva de totes les que apareixen en la radiòlisi de l'aigua (veure Secció 3.2.2). La descripció complerta de les modificacions causades per altres espècies escapa de l'abast d'aquest treball. Es remet al lector a la bibliografia per a conèixer altres reaccions donades per altres espècies, com ara el $O_2^{\bullet-}$ el H_2O_2 i el $H^{\bullet}$ [41,45,46].

2. El dany per radiació en experiments de biologia estructural en sincrotrons

El DR en sistemes biològics és un fenòmen estudiant àmpliament en el camp de la radiobiologia, des de fa moltes dècades[47]. Els efectes nocius de la radiació sobre organismes vius comporten conseqüències a diferents escales, que van des dels efectes sobre les persones o els animals[48] a efectes més fonamentals a nivell molecular[49]. Una de les maneres de comprovar a nivell molecular quins són aquests efectes és mitjançant l'ús de tècniques de biologia estructural, com ara MX i SAXS.

A continuació es presenten les conseqüències del DR que poden ser observades en experiments de MX i SAXS, així com també algunes de les estratègies per a evirtar-les (Secció 2.1). En particular, es farà èmfasi en l'ús de compostos *scavenger* com a estratègia per a reduir el DR en ambdues tècniques estructurals (Secció 2.2 i 2.3).

2.1. Empremtes i mitigació del dany per radiació en MX i SAXS

Les dues tècniques més emprades per a determinar l'estructura tridimensional de macromolècules amb llum de sincrotró són la cristal·lografia de macromolècules (MX) i la dispersió a baixos angles (SAXS). Una diferència fonamental entre aquestes dues tècniques és la forma en què la macromolècula es prepara per ser estudiada: mentre en MX la mostra és un cristall de macromolècules, en SAXS la mostra és en solució. Una descripció més detallada d'ambdues tècniques es pot trobar en Wlodawer *et al.* (2013)[50] i en Skou *et al.* (2014)[51]. La diferent preparació de la mostra, en solució i en cristall, implica una gran diferència en la concentració de la macromolècula. Aquest fet és molt rellevant en la influència del DR en els experiments de SAXS i MX. Concretament, les mostres més diluïdes, les solucions proteiques, contenen molt més solvent que les formes cristal·lines i, per tant, són les que pateixen més els efectes del DR[49,52,53].

A continuació es fa un repàs de les principals empremtes que DR deixa en els experiments de SAXS i MX, així com també de les estratègies més usuals per a la mitigació dels seus efectes.

Experiments de SAXS

Donat que els experiments de SAXS proporcionen informació estructural a baixa resolució les empremtes del DR queden reduïdes només a que es puguin observar a escala global. Les principals conseqüències del DR són l'agregació (Figura 9a), el desplegament i la fragmentació de la proteïna[52,54,55]. Aquests efectes, en ser tots ells globals i no específics per residus de la proteïna, es poden veure més fàcilment en la regió dels angles més baixos dins dels perfils de dispersió (Figura 9b). L'avaluació dels efectes globals es realitza mitjançant mètriques, és a dir, estimadors que avaluen amb un sol valor els

efectes del DR. Les mètriques més adequades i emprades en la literatura existent en SAXS són el radi de gir (R_g), la intensitat en l'angle zero ($I(0)$), el volum de Porod[55] (V_P) i la comparació estadística entre perfils de dispersió[55,56].

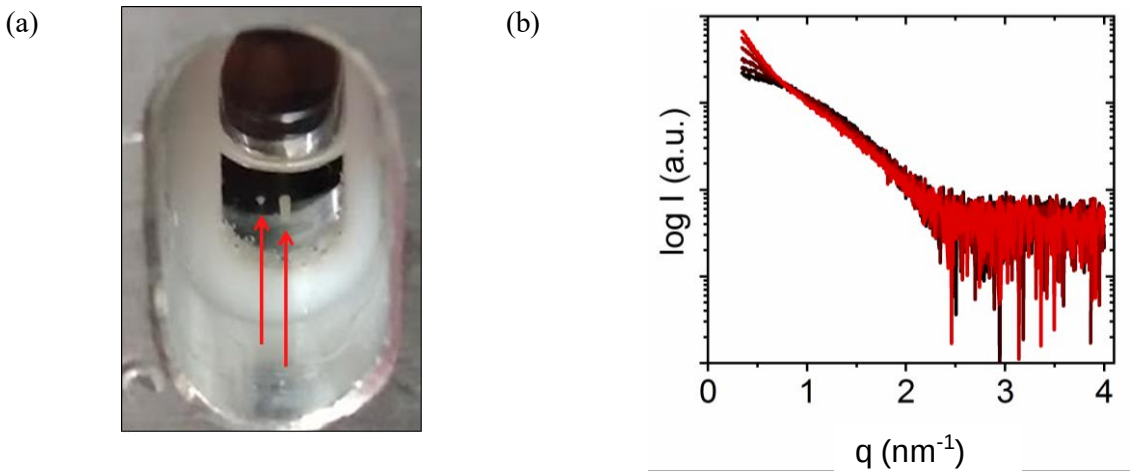

Figura 9 | *Exemple de l'efecte d'agregació provocat pel DR en SAXS. (a) La irradiació d'una solució de lisozim ha donat lloc a l'agregació de la proteïna. Les fletxes vermelles assenyalen la trajectòria del feix de raigs X i alhora també la part agregada de la mostra. Figura obtinguda en un experiment de dut a terme a la línia de llum NCD-SWEET al sincrotró ALBA. (b) Els efectes globals del DR en mesures de SAXS es veuen principalment a la regió d'angles baixos ($q = 4\pi\ sin\theta/\lambda$) dins dels perfils de dispersió. Els perfils de dispersió estan dibuixats de menys a més dosi absorbida (de negre a vermell, respectivament) per la mostra.*

Fins i tot tenint en compte que els efectes del DR observats en SAXS són només una part dels processos que intervenen en la irradiació de solucions de proteïnes, el DR en SAXS és molt acusat respecte d'altres tècniques bio-estructurals. Per l'alt contingut de solvent de la mostra, s'espera que el principal agent del DR en SAXS sigui el dany indirecte, molt per davant del directe.

Algunes de les estratègies per a la mitigació del DR en SAXS són l'atenuació o desfocalització del feix de raigs X, l'escurçament del temps d'exposició en la mostra o la circulació de la mostra durant el temps d'irradiació[57]. La finalitat d'aquestes estratègies és la reducció de la dosi absorbida a la mostra i, per tant, són en detriment a poder recollir dades amb una bona relació senyal-soroll en el detector. És en relació a aquest punt que l'ús d'additius *scavenger* contra el DR indirecte, que no requereix la modificació de les condicions d'irradiació, és extremadament útil en els experiments de SAXS. Prova d'això és que l'addició d'*scavengers* en les mostres per experiments de SAXS és una de les estratègies de mitigació del DR més àmpliament utilitzada per la comunitat d'usuaris d'aquesta tècnica (Secció 2.2). Per últim, tot i que encara està lluny de ser implementada de manera rutinària, la irradiació de solucions vitrificades de macromolècules a temperatures criogèniques (crio-SAXS) també s'ha mostrat com una tècnica efectiva contra el DR[58].

Experiments de MX

En el cas dels experiments de MX, en ser una tècnica bio-estructural d'alta resolució, podem classificar les conseqüències del DR en dos tipus: i) el DR global, que afecta a tota o gran part de la proteïna i/o cristall i ii) el DR específic, és a dir, sobre residus determinats. Les empremtes que deixa el DR global donen lloc a una pèrdua en les intensitats experimentals resultants de la dispersió de Rayleigh (en particular en zones corresponents a l'alta resolució)(Figura 10), a una expansió de la cel·la unitat, a l'increment dels valors estadístics relatius a les diferències entre les intensitats de les reflexions al llarg de la irradiació (R_{meas} i $CC_{1/2}$), al decaïment del paràmetre senyal-soroll, a l'increment dels desplaçaments atòmics (B-factors) i a l'increment de la moisaïcitat del cristall[10,59,60]. Altres conseqüències globals al llarg de la irradiació també es poden veure directament en la morfologia del cristall, com ara canvis en la coloració o, fins i tot, fractures i forats.

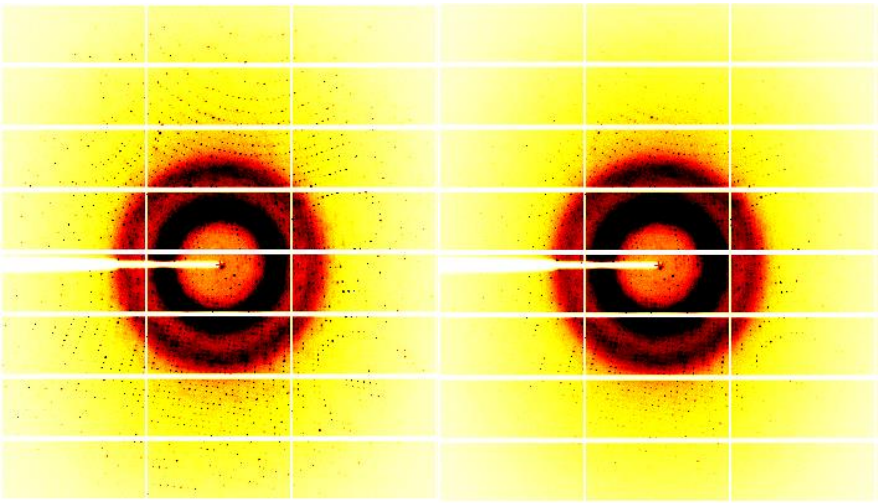

Figura 10 | *El DR global en experiments de MX dona lloc a la pèrdua de les intensitats experimentals resultants de la dispersió de Rayleigh. Esquerra: patró de difracció d'un cristall d'AKR1B1 amb 0.03 MGy de dosi absorbida a 0.92 Å de resolució (R_{meas} = 0.352 en el rang de resolucions entre 0.94 i 0.92 Å). Dreta: patró de difracció del mateix cristall d'AKR1B1 amb 3.45 MGy de dosi absorbida a 1.12 Å de resolució (R_{meas} = 0.335 en el rang de resolucions entre 1.19 i 1.17 Å). Ambdós patrons de difracció estan col·lectats en la mateixa orientació.*

El DR global en MX és significativament més acusat a temperatura ambient que a temperatures criogèniques: les dosis crítiques a 100K són fins a 100 vegades més elevades que les corresponents a temperatura ambient[61,62]. La dosi crítica es defineix com la dosi del conjunt de dades experimentals en què la intensitat total dels pics de difracció baixa al 50% respecte del primer conjunt de dades. L'augment enorme de la dosi crítica a 100K respecte a temperatura ambient pot indicar que el DR global a 100K és un efecte directe, mentre que a temperatura ambient és una barreja entre directe i indirecte. A banda dels possibles efectes directes i indirectes, s'ha vist també que la creació de gasos dins dels cristalls generats llarg de la irradiació també pot contribuir al DR global, especialment a temperatura ambient (Figura 11)[59].

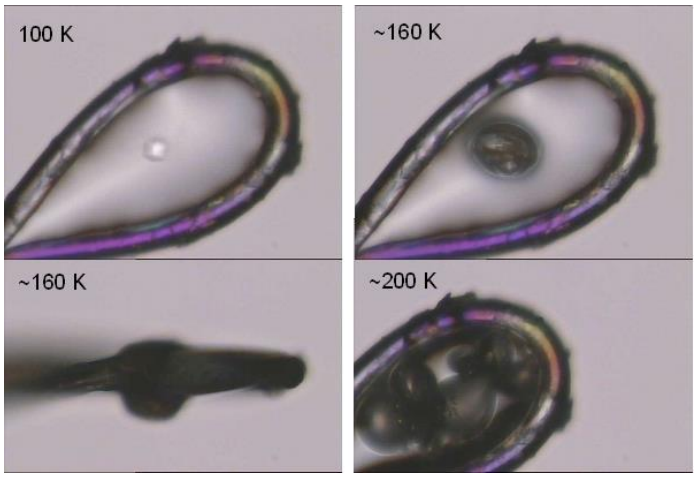

Figura 11 | *L'exposició d'un cristall de proteïnes als raigs X dona lloc a la creació de gasos dins d'ell. Exposició d'un micro-cristall d'insulina al feix de llum de sincrotró. Figura superior de la primera columna: el cristall ha sigut pescat amb l'ajut d'un llaç de niló d'una solució que conté etilenglicol i està alineat amb el feix de llum de sincrotró (abans de l'exposició) a 100K. Altres figues: després d'haver exposat el cristall a la llum de sincrotró, la temperatura del cristall s'ha incrementat (de 100 a 200K) i han començat a aparèixer bombolles de gas en el lloc de l'exposició als raigs X*[59]*. Figura extreta de Meents et al. (2010)*[59]*.*

El dany per radiació específic a 100 K molt sovint apareix de manera molt establerta en el temps: primer, els centres metàl·lics es veuen reduïts, després els ponts disulfur s'elonguen i s'acaben trencant, seguidament les cisteïnes perden els seus àtoms de sofre, els aspàrtics i glutàmics es descarboxilen, els enllaços carboni-sofre de les metionines es trenquen i les tirosines perden els seus grups hidroxils (Figura 12a i 12b). A banda dels efectes específics en aminoàcids, les molècules de solvent també es veuen afectades fàcilment pel DR i induir moviments en l'estructura (Figura 12c).

El DR indirecte és difícil de veure en MX. De la mateixa manera que es generen les modificacions en els experiments de XF, tot i que probablement en menys mesura, caldria esperar que les espècies reactives generades en la radiòlisi del solvent induïssin oxidacions en la part exposada de l'estructura. Sorprenentment però, la major part dels estudis de DR en MX no descriuen aquestes oxidacions en les seves estructures. Fins on arriba el meu coneixement, l'únic treball on es veuen oxidacions induïdes pel DR és en la irradiació d'un cristall del fotosistema II (PSII) a 100 K[43]. El que diferència aquest treball dels altres és principalment la manera de processar les dades: les densitats electròniques s'han ressaltat mitjançant la normalització dels factors d'estructura experimentals i el posterior refinat en base als procediments de Sayre[43]. Aquesta manera de generar els mapes de densitats electròniques és molt diferent de la resta dels treballs de DR en MX, que fa ús generalment, dels típics mapes $2F_{obs} - F_C$ i $2F_{obs} - F_C$ (F_{obs} i F_C representen els factors d'estructura observats experimentalment i calculats, respectivament).

Existeix un ampli ventall d'estratègies per a la mitigació del DR en MX. D'entre totes elles, les més conegudes són: l'atenuació o desfocalització del feix de raigs X[61], l'escurçament del temps d'exposició, la irradiació de més d'un cristall[18] (e.g. *serial crystallography*[63]), la irradiació de diferents parts d'un mateix cristall (e.g., col·lecció de dades de manera helicoïdal[64]), l'ús de línies de llum micro-focus[16] i la irradiació

a temperatures criogèniques[65]. La col·lecció de dades a 100K s'ha convertit en l'estratègia més popular contra el DR en MX, donat que permet incrementar la dosi crítica fins a 100 vegades respecte a la col·lecció a temperatura ambient. No obstant, malgrat l'intensiu ús de les tècniques criogèniques per a la mitigació del DR, els experiments de MX a temperatura ambient guanyen cada dia més interès per tal de veure possibles moviments dins de l'estructura cristal·logràfica.

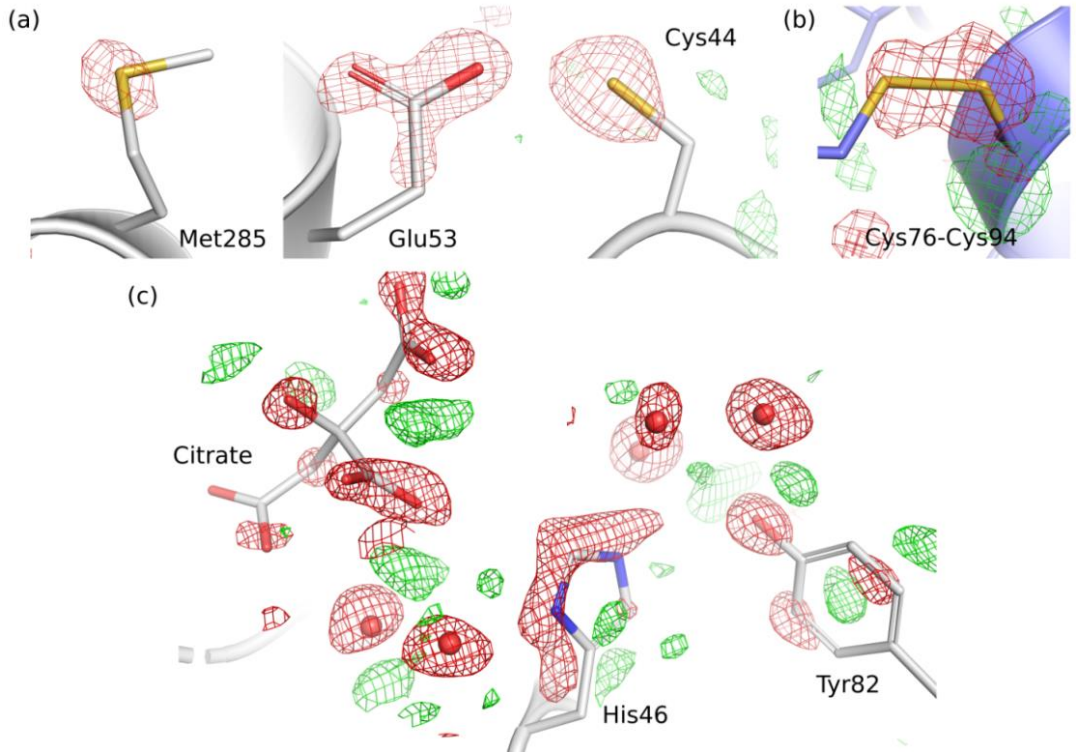

Figura 12 | *El DR específic a 100 K en MX. Mapes de diferències de Fourier (σ = +4 en verd i σ = -4 en vermell) per a la visualització del DR específic. (a) Trencament d'un enllaç de carboni-sofre en una metionina, la descarboxilació d'un glutàmic i la dessulfuració d'una cisteïna en un cristall d'AKR1B1 a 3.45 MGy de dosi absorbida. (b) Trencament d'un pont disulfur en un cristall de lisozim a 5.5 MGy de dosi absorbida. (c) El DR específic sobre una molècula de citratat i sobre molècules d'aigua indueix moviments en una tirosina i en una histidina dins d'un cristall d'AKR1B1 a 3.45 MGy de dosi absorbida.*

2.2. L'ús de scavengers en experiments de SAXS

L'ús de compostos *scavenger* en experiments de SAXS està molt establert en la seva comunitat d'usuaris. Una possible explicació d'aquest fet és el gran poder que tenen aquests compostos alhora de mitigar el DR indirecte: la dosi tolerada, en alguns casos, pot arribar a veure's incrementada fins a 5 cops. El 61.3% de les dades experimentals dipositades en el Small Angle Scattering of Biological Data Bank (SASBDB) descriu l'ús de compostos *scavengers* en els seus experiments (Figura 13a). Concretament, entre les entrades on es descriu l'ús de compostos *scavenger*, el 45.8% d'aquestes fan servir dithiothreitol (DTT), el 44.5% glicerol, el 8.5% tris(2-carboxyethyl)phosphine (TCEP) i el 1.1% sucrosa en els seus

experiments (Figura 13b). L'ús d'àcid ascòrbic, un conegut additiu *scavenger* per SAXS, no es troba descrit en cap de les entrades de la base de dades. Cal notar que, de totes les entrades dipositades en el SASBDB, el 98.8% s'han dut a terme amb raigs X (provinents d'un sincrotró o bé d'un laboratori de raigs X). Considerant només les entrades obtingudes en sincrotrons, l'ús de compostos *scavenger* és independent tant del tipus de macromolècula considerada així com del seu pes molecular (Figura 13c). Per tant, es pot afirmar que l'ús de compostos *scavenger* és tingut en compte per la comunitats d'usuaris de SAXS en sincrotrons.

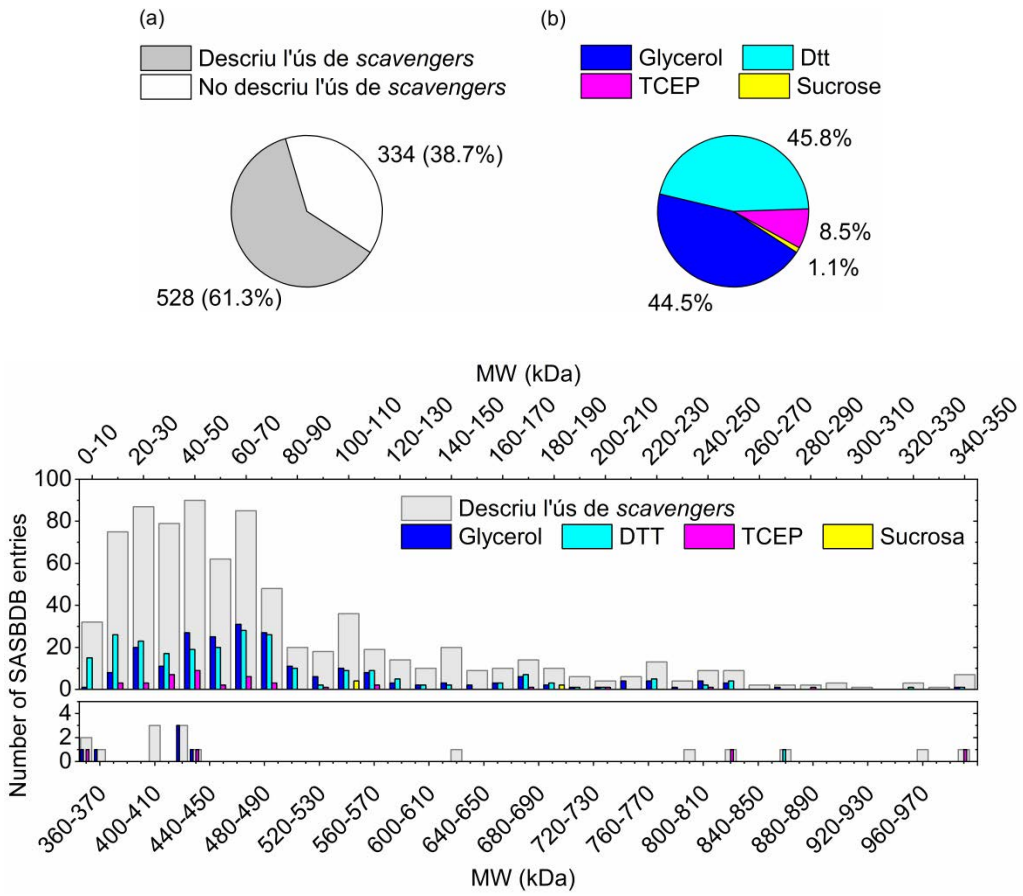

Figura 13 | *Els compostos scavenger s'utilitzen àmpliament per la comunitat d'usuaris de SAXS. (a) Quantitat d'entrades en el SASBDB en les que es descriu (en gris) o no es descriu (en blanc) l'ús de compostos scavenger en les mostres. (b) Dins del grup d'entrades del SASBDB que descriuen l'ús de scavengers: percentatge d'entrades que descriuen l'ús de glicerol (en blau fort), de dithiothreitol (DTT, en blau fluix), de Tris(2-carboxyethyl)phosphine (TCEP, en magenta) i de sucrosa (en groc).(c) Distribució del nombre d'entrades en el SASBDB que no descriu cap scavenger (en gris), que descriu l'ús de glicerol (en blau fort), de DTT (en blau fluix), de TCEP (en magenta) i de sucrosa (en groc), en funció del pes molecular de macromolècula considerada. Les dades han sigut obtingudes a partir d'un datamining fet en Python el dia 17/09/2018. Figura pendent de ser publicada.*

Una avantatge de considerar l'ús de scavengers en SAXS és, a banda de l'efectivitat contra el DR, la facilitat per a ser afegits en solucions macromoleculars. Ara bé, el fet de treballar amb additius contra el DR pot donar lloc a inconvenients inesperats si no es coneixen abans amb antelació. Per exemple, tan el DTT com el TCEP són agents reductors molt potents que cal evitar en el cas de que la mostra contingui ponts disulfur, l'àcid ascòrbic pot donar lloc a alterar el pH de les solucions i el glicerol i la sucrosa poden afectar les interaccions intermoleculars molt fàcilment. A banda d'aquestes consideracions químiques, també hi han altres efectes de caire més tècnic que cal tenir en compte com ara el fet de que més del 3% de glicerol pot donar lloc a superar la màxima pressió tolerada en algunes columnes de FPLC o bé que el contrast entre la part del solvent i la part proteica es pot veure afectada[54,66].

2.3. L'ús de scavengers en experiments de MX

L'ús de compostos *scavenger* per a la mitigació del DR en experiments de MX no és molt extens, donat que sovint comporta més desavantatges que avantatges. Els possibles motius són els següents: i) una gran fracció de la radiació incident és absorbida directament pels àtoms de la proteïna i ii) la relació entre molècules *scavenger* i molècules de proteïna és molt baixa com per a poder proporcionar suficient protecció contra el DR indirecte[38,67].

Hi ha molts pocs exemples de la utilització de compostos *scavengers* per a MX en la literatura. A temperatura ambient, l'ús de 0.5 M de 1,4-benzoquinona i de 0.5 M d'àcid ascòrbic és demostrat per Barker *et al.* (2009) ser efectiu contra el DR global, permetent prolongar la dosi crítica del cristall fins a un factor 9 i 2, respectivament[68]. Pel que fa a la irradiació a 100 K, l'ús de 0.5 M de nitrat de sodi és descrit per De la Mora *et al.* (2011) ser efectiu a nivell global i específic, donant lloc a factors de protecció de 2 i de 5 en la dosi crítica i en els nivells de protecció en ponts disulfur, respectivament[20]. Addicionalment, els estudis de Kmetko *et al.* (2011) contribueixen a donar llum sobre què succeeix amb el nitrat de sodi a més baixes concentracions[38]. Concretament, Kmetko *et al.* conclouen que l'ús de 100 mM de nitrat de sodi no protegeix a 100 K a nivell global però sí ho fa específicament, en canvi, a temperatura ambient hi ha protecció tan a nivell global com a nivell específic[38]. El treball de Kmetko *et al.* és alhora molt il·lustratiu en quan a mostrar com de complicat és trobar un bon *scavenger* per MX: només 1 d'un total de 19 potencials compostos *scavenger* va ser capaç de mostrar protecció contra el DR[38]. També, en la mateixa línia, en el treball de Allan *et al.* (2013) es pot trobar un ampli recull de tots els intents (exitosos i frustrats) que s'han descrit en MX en l'ús de *scavengers*[67]. Aquest darrer treball, també es pot comprovar la gran variabilitat que hi ha en els resultats experimentals[67].

3. L'estrès oxidatiu

L'oxigen molecular, O_2 , present en un 21% en l'atmosfera terrestre, participa en multitud de mecanismes clau per a la vida. El cas més rellevant és la respiració cel·lular. En organismes aerobis l'oxigen és l'últim acceptor dels electrons en la cadena respiratòria, resultant en la formació final de molècules d'aigua:

$$O_2 + 4H^+ + 4e^- \rightarrow 2H_2O$$

La molècula de O_2 és una molècula radical amb dos electrons desaparellats que, pel seu caràcter paramagnètic, es veu obligada a intercanviar electrons amb altres molècules univalentment. Aquest fet fa que l'oxigen esdevingui una molècula poc reactiva i, a priori, sigui totalment inofensiva per a la vida: per a que l'O_2 oxidi una molècula no radical aquesta hauria d'oferir-li un parell d'electrons amb spins també paral·lels. Afortunadament per a tothom, els spins d'un parell d'electrons estan típicament sempre disposats de manera antiparal·lela i, conseqüentment, el principi d'exclusió de Pauli impedeixen a l'O_2 que pugui reaccionar amb moltes de les molècules biològiques no radicals. Ara bé, quan els nivells d'oxigen són superiors als corresponents en la seva metabolització aleshores aquest esdevé altament tòxic.

Aquest tercer apartat introductori presenta els fonaments de l'origen de la toxicitat del O_2 (Secció 3.1). Seguidament, s'expliquen les diferents fonts de ROS en organismes aerobis i com aquests poder conduir a l'estrès oxidatiu (Secció 3.2). Dins d'aquesta última secció, es presentaran les vies principals de generació i catabolisme de ROS (Secció 3.2.1), així com també les diferents característiques i conseqüències dels ROS (Secció 3.2.2) en organismes aeròbics.

3.1. La toxicitat de l'oxigen molecular: les espècies reactives de l'oxigen

Malgrat la seva poca reactivitat, un excés d'O_2 resulta ser molt tòxic a nivell cel·lular. L'origen d'aquesta toxicitat va ser per primer cop resolta per Gerschman l'any 1954. Gerschman va relacionar per primer cop la toxicitat de l'oxigen en organismes vius amb els esdeveniments subjacents a la toxicitat induïda per la irradiació ionitzant en diferents sistemes biològics: "*it would appear that irradiation and O_2 poisoning produce some of their lethal effects through at least one common mechanism, possibly that of the formation of free radicals*"[69]. Les hipòtesis de Gerschman es veien reforçades, entre d'altres, pel fet de que l'ús de compostos *scavenger* com el glutatió, l'etanol o la cisteïna ajudaven a minvar l'efecte tòxic de l'oxigen[69]. Gerschman no només va ser la primera en postular l'oxigen com el precursor de la toxicitat de l'oxigen, si no que també va ser indirectament qui va fer ús per primer cop dels raigs X com a banc de proves en l'estudi de l'estrès oxidatiu en organismes vius.

Les espècies químiques comunes als experiments d'irradiació i a la toxicitat de l'oxigen a les que Gerschman feia referència són les que avui en dia coneixem com *espècies reactives de l'oxigen* (*reactive*

oxygen species, ROS). El mot ROS inclou a totes les espècies químiques derivades de les diferents formes reduïdes o excitades de l'oxigen molecular, tan radicals com moleculars. Les formes radicals de ROS inclouen al ió superòxid ($O_2^{\bullet-}$) i al radical hidroxil ($^{\bullet}OH$), mentre que les formes no radicals inclouen al peròxid d'hidrogen (H_2O_2) i a l'oxigen singlet ($^1O_2$), entre d'altres.

Els ROS més comuns generats en processos biològics són el $O_2^{\bullet-}$, el H_2O_2 i el $^{\bullet}OH$. La manera com aquests processos generen ROS és mitjançant la successiva reducció univalent de l'oxigen molecular (Figura 14). En química, una manera de quantificar l'afinitat que té una substància per a acceptar electrons és mitjançant el paràmetre *potencial de reducció*, ΔV (el potencial de reducció de referència es considera el de l'hidrogen, que es defineix com 0). Així, una molècula amb baix potencial de reducció es pot considerar que te poca tendència a acceptar electrons i, per tant, té poc poder oxidant. El valor negatiu del potencial de reducció univalent de l'O_2 (-0.16 V, Figura 14) mostra la poca facilitat que aquest té per a ser reduït. Per tant, només els més potents donadors univalents d'electrons seran capaços de reduir l'O_2 cap a $O_2^{\bullet-}$ (Secció 3.2.1). En canvi, els valors positius dels potencials de reducció de l'$O_2^{\bullet-}$, del H_2O_2 i del $^{\bullet}OH$ (Figura 14) indiquen que aquestes espècies tenen facilitat per a ser reduïdes i, conseqüentment, són potents agents oxidants.

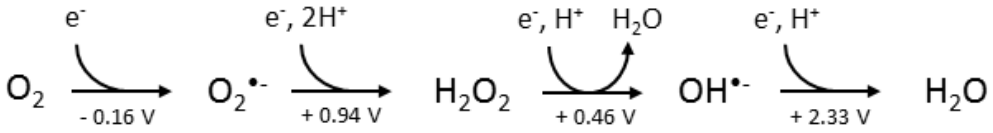

Figura 14 | *Seqüència de reducció univalent de l'oxigen molecular i potencials de reducció de cadascuna de les espècies implicades*[70].

3.2. ROS en organismes aeròbics

Els ROS són subproductes inevitables del metabolisme de l'oxigen. Malgrat la seva toxicitat, els ROS són essencials per a la vida, doncs participen en la senyalització cel·lular[71] i en diverses respostes immunològiques contra patògens[72]. No obstant, una excessiva acumulació de ROS en nivells superiors al seu catabolisme i a la capacitat de reparació cel·lular del dany provocat dona lloc al que s'anomena com *estrès oxidatiu*. Un excessiu desequilibri en l'homeòstasi dels ROS generarà progressiu dany en diferents components cel·lulars com les proteïnes, l'ADN i els lípids. El resultat d'aquest dany condueix a diferents patologies com el càncer, la diabetis, l'Alzheimer i el Parkinson, a més de la mort cel·lular i l'envelliment.

3.2.1. Generació i catabolisme de ROS en organismes vius

La generació de ROS en organismes vius pot sorgir de fons exògenes o endògenes. Agents externs com el tabac, la contaminació ambiental, la radiació ultraviolada o ionitzant o l'exposició a agents xenobiòtics són fonts exògenes de generació de ROS. En organismes vius, els ROS es generen en diferents sistemes cel·lulars com ara les NAD(P)H oxidases presents en la membranes plasmàtiques, els peroxisomes, el

reticle endoplasmàtic, els cloroplasts o la mitocòndria. Atès que la major part del consum d'oxigen és metabolitzat per la mitocòndria, aquest sistema és considerat una de les principals, si no la principal, font cel·lular de generació de ROS[73].

Els radicals $O_2^{\bullet-}$ i H_2O_2 es poden generar de manera endògena en processos no enzimàtics mitjançant la reducció de l'O_2 amb potents donants d'electrons com ara els centres metàl·lics o cofactors com les flavines o les quinones[71]. Aquests cofactors participen prominentment en les cadenes respiratòries a l'hora de transportar electrons i és per això que aquests sistemes esdevenen una important font de creació de ROS via la pèrdua accidental d'electrons al llarg de la cadena. Els enzims responsables de la generació de $O_2^{\bullet-}$ i de H_2O_2 són les NAD(P)H oxidases (NOX)[74], el flavoenzim ERO1[75], la xantina oxidasa (XO)[76] i el citocrom P450[77], entre d'altres. La generació endògena del radical $^{\bullet}OH$ sorgeix només de manera no enzimàtica via la catàlisi en presencia de ions metàl·lics com ara el ferro i el calci, segons les següents equacions[78]:

$$Fe^{3+} + O_2^{\bullet-} \rightarrow Fe^{2+} + O_2$$

$$Fe^{2+} + H_2O_2 \rightarrow Fe^{3+} + OH^- + OH^{\bullet}$$

la suma de les quals dona lloc a la coneguda reacció de Fenton:

$$O_2^{\bullet-} + H_2O_2 \rightarrow OH^{\bullet} + OH^- + O_2$$

L'oxidació dels clústers de $[4Fe-4S]$ i la posterior alliberació de ions de Fe en presència de $O_2^{\bullet-}$ i de H_2O_2 és un mecanisme conegut i ben establert en proteïnes que contenen ferro-sofre[79]. Aquests ions alliberats esdevenen una important font de Fe disponibles per a la catàlisi del radical $^{\bullet}OH$ via reacció de Fenton[79,80].

La cèl·lula disposa d'un ampli ventall de mecanismes antioxidants per tal de contrarestar els efectes adversos dels ROS. El catabolisme dels ROS pot ser tan enzimàtic com no enzimàtic. Els enzims antioxidants més importants són la superòxid dismutasa (SOD), la catalasa (CAT) i les tioredoxines (TRX). Entre els mecanismes no enzimàtics es troben els compostos *scavenger* de ROS com ara el glutatió, la vitamina C i E, els flavonoides i els carotenoides, entre d'altres.

3.2.2. Reactivitat, concentració i dany generat pels ROS

Els potencials de reducció de la Figura 14 assenyalen els diferents graus de reactivitat dels ROS. L'$O_2^{\bullet-}$ és una espècies moderadament reactiva ($\Delta V = +0.94$ V), amb un temps de vida mig ($T_{1/2}$) entre 1 i 4 µs i amb una distància de migració de al voltant de 30 nm. En canvi, el H_2O_2 és una molècula no radical amb menor reactivitat que l'$O_2^{\bullet-}$ ($\Delta V = +0.46$ V). Aquesta poca reactivitat i la seva naturalesa no radical permet al H_2O_2 a migrar grans distàncies i, fins i tot, traspassar membranes biològiques a través de les aquaporines. Per això el H_2O_2 participa en molts casos com a molècula transmissora de senyals cel·lulars.

El temps de vida mig i la distància de migració del H_2O_2 van més enllà de 1 ms i de més d'1µm, respectivament. Per últim, l'espècie més reactiva de totes és el radical $OH^{\bullet}$ ($\Delta V = +2.33$ V). El temps de vida mig i la distancia de migració del radical $OH^{\bullet}$ són, respectivament, 1 nm i 1 ns aproximadament[81–83]. Donat que no existeixen mecanismes enzimàtics cel·lulars per a la detoxificació del $OH^{\bullet}$, la sobreproducció d'aquest radical és especialment perillosa i pot induir la apoptosi cel·lular fàcilment[78].

Les concentracions cel·lulars de ROS són molt difícils de determinar, donat que la vida mitja d'algunes espècies és extremadament curta i la localització d'aquestes depèn molt del lloc on es generin. No obstant, per al cas del H_2O_2 i el $O_2^{\bullet -}$, encara es poden trobar alguns valors orientatius. Les concentracions estimades de $O_2^{\bullet -}$ i H_2O_2 dins de la matriu mitocondrial en condicions fisiològiques són de l'ordre de 10^{-10} i 10^{-8} M, respectivament[73].

Les molècules més afectades pels ROS són els lípids, el DNA, el RNA i, principalment, les proteïnes. La major part del dany és causat pel radical $OH^{\bullet}$ a causa de la seva gran reactivitat. La peroxidació de lípids induïda per l'atac de ROS dona lloc a una disminució de la permeabilitat de les membranes cel·lulars i causa dany a les proteïnes de membrana. El dany al DNA i al RNA s'esdevé a través de trencaments simples i dobles, alteracions en les bases i sucres que el conformen i l'enllaç amb altres molècules. El dany en proteïnes per efecte de l'atac de ROS dona lloc a l'oxidació de cisteïnes i metionines, a la reducció de ponts disulfur, a oxidacions i peroxidacions de les cadenes laterals, a carbonilacions, a modificacions en grups prostètics o en clústers de metalls, a l'encreuament entre proteïnes i a la fragmentació de pèptids[80,84,85].

Objectius

Capítol 1

Caracterització de les propietats mitigadores del dany per radiació de la uridina i avaluació de la seva aplicació en els experiments de MX.

Els objectius del Capítol 1 són:

- Estudi de les possibles propietats mitigadores de la uridina contra el DR en MX.
- Trobar les condicions experimentals òptimes en les que la uridina actuï, de manera significativa, com a compost scavenger en MX.
- Comparar els resultats obtinguts en MX amb altres estudis similars del camp.
- Preparació dels resultats de MX per al redactat d'una publicació científica.

Capítol 2

Caracterització de les propietats mitigadores del dany per radiació de la 5-metil uridina, citidina i citosina i avaluació de l'aplicació d'aquestes en experiments de SAXS.

Els objectius del Capítol 2 són:

- Extensió dels resultats obtinguts amb la uridina en altres nucleòsids i bases nitrogenades pels experiments de SAXS.
- Comparació dels compostos *scavenger* objecte d'estudi amb els compostos més utilitzats en els experiments de SAXS, en particular contrast, col·lecció de dades a angles alts, etc.
- Exploració de les noves possibilitats que ofereixen els compostos estudiats.
- Preparació dels resultats obtinguts per al redactat d'una publicació científica.

Capítol 3

Caracterització de les propietats mitigadores del dany per radiació de l'hidrogel peptídic Fmoc-CF en cristalls de lisozim.

Els objectius del Capítol 3 són:

- Estudi del DR en cristalls de lisozim crescuts en presència de l'hidrogel Fmoc-CF.
- Trobar les condicions experimentals òptimes en les que l'hidrogel Fmoc-CF actuï, de manera significativa, com a compost scavenger en MX.
- Optimitzar la metodologia per a l'anàlisi de les dades experimentals obtingudes a temperatura ambient.
- Preparació dels resultats obtinguts per al redactat d'una publicació científica.

Capítol 4

Caracterització enzimàtica i estructural de la forma "activada" de la hAR, present en condicions d'estrès oxidatiu, mitjançant la irradiació amb raigs X.

Els objectius del Capítol 4 són:

- Caracterització cinètica de la hAR irradiada amb raig X.
- Trobar quina és la dosi absorbida màxima tolerada per l'enzim en solució compatible amb els resultats enzimàtics obtinguts.
- Caracterització dels inhibidors de la hAR amb l'enzim irradiat.
- Comparar els resultats obtinguts amb la bibliografia del camp. Justificació que la irradiació amb raigs X produeix efectes sobre la proteïna similars a les produïdes per les condicions d'estrès oxidatiu.
- Trobar les possibles modificacions específiques que han donat lloc a canvis en les constants cinètiques de l'enzim.
- Proposar un mecanisme per als canvis enzimàtics.
- Preparació dels resultats obtinguts per al redactat d'una publicació científica.

Capítol 1

Uridine as a new scavenger for synchrotron-based structural biology techniques

The results presented in this chapter are part of the work published in:

Journal of Synchrotron Radiation. (2017). **24**, 53-62. DOI: 10.1107/S1600577516018452

Authors: Crosas, E.*, **Castellví, A**.*, Crespo, I., Fullà, D., Gil-Ortiz, F., Fuertes, G., Kamma-Lorger, C. S., Malfois, M., Aranda, M. A. G. & Juanhuix, J.

*These authors contributed equally to this work

Introduction

Many compounds are described to have antioxidant properties, counteracting the effects of ROS on biological macromolecules. Interestingly, uridine, the ribonucleoside of the pyrimidine base uracil and one of the four standard nucleosides which constitute RNA, is found at high concentrations in the cytosol of *D. radiodurans*[86], together with other bases, metabolites and peptides. This extremophile bacterium can withstand ionizing radiation up to 12 kGy although its DNA is as sensitive to ROS attack as that of other organisms which cannot withstand 12 kGy without damage[86]. The key factor in *D. radiodurans* ability to survive under extreme levels of irradiation is the persistence of a functional DNA repair system due to the presence of a collection of compounds in the cytosol[86–88]. Uridine reacts with solvated electrons and with hydroxyl and hydrogen radicals[89]. In combination with manganese and orthophosphate, uridine contributes to protecting the proteome, and in particular the DNA repair enzymes against exposure to high levels of radiation[86]. However, in spite of the known scavenging properties of uridine against radicals, to the best of our knowledge this compound has never been studied as a potential scavenger for SAXS or MX experiments.

Here is presented the MX part concerning the results published by Crosas *et. al* (2017)[61]. In this work, Crosas and co-workers demonstrated that uridine, ranging from 5 to 100 mM, could be considered as a suitable scavenger for SAXS experiments at room temperature. The absorbed dose at Rg/Rg_0 = 1.1 in lysozyme solutions containing 100 mM uridine was reported to be up to 25-fold higher than that without

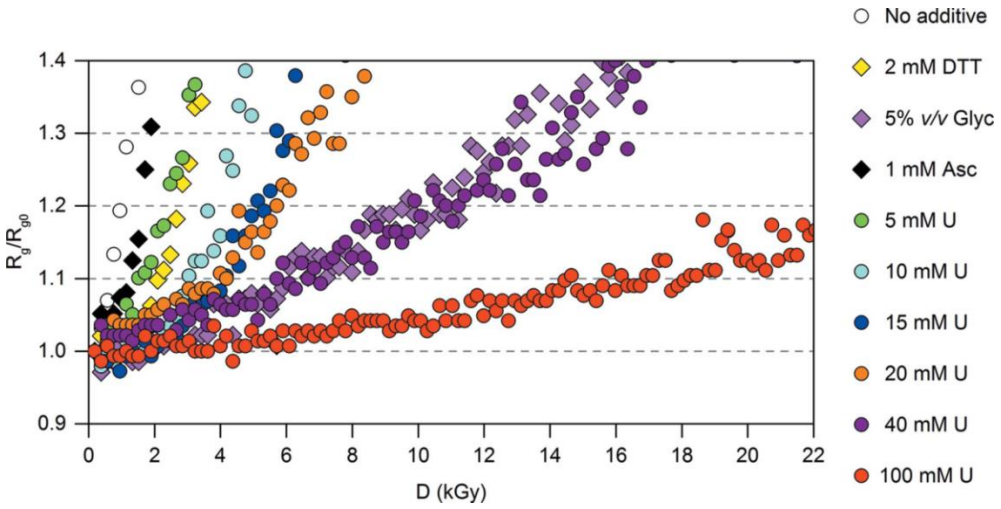

Figure 15 | *Evolution of the ratio of radius of gyration R_g of lysozyme at a given dose with respect to the initial value R_{g0} (first frame), R_g/R_{g0}, with absorbed dose, in the presence of different additives. Samples of 7.2 mg/ml lysozyme were analyzed in 40 mM sodium acetate, pH 3.8, 150 mM sodium chloride. Multiple frames of 0.035 s exposure time were recorded and added per point. Measurements were performed in presence of 2 mM DTT, 5% v/v glycerol, 1 mM ascorbic acid, and increasing concentrations of uridine (5, 10, 15, 20, 40, 100 mM). Samples without any additive were also analyzed as negative controls. All the samples were measured in static mode (DTT: dithiothreitol; Asc: ascorbic acid; Glyc: glycerol; U: uridine)*[61]*. Figure extracted from Crosas et al. (2017)*[61].

any additive (Figure 15). In addition, the scavenging effect of 40 mM uridine was shown to be similar to that of 5% (v/v) glycerol, and greater than 2 mM DTT and 1 mM ascorbic acid, another well-known scavengers usually employed by the SAXS community (Figure 15).

The following is presented the use of uridine as a scavenger for the mitigation of radiation damage in lysozyme crystals at room temperature. The scavenging properties of uridine are similar, or better in some cases, to those of ascorbate[90] and sodium nitrate[91].

Materials and methods

Sample preparation

Chicken egg-white lysozyme (cEWL) was obtained from Sigma-Aldrich (L6876). The protein concentration in the corresponding buffer was determined by measuring the absorbance at 280 nm using an extinction coefficient of 2.64 ml mg^{-1} cm^{-1}. Crystals for the MX experiments were grown according to the method given in De la Mora *et al*. (2011)[91] at different concentrations of lysozyme ranging between 50 mg ml^{-1} and 80 mg ml^{-1}. The mother liquor (100 mM sodium acetate, 10% sodium chloride at pH 4.7) does not have any scavenging properties. Only crystals with a size of around 100 × 100 × 50 μm were harvested for use in the experiments (see Supporting Table 4 for sizes of the individual crystals). The crystals of lysozyme used for diffraction at room temperature with uridine were prepared by soaking them in mother liquor containing three different concentrations of uridine (200 mM, 500 mM and 1M). The uridine solutions replaced the corresponding amount of water in the mother liquor. The soaking time, which was not found to be affect the outcome of initial test experiments, was varied from few seconds to a few minutes. Crystals were introduced inside a polyimide capillary of 1 mm internal diameter (Goodfellow, IM307100) with the aid of a pipette. The crystals were adhered to the tube wall by removing the excess solution around them. Sample dehydration was prevented by keeping some solution around the crystal and by a solution reservoir pipetted near the crystal. The capillary was mounted on a SPINE magnetic cap compatible with the diffractometer. The crystals used for diffraction at 100 K were prepared as above with 500 mM and 1 M of uridine and with the addition of 25% (v/v) ethylene glycol as a cryoprotectant in the soaking solution.

Data collection

Diffraction data collections at room temperature and at 100 K were performed in the BL13-XALOC beamline at the ALBA synchrotron[92] using a Pilatus 6M photon-counting detector (DECTRIS, Baden, Switzerland) . The beam was Gaussian-shaped and was set at 12.661 keV photon energy (λ =0.979 Å). The sample-detector distance was adjusted to collect the data sets at a resolution of 1.4 Å and 1.1 Å for experiments at room temperature and at 100K, respectively.

Eleven crystals soaked at different uridine concentrations (four crystals without, four 200 mM and three 500 mM uridine) were irradiated at room temperature at an absorbed dose rate of 13.8 kGy s^{-1} (Supporting Table 4). Seven crystals (four crystals without uridine, three soaked at 1 M of uridine) were irradiated at

room temperature at an absorbed dose rate of 20.0 kGy s^{-1}. Finally, seven more crystals (three crystals without uridine, one soaked at 500 mM and three soaked at 1 M uridine) were irradiated at 100K at a dose rate of 90 kGy s^{-1}. The flux to calculate the dose was measured using a calibrated PIN Si diode at the sample position. The beam had a Gaussian shape and was defocused to a FWHM dimension of 86-100 µm (h) × 78-85 µm (v) as measured by a Ce:YAG fluorescent screen at the sample position. Complete data sets of 90 images were collected with an angle increment per image of 1°. The crystals at 100 K were 'burned' between data sets with an absorbed dose of 1230 kGy at a dose rate of 205.2 kGy s^{-1}. The crystals were rotated by 90° during the 'burns'. Burns were not performed for crystals at room temperature. For a given crystal, the successive data sets with increasing dose were collected starting from the same initial angle. The space group for all crystals was $P4_32_12$. All crystals had cell dimensions differing less than 1 Å to those of the crystals without uridine at room temperature, that is, $a = b = 79.2$ Å and $c = 37.9$ Å (Supporting Table 5 and Supporting Table 6).

Absorbed dose calculation

The doses for MX experiments were calculated with *RADDOSE-3D*[7]. The crystal is assumed to have a cubic shape with dimensions measured by the on-line microscope of the beamline. As the FWHM beam size was somewhat smaller than the size of the crystals, the effective absorbed dose was in general slightly smaller than the values calculated by RADDOSE-3D. Nevertheless, the relative comparison of the radiation hardness was possible since the crystals were of similar size and were illuminated using the same protocol.

MX data processing

All datasets at room temperature in MX experiments were indexed and integrated between 50 Å and 2 Å using *XDS*[93] (Supporting Table 5). Data statistics for each dataset were extracted from the output files generated by *XDS*. The values of the relative diffraction intensity I/I_0 and the R-damage factor R_d[94] were extracted from XDSSTAT. Data sets were scaled and structure factors found by using *Aimless*[95] and TRUNCATE[96], respectively. Molecular replacement was not necessary since the initial PDB model used for lysozyme (1BWH)[97] has the same space group and similar unit cell dimensions as our data. The first refinement of the structure was performed *via* rigid-body minimization followed by restrained refinement using *REFMAC5*[98]. Subsequently, preliminary structures continue to be refined iteratively through manual adjustment using *COOT* [99] (according to the allowed values in Ramachandran plot, with a good fit on $2F_o - F_c$ maps and with no significant peaks in $F_o - F_c$ maps) and then through restrained refinement until the crystallographic R value and R_{free} were as low as possible. Water molecules were added and replaced by using *REFMAC5*. The refinement was completed when $R_{work}<0.20$ and $R_{free}<0.25$. All the data sets of the same crystal were Wilson scaled together *via SCALEIT* [100]. Difference Fourier maps ($F_{obs,n}$ - $F_{obs,1}$, $\alpha_{calc,1}$) were calculated between each dataset n and the initial data set using the phases of the fresh, not previously irradiated, data set $\alpha_{calc,1}$, as described by Southworth-Davies *et al.* (2007)[101]. All programs mentioned here

belong to the *CCP4* programming suite[102]. Data sets collected at 100K were integrated between 50 Å and 1.7 Å, and processed using the same protocol.

Results

Global damage

Global radiation damage is characterised here by using three metrics already mentioned: the dose, $D_{1/2}$, required to reduce the mean intensity of all reflections in a data set to half of the value of the first data set; the damage *R*-factor per image, R_d, as defined by Diederichs (2006)[94]; and the coefficient of sensitivity to absorbed dose, $S_{AD} \equiv 8\pi^2(\Delta B/\Delta D)$[38,103], where the ratio $\Delta B/\Delta D$ quantifies the increase of the mean *B*-factor induced by an additional dose. The experiments performed at 100 K show no scavenging effect of uridine in lysozyme crystals (data shown in Supporting Figure 35 and Supporting Table 6). Therefore, all results reported hereinafter are for measurements made at room temperature. All the metrics indicate an evolution of the crystal damage with dose that depends on the concentration of the uridine, as shown in Figure 16. The protective effect of uridine increases with increasing concentration for all metrics. The scavenging effect of uridine at a given dose *D* is quantified *via* the enhancement factors defined as the ratio of the metrics calculated with and without uridine $D_{1/2,U}/D_{1/2,0}$, $R_{d,U}/R_{d,0}$ at 1 MGy and $S_{AD,U}/S_{AD,0}$ (Table 1, particular statistics for individual crystals are shown in Supporting Table 5). Three other metrics to evaluate the radiation damage effects and the scavenging properties of uridine were tested but disregarded. The increment of the normalized R_{merge} and the normalized mosaicity with absorbed dose show consistent trends compared with other metrics, but the errors were too high to provide reliable values. The relative expansion of the unit cell parameters is inconsistent as it does not show a defined pattern for all crystals under the same conditions, as has been reported in previous studies. The global radiation damage suffered by the crystals at room temperature not soaked with uridine does not show a dependence on dose rate, in agreement with results reported by Kmetko *et al.* (2011)[38] and Warkentin *et al.* (2012)[104], except for at high doses (above 1.2 MGy approximately), where all significant metrics in Figure 16 indicate a slower structural damage at higher rates (20 kGy/s, light grey points) compared to lower rates (13.8 kGy/s, orange points).

Specific damage

Specific radiation damage was assessed using the difference Fourier maps calculated between the first data set and the second and third data sets, $(F_{obs,2} - F_{obs,1}, \alpha_{calc,1})$ and $(F_{obs,3} - F_{obs,1}, \alpha_{calc,1})$ respectively, for the non-soaked crystals (PDB codes 5L9J, 5LA5 and 5LA8 for structures derived from the first, second and third data set, respectively) and for the crystals soaked at 1 M uridine (PDB codes 5LAF, 5LAG and 5LAN) (crystals 12 and 16, Supporting Table 5). Each data set absorbed a dose of 0.36 MGy, and all were collected at a dose rate of 20 kGy/s. The $(F_{obs,3} - F_{obs,1}, \alpha_{calc,1})$ maps of both crystals show significant peaks for Cys30-Cys115, Cys64-Cys80, Cys76-Cys94 disulphide bonds and Met105 (Figure 17), but not for Cys6-Cys127 (data not shown). Beyond -4σ no significant peaks are observed for $(F_{obs,3} - F_{obs,1}, \alpha_{calc,1})$

maps. The $2F_o$-F_c and F_o-F_c maps of the crystals soaked at 1 M uridine do not reveal the presence of ordered uridine in the crystallographic structure.

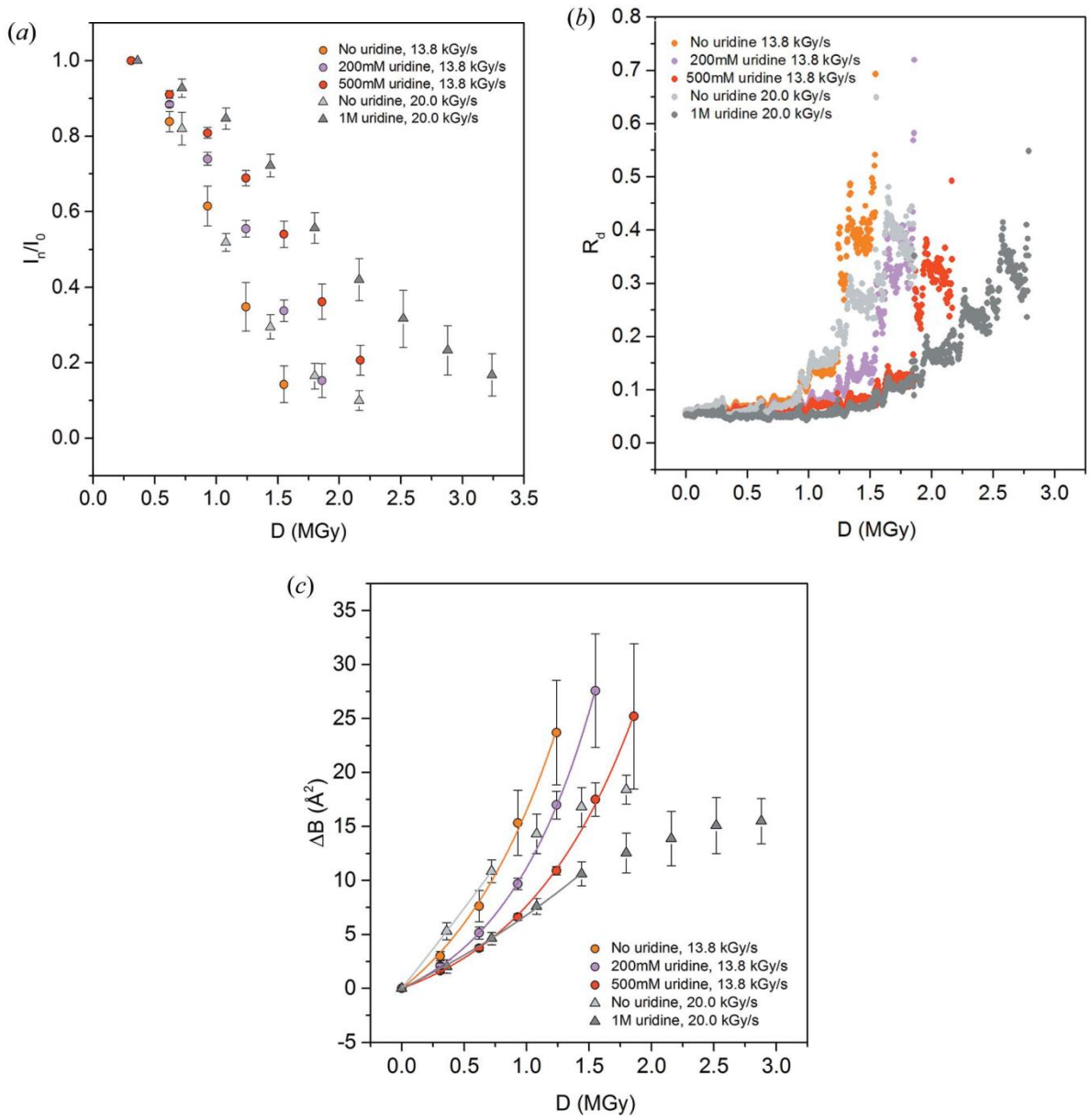

Figure 16 | *Evolution of radiation damage with absorbed dose on lysozyme crystals at room temperature monitored using different metrics. The dose D is defined as the total absorbed energy divided by the mass of the region of the crystal receiving nonzero dose (AD-ER), as defined by Zeldin et al. (2013)* [7]. *Crystals were soaked at different uridine concentrations, from none to 1 M, and diffraction data recorded at two different dose rates. (a) Decay of the mean normalized intensity I/I_1, calculated in the 50-2 Å. resolution range (b) Decay of the R-factor R_d with dose. R_d is calculated in the 50-2 Å. resolution range. For clarity error bars are not shown (data with error bars are plotted in Supporting Figure 36). (c) Evolution of ΔB as a function of dose. Lines show the fits of the experimental data using an exponential model* $\Delta B = B_0(e^{k\Delta D} - 1)$. *Results of the fits are shown in Table 1.*

Table 1 | *Radiation damage metrics (top) and derived enhancement factors (below) for uridine in MX experiments in lysozyme crystals without, with 200mM, with 500mM and 1M of uridine.* $R_{d,U}$ *factors are calculated at 1 MGy dose.* $\Delta B/\Delta D$ *and* S_{AD} *values are calculated using the approximation* $\Delta B = B_0(e^{k\Delta D} - 1) \approx B_0 k\, \Delta D$ *(valid at low doses).*

Sample, dose rate	$D_{1/2}$ (MGy)	$R_{d,U}$	$\Delta B/\Delta D$ (S_{AD}) (Å^2 MGy^{-1})
No uridine, 13.8 kGy/s	1.06	0.120	9.07 (0.11)
No uridine, 20.0 kGy/s	1.11	0.127	15.07 (0.19)
200 mM uridine, 13.8 kGy/s	1.32	0.072	5.32 (0.07)
500 mM uridine, 13.8 kGy/s	1.62	0.065	4.26 (0.05)
1000 mM uridine, 20.0 kGy/s	1.95	0.049	5.63 (0.07)
	$D_{1/2,U}/D_{1/2,0}$	$R_{d,U}/R_{d,0}$	$S_{AD,U}/S_{AD,0}$
200 mM uridine *vs* no uridine, 13.8 MGy/s	1.24	0.59	0.58
500 mM uridine *vs* no uridine, 13.8 MGy/s	1.52	0.55	0.47
1000 mM uridine *vs* no uridine, 20.0 MGy/s	1.76	0.38	0.37

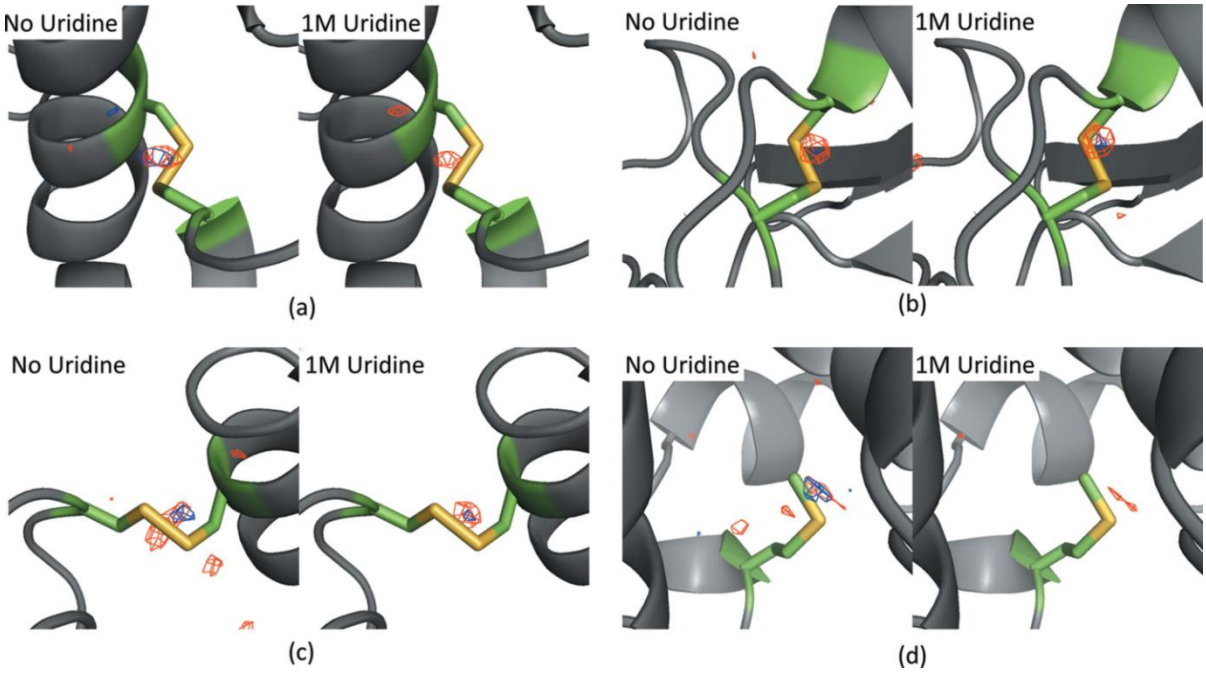

Figure 17 | *Comparison of the* ($F_{obs,2}$ - $F_{obs,1}$, $\alpha_{calc,1}$) *(blue) and* ($F_{obs,3}$ - $F_{obs,1}$, $\alpha_{calc,1}$) *(red) maps between a crystal without uridine (left figures) and a crystal with 1M of uridine (right figures) contoured at -4σ. (a) Cys30-Cys115. (b) Cys64-Cys80. (c) Cys76-Cys94. (d) Met105. Crystals used are 12 (no uridine) and 16 (1M of uridine in solution). Data were collected at room temperature. See Supporting Table 5 for diffraction statistics.*

Discussion

The significant global metrics consistently show an increasing scavenging effect of uridine as its concentration is increased in lysozyme crystals at room temperature. The enhancement factors $D_{1/2,U}/D_{1/2}$ and $S_{AD,U}/S_{AD}$ for 1 M uridine are 1.76 and 0.37, respectively. These values are comparable to the factors achieved by other scavengers previously reported for lysozyme crystals at room temperature, namely, ascorbate at 0.5 M minimum (factor 2 in $D_{1/2,U}/D_{1/2}$)[90] and sodium nitrate at 0.1 M (factor 0.47 in $S_{AD,SodiumNitrate}/S_{AD}$)[38]. These irradiation experiments are comparable in spite of the different protocols, variability of the crystals and the diverse X-ray beam properties, as shown by the obtained values of $D_{1/2}$. The value for $D_{1/2}$ obtained by Barker *et al.* (2009)[90] is 0.9 MGy at a dose rate of 2.8 kGy s^{-1}, which is in good agreement with our results of 1.06 and 1.11 MGy obtained at 13.8 and 20.0 kGy s^{-1}, respectively. The values of $D_{1/2}$ are consistent with the observation made by Warkentin *et al.* (2012)[104] on thaumatin crystals that radiation damage is not dependent on the absorbed dose rate at room temperature at the typical irradiation levels achievable at synchrotron beamlines. It is worth noting that the value of S_{AD} reported by Kmetko *et al.* (2011)[38] for control native lysozyme crystals at room temperature, 0.57 $Å^2$ MGy^{-1}, differs from the values 0.115 and 0.191 $Å^2$ MGy^{-1} obtained here at 13.8 and 20.0 kGy s^{-1}, respectively. The discrepancy may be explained by the differences in the experimental set up. Moreover, the use of S_{AD} at room temperature suffers from the lack of linearity of the relative increase of the *B*-factors with respect of the absorbed dose (Figure 16c). On the contrary, the use of S_{AD} at 100K is justified as *B*-factors increase linearly at low doses[103]. To better fit the evolution of the *B*-factors with dose at room temperature, we have assumed an exponential increase of the *B*-factor with dose, that is,

$$\Delta B = B_0(e^{k\Delta D} - 1)$$

where B_0 is the *B*-factor at close-to-zero dose, ΔD is the differential dose within data sets, and k is the sensitivity of the *B* factors to the dose. This equation reduces to the standard linear fit at low doses or low sensitivities, i.e.

$$\Delta B \approx kB_0\,\Delta D$$

as used for data sets collected at 100 K. Results using an exponential fit and its linear approximation at low doses for data sets collected at room temperature are shown in Table 1.

Lysozyme does not show significant specific radiation damage at room temperature (Supporting Figure 37). Only some differential electron density in residue Met105 and in 3 out of 4 disulphide bonds was barely noticeable in difference maps ($F_{obs,2} - F_{obs,1}, \alpha_{calc,1}$) contoured at -4σ (Figure 17). Conversely, global damage in MX experiments at room temperature is much more apparent, as seen comparing the effects in Figure 16 and Figure 17, respectively.

Capítol 2

Expanding the small angle scattering experiments to low-molecular weight and low-concentration protein samples

The results presented in this chapter are pending to be submitted in a scientific jounal.

Authors: **Castellví, A**., Pascual-Izarra, C., Eva Crosas, E., Malfois, M., Juanhuix. J.

Introduction

With the continuous advances on automated sample handling and the appearance of CCD and, especially, PAD detectors in synchrotron beamlines, Small Angle X-ray Scattering (SAXS) has become a popular low-resolution structural technique for the characterization of biological macromolecules in solution. BioSAXS provides low-resolution information at nanoscale on the shape, conformation and assembly state of a wide range of proteins, nucleic acids and macromolecular complexes with molecular weights ranging from 5 kDa to 1 MDa[105]. This technique also offers useful information about flexible systems and is compatible with sample environments close to physiological conditions. In spite of being a low-resolution technique compared to other structural biology techniques such as macromolecular crystallography or cryo-electron microscopy, SAXS measurements provide access to some aspects that other high-resolution techniques cannot reach easily like the protein flexibility, the oligomerization state, the influence on buffer conditions or the particle size distribution, among others[44,106–109].

The total intensity of the scattered beam as collected by the detector in SAXS experiments is expressed as the sum of the scattered beams from every type of particle i, within the irradiated sample

$$I(q) = S(q)\sum_{i}^{n}(\Delta\rho_i V_i)^2 P_i(q) \qquad \text{(Eq. 5)}$$

where the angular variable is included in the scattering vector $q = 4\pi \sin\theta/\lambda$, being 2θ and λ the scattering angle and the wavelength of the incident X-ray beam, respectively. The dependence of the scattering intensity on the structure for each type of scatterer is incorporated through the form factor $P_i(q)$, and represents the target of the SAXS experiments as used to characterize the biological structures[110]. The total scattering intensity also depends on the volume of each particle V_i, the difference in the electronic scattering density (electronic contrast) between the particle and its surrounding solvent $\Delta\rho_i$, and the structure factor $S(q)$, which provides all information about interparticle distances. The above expression of the scattering intensity is greatly simplified when the irradiated sample is monodisperse and the scattering particles do not interact between them, so that the structure factor is no longer influencing the scattering intensity. In this case there is only one type of particle and the structure factor $S(q)$ reduces to 1 at all angles so that the general expression of the scattering intensity (Eq. 5) simplifies to:

$$I(q) = N(\Delta\rho V)^2 P(q)$$

To maintain monodisperse and aggregate-free samples throughout the X-ray data collection is one of the most important challenges for SAXS community since radiation damage, which causes aggregation, unfolding, and fragmentation[52,55,110], is the main bottleneck for these conditions.

A thoroughly planned SAXS experiment should include a plan to control and mitigate the radiation damage effects. There are several strategies for the mitigation of radiation damage in SAXS experiments (see Section 2.1). One of these strategies is the use of additives that scavenge the radiation-induced radical species produced in the water solution, which are accountable for most of the structural damage of the

protein sample. Although radical scavengers can interfere in the stability of the sample or can reduce the electronic contrast of the protein in solution, they are widely used to increase the photon flux accepted by the sample before significant radiation damage occurs.

In addition to radiation damage one has also to take into account those aspects that can cause poor signal-to-noise ratio during data collection and therefore can also affect to the final quality of the experimental data. That is, signal from X-ray scatters is more difficult to collect from low molecular weight samples than for high molecular weight. Also measurements from highly diluted samples (e.g. 1 mg/mL for a 5 kDa protein) are difficult to measure with high precision. Conversely, high concentrated samples provide us more signal but then inter-particle interactions can appear and interfere in the scattering profile at low angles[111]. Furthermore, signal-to-noise ratio also depends on the beamline characteristics and therefore the optimal sample concentration for a specific molecular weight only can be known by in situ inspection of the collected data during the beamtime.

In the following the use of uridine as a scavenger for SAXS experiments[61] is expanded to other nucleosides and its nitrogenous bases. Only those nucleosides and nitrogenous bases easily solubilized in water up to at least 0.5 M were considered to be tested as scavengers: the selected compounds were 5-methyl uridine, cytidine, uridine and cytosine.

Materials and methods

Sample preparation

Chicken egg-white lysozyme (HEWL) was obtained from Sigma-Aldrich (L6876) as a lyophilized powder and was dissolved in mQ water. Buffer exchange was performed by dialysis (overnight) in 40 mM sodium acetate pH 3.8, 150 mM NaCl.

Bovine Liver Catalase (BLC) was also obtained from Sigma-Aldrich (C30) as a crystalline suspension in water containing 1% of thymol. BLC crystals were pelleted by centrifugation and diluted in 50 mM sodium phosphate buffer pH 7. BLC crystals were dissolved by warming the sample at 30ºC with slightly agitation during one hour. The BLC solution was further purified with a size exclusion chromatography (SEC) column previously equilibrated with 50 mM sodium phosphate pH 7.

Human Aldose Reductase (hAR, AKR1B1) vas purified as previously described[112] and was subjected to a further purification step in a SEC column previously equilibrated in 20 mM Tris pH 8, 250 mM NaCl.

The alpha-spectrin SH3 domain (SH3-SPC) was purified as previously described[113] and was subjected to a final purification step with a SEC column previously equilibrated in 10 mM citric acid pH 3, 150 mM NaCl.

All proteins were centrifuged at maximum speed and then quantified before final sample preparation. Each protein concentration in its corresponding buffer was determined spectrophotometrically at 280 nm.

Uridine, 5-methyl uridine, cytidine, cytosine were obtained from Sigma-Aldrich (U3750, 535893, C122106 and C3506, respectively). All nucleosides and the nitrogenous base were dissolved at 0.5 M in the corresponding dialysis or SEC buffer according to the considered protein. Glycerol stock solutions were diluted also with buffers from dialysis or SEC purifications.

All samples were freshly prepared and were housed in a 1.8 mm quartz capillary (1.7 mm internal diameter, cell wall thickness 50 μm) and held at room temperature.

SAXS data collection

SAXS data from BL11-NCD-SWEET beamline at ALBA synchrotron was obtained using a Pilatus 1M photon-counting detector (DECTRIS, Baden, Switzerland).

The beam at the sample position for HEWL samples was 0.349 mm (horizontal) × 0.379 mm (vertical), the incident photon flux was 7.56×10^{11} photons/s at 12.4 keV (λ = 0.999 Å) and the sample to detector distance was 2.291 m. The beam at the sample position for BLC, hAR and SH3-SPC samples was 0.566 mm (horizontal) × 0.420 mm (vertical), the incident photon flux was 1.08×10^{12} photons/s at 12.4 keV (λ = 0.999 Å) and the sample to detector distance was 2.460 m. For all samples, 2000 frames of 0.1 s exposure time were recorded. The experiments were performed in static mode without beam attenuation to speed-up radiation damage on the sample.

SAXS data processing

All SAXS data was normalized by the intensity of the electron current and by the protein concentration. SAXS data manipulation, buffer subtraction and all structural parameters were performed with the *ATSAS* package[114]. *Rg* (from the Guinier approximation), *I(0)* and *C* values were calculated from the *PRIMUS* software[115] and from the CorMap test[116]. In order to improve the accuracy in the *Rg, I(0)* and *C* values these parameters were calculated from the average of a set of consecutive frames. The number of consecutive frames for those calculations was 3 for samples without additives, and 11 for samples with additives. All *Rg* (from Guinier approximation), *I(0)* and *C* values were computed by using a Python-based script. Pair distribution functions were calculated with GNOM[117]. Shannon Channels and Whittaker-Shannon interpolation polynomials were calculated with SHANUIM[118]. Modellings were performed with DAMMIN[119] and the normalized spatial discrepancy (NSD) values were obtained with SUPCOMB[120].

Absorbed dose calculation

All dose calculations were calculated with RADDOSE-3D[121].

Results

Radiation damage in the buffer solutions

The experimental SAXS profiles as a function of dose from the buffered solutions containing 5-methyl uridine, cytidine, cytosine and uridine at 100 mM are plotted in Figure 18. For each solution, the collected SAXS profiles show differences during the irradiation as a consequence of radiation damage (Figure 18). Therefore, this effect on the buffer solutions containing the tested compounds at 100 mM has to be taken into account when buffer subtraction is performed. That is, all buffer subtractions have to be performed with the same number of frames in the buffer and protein-containing SAXS profiles.

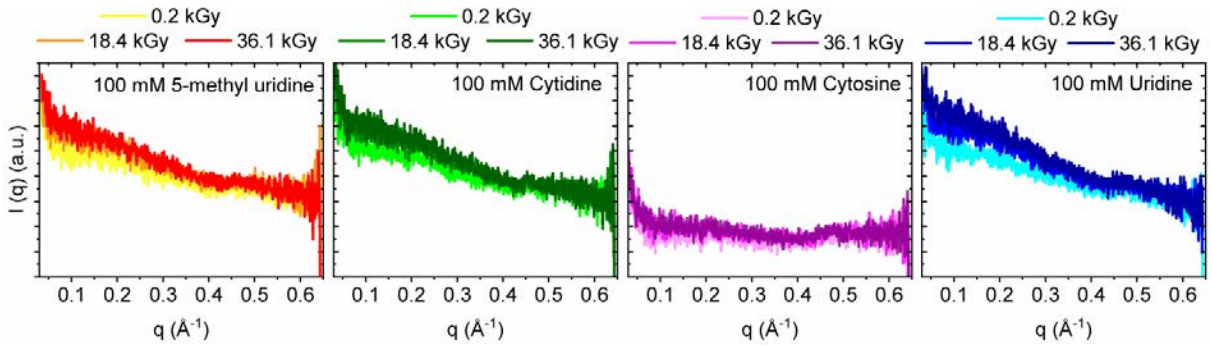

Figure 18 | *Buffer solutions containing 5-methyl uridine, cytidine, cytosine and uridine at 100 mM are affected by radiation damage. The buffered solutions were composed by 40 mM sodium acetate, pH 3.8, 150 mM sodium chloride and 100 mM of the tested compound.*

The new compounds possess strong scavenging properties against radiation damage

The scavenging effect of 5-methyl uridine, cytidine, cytosine and uridine at different concentrations is monitored though the increase of the normalized radius of gyration, $Rg\,/Rg_0$, the normalized intensity at zero angle, $I(0)\,/I(0)_0$, and the number of consecutive experimental points in the n-th frame below or above the experimental points in the first frame, C (Figure 19). Nucleosides and the nitrogenous base concentrations in Figure 19 range from 25 mM to 100 mM. For comparison, it is also monitored the scavenging effect of 100 mM and 678 mM glycerol (Figure 19). Based on the three different metrics described above, three different critical doses were defined: i) the dose where $Rg\,/Rg_0$ reaches an increment of 5%, ii) the dose where $I(0)\,/I(0)_0$ reaches an increment of 5% and iii) the dose where seven consecutive data frames reach the $C = 17$ condition ($C \geq 17$ corresponds to the condition where the hypothesis of similarity of two different frames could be rejected (CorMap test, $n = 701$, $C \geq 17$, $P < 0.01$)[56]). For each sample, the frames where the critical doses are reached and their corresponding scavenging factors are tabulated in Table 2 (see expanded table in Supporting Table 7). The maximum scavenging factor for the tested nucleosides and the nitrogenous base at 100 mM ranges from 15.8 to 20.45 (Rg/Rg_0 metric), from 12.36 to 19.73 ($I(0)/I(0)_0$ metric) and from 8.82 to 16.18 (CorMap test).

All these latter scavenging factors are bigger than that from 678 mM glycerol condition. The scavenging factor for 678 mM glycerol is 4.55 (Rg/Rg_0 metric), 4.55 ($I(0)/I(0)_0$ metric) and 4.64 (CorMap test).

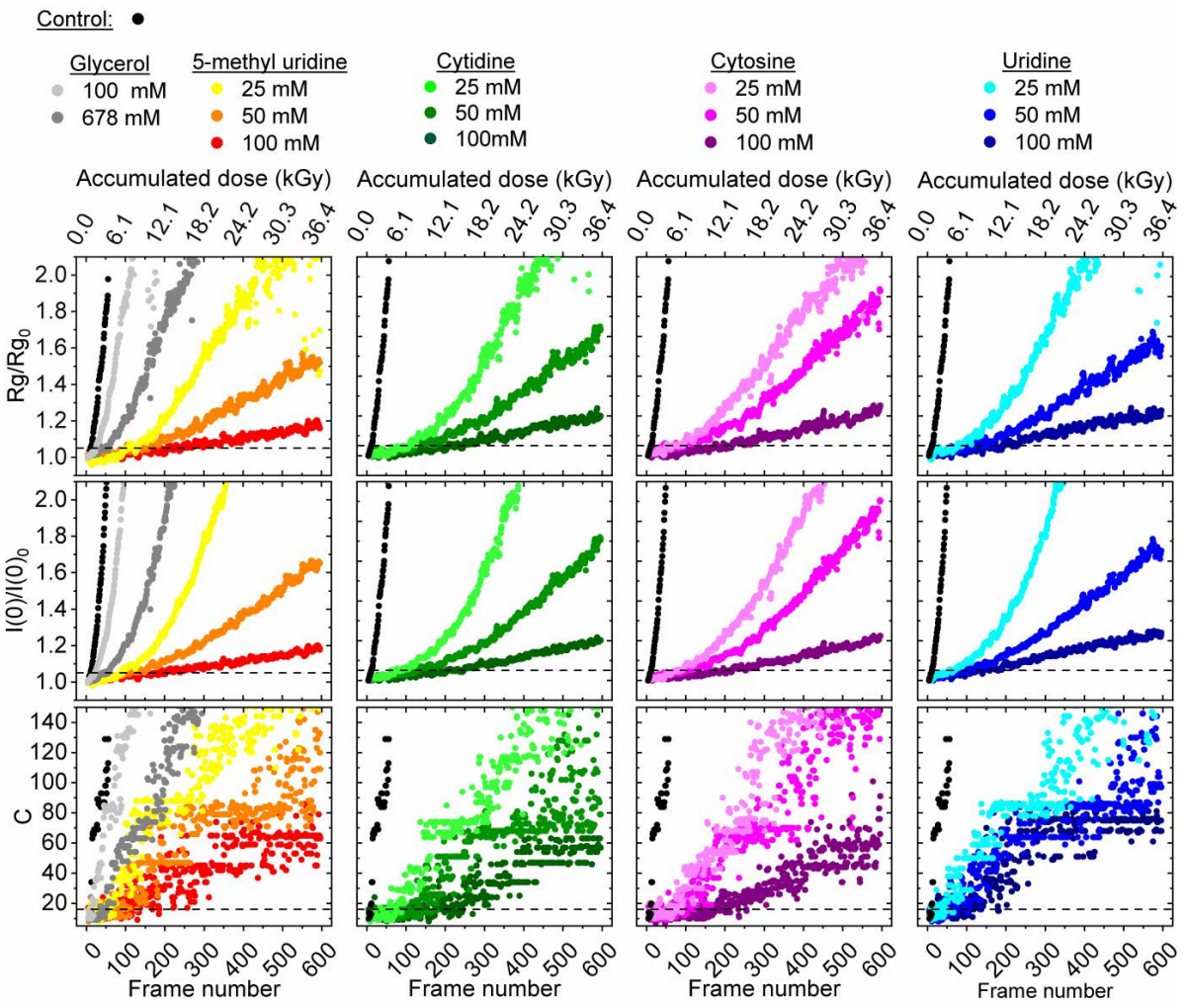

Figure 19 | *The addition of 5-methyl uridine, cytidine, cytosine and uridine reduces the radiation damage. The scavenging effect of 5-methyl uridine, cytidine, cytosine, uridine (from 25 to 100 mM) and glycerol (at 100 and 678 mM) is monitored though the increase of the radius of gyration,* Rg/Rg_0*, the normalized intensity at zero,* $I(0)/I(0)_0$*, and the* C *value as a function of the accumulated dose and frame number. Dashed lines represents the limits where* $Rg/Rg0 = 1.05$*,* $I(0)/I(0)_0 = 1.05$ *and* $C = 17$*. Sample conditions for all samples: HEWL at 7.00 mg/ml in 40 mM sodium acetate (pH 3.8), 150 mM sodium chloride and 25-678 mM of scavenger.*

The pair distribution functions were calculated for those samples in presence of 5-methyl uridine, cytidine, cytosine and uridine at 100 mM (Supporting Figure 38) by using all data frames below the three different critical doses. All pair distribution functions in Supporting Figure 38 and all calculated structural parameters from them (Supporting Table 8) can be considered the same independently of the considered metric and the used scavenger. Structural parameters in Supporting Table 8 are in good agreement with those reported by Crosas *et al.* (2017)[61].

Table 2 | *Frames where the critical doses were reached and their corresponding scavenging factors. All the tabulated frames arise from the intersection between a 4th order interpolation polynomial and the threshold conditions in which the critical doses are defined. The number of frames in parenthesis correspond to the second set of seven consecutive data frames with* $\boldsymbol{C = 17}$.

Sample	Frames			Scavenging factors		
[HEWL] = 7.00 mg/ml	$Rg/Rg_0 = 1.05$	$I(0)/I(0)_0 = 1.05$	CorMap test	$Rg/Rg_0 = 1.05$	$I(0)/I(0)_0 = 1.05$	CorMap test
Control	11	11	11	1	1	1
100 mM glycerol	25	29	18	2.27	2.64	1.64
678 mM glycerol (5% v/v)	50	50	51	4.55	4.55	4.64
100 mM 5-methyl uridine	225	177	97	20.45	16.09	8.82
100 mM cytidine	223	217	178	20.27	19.73	16.18
100 mM cytosine	198	202	177	18.00	18.36	16.09
100 mM uridine	174	136	42 (117)	15.82	12.36	3.82 (10.63)

Variations in the electronic contrast

The decrease of I(0) as a consequence of decreasing the electronic contrast when 5-methyl uridine, cytidine, cytosine, uridine and 678 mM glycerol at 100 mM were used is shown in Figure 20. The decrease of I(0) due to the use of 5-methyl uridine, cytidine, cytosine, and uridine at 100 mM ranges from 9 to 16% while for 678 mM glycerol is 28%.

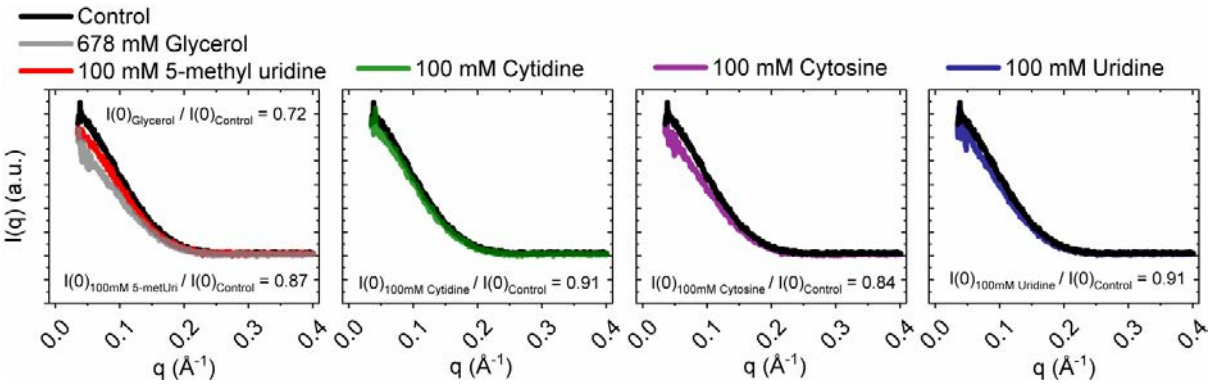

Figure 20 | *Samples containing 5-methyl uridine, cytidine, cytosine and uridine at 100 mM have more electronic contrast than samples containing 678 mM glycerol. Buffer subtracted data extrapolated to zero concentration for samples containing 5-methyl uridine, cytidine, cytosine, uridine at 100 mM and 678 mM glycerol. HEWL concentrations of 2.13, 5.17 and 7.00 mg/ml were used for the extrapolation to zero concentration.*

The accessibility to more useful information

The scavenging effect of 100 mM 5-methyl uridine was tested in human Aldose Reductase (hAR), Bovine Liver Catalase (BLC) and the SH3 domain of Spectrin (SH3-SPC). These tested proteins, in conjunction with HEWL, were chosen based on their wide range of molecular weight (from 7 to 240 kDa) and their buffer acidity (from pH 3.0 to 8.0). The chosen metric to monitor radiation damage in presence of 100 mM 5-methyl uridine and without the presence of additives (control) was Rg/Rg_0. As it is shown in Figure 21 (left panels) the addition of 100 mM 5-methyl uridine prevents to radiation damage to all samples. For each protein, the scavenging factors are: >100 for BLC, 10.57 for hAR, 20.45 for HEWL and 14.86 for SH3-SPC (Figure 21 and Table 3). The scattering profiles for all samples are plotted in Figure 21 (right panels) according to the number of frames below their critical doses. The signal-to-noise ratio is especially improved at high angles when 100 mM 5-methyl uridine is used (Figure 21) and thus the useful data range in the scattering profiles is wider for all proteins. The accessibility to the data range with useful information can be estimated through the number of available Shannon channels inside the experimental data[122,123]. All proteins in presence of 100 mM 5-methyl uridine have their available Shannon channels

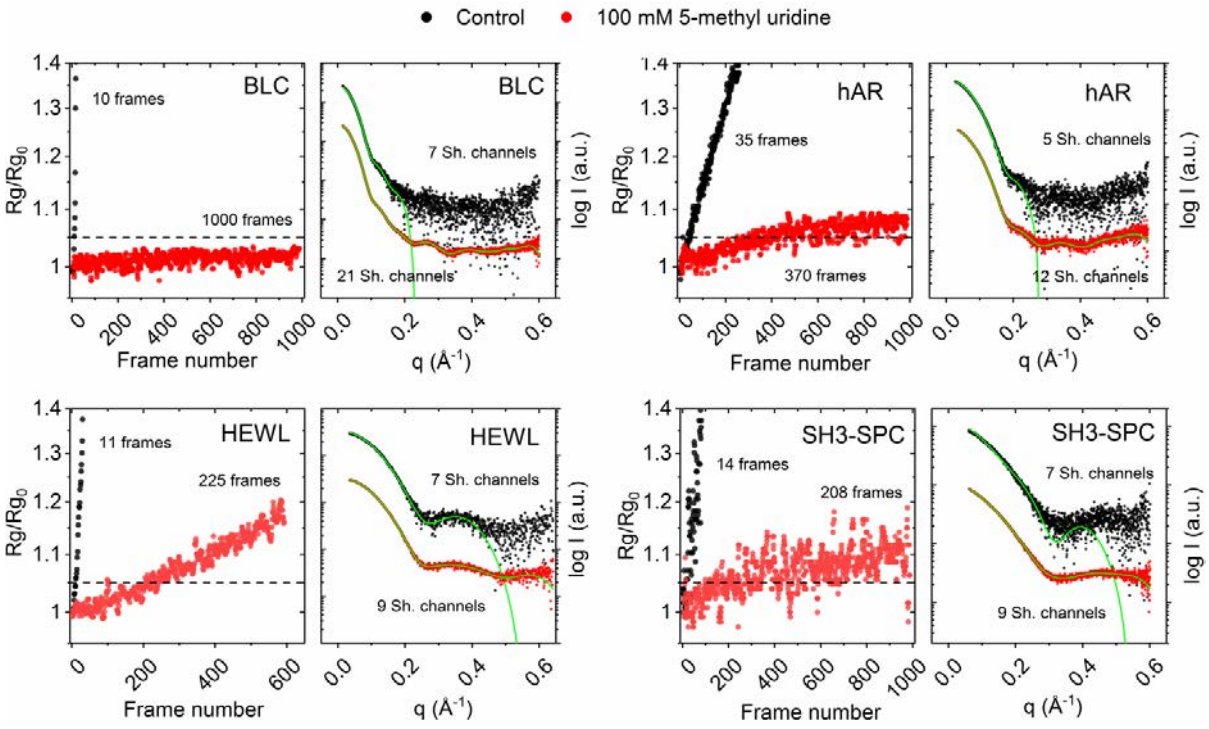

Figure 21 | *Radiation damage is mitigated and signal-to-noise ratio is improved for BLC, hAR, HEWL and SH3-SPC samples in presence of 100 mM of 5-methyl uridine. Left panels: normalized radius of gyration as a function of the number of collected frames. Right panels: experimental buffer subtracted scattering profiles in all the available angular range (black and red points) and its corresponding best Whittaker-Shannon interpolation polynomial (green lines). BLC sample conditions: 6.7 mg/ml of BLC in 50 mM potassium phosphate pH 7. hAR sample conditions: 7.0 mg/ml of hAR in 50 mM Tris pH 8 and 150 mM NaCl. SH3-SPC sample conditions: 10.0 mg/ml of SH3-SPC in 10 mM citric acid pH 3 and 150 mM sodium chloride.*

well determined (Figure 21). Conversely, only a few well determined Shannon channels can be achieved for all the tested proteins when it is no added any additive (Figure 21, right panels).

Table 3 | *The use of 100 mM 5-methyl uridine prevents to radiation damage and allows to obtain more information. The quantity of information inside a SAXS profiles is related with the number of well characterized Shannon Channels.*

Protein	BLC	hAR	HEWL	SH3-SPC
MW (kDa)	250	36	14	7
[protein] (mg/ml)	6.7	7.0	7.0	10.0
Scavenging factor	>100	10.57	20.45	14.86
$Sh.ch._{100\ mM\ 5\text{-}methyl\ uridine}$ / $Sh.ch._{Control}$	3.0	2.4	1.3	1.3

Nucleosides and nitrogenous bases for low protein concentrations

Based on the previous results, here is checked if the tested scavenging compounds can be instrumental for SAXS measurements at low protein concentrations. The measured and computed scattering profiles for HEWL samples (ranging from 0.5 to 7.0 mg/ml) in the presence of 100 mM 5-methyl uridine are plotted in Figure 22. All computed SAXS profiles in Figure 22 were calculated from their corresponding $P(r)$ functions (Supporting Figure 40). Each SAXS profile in Figure 22a consists in the average of all frames below $I(0)/I(0)_0 = 1.05$ (Supporting Figure 39 and Supporting Table 9). The chosen metric in in Figure 22 was $I(0)/I(0)_0$ because the Rg/Rg_0 metric was very noisy and inconsistent at 2.13 and 0.5 mg/ml with the previous results (Supporting Figure 39 and Table 2). The $P(r)$ functions can be calculated in all samples containing 100 mM 5-methyl uridine in the angular range $q \leq 0.4$ nm^{-1}, except at 0.5 mg/ml where the $P(r)$ function can be calculated only up to $q = 0.22$ nm^{-1} (Figure 22a and Supporting Figure 40). Instead, the computation of the $P(r)$ function for the control sample at 0.5 mg/ml is not possible and for the 2.13 mg/ml sample is only possible up to $q = 0.21$ nm^{-1} (Figure 22a and Supporting Figure 40). Ten independent DAMMIN models were computed for those samples where the calculation of the $P(r)$ functions was possible. For each sample, the model with the lower normalized spatial discrepancy (NSD) from the rest of the nine models is plotted and superposed to the HEWL crystallographic structure (PDB ID 5L9J[61]) in Figure 22b. NSD is a measure of quantitative similarity between sets of three-dimensional points. The worst DAMMIN model in Figure 22b is for the 2.13 mg/ml control sample. In all HEWL samples containing 100 mM 5-methyl uridine were possible to compute accurate DAMMIN models, even at 0.50 mg/ml (Figure 22b).

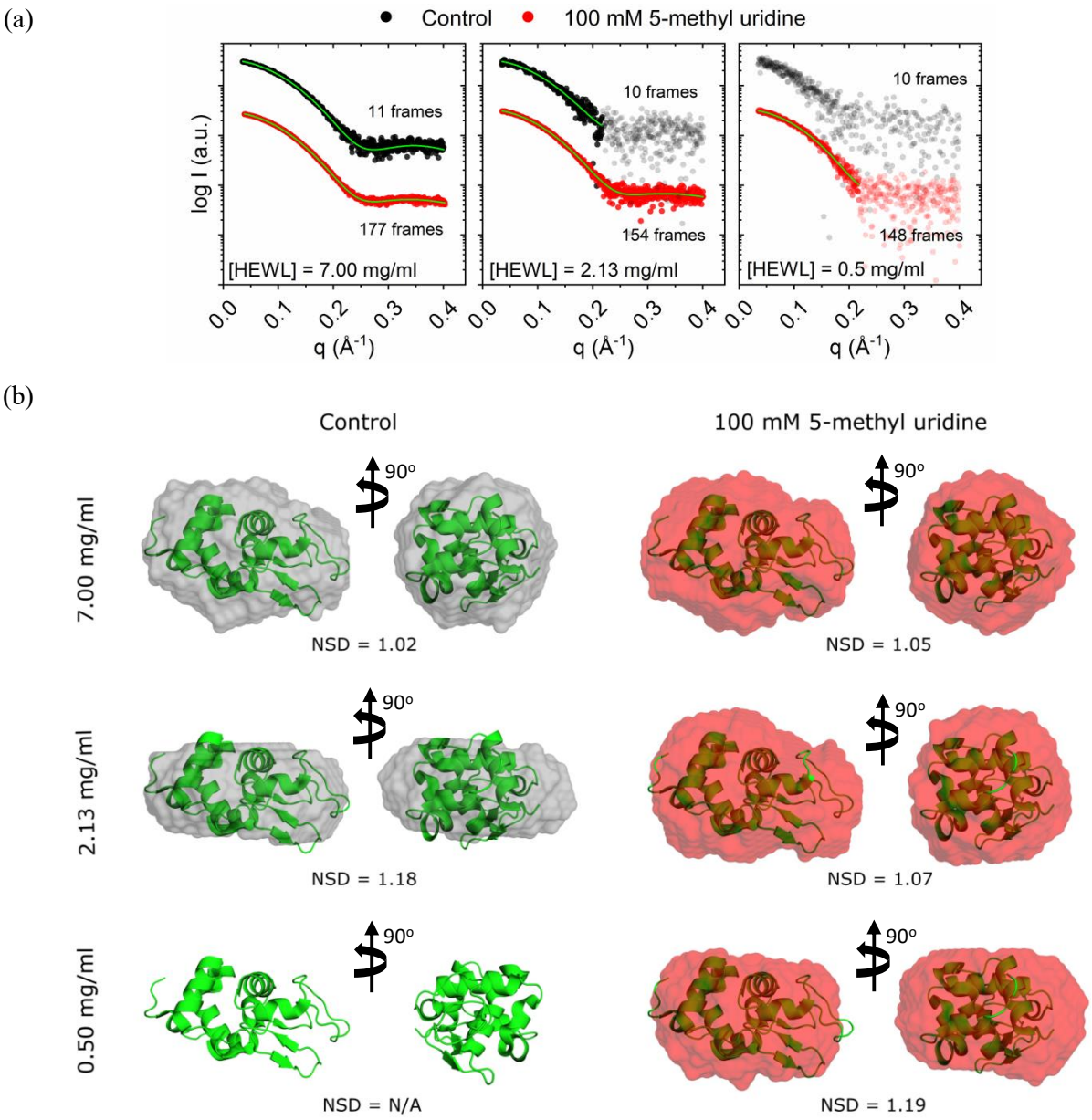

Figure 22 | *The presence of 100 mM 5-methyl uridine allows to collect useful data at low protein concentration. (a)Averaged SAXS profiles for HEWL samples at different protein concentrations (from 7.0 to 0.5 mg/ml). For each sample, the number of averaged frames meets the* $I(0)/I(0)_0 = 1.05$ *condition. In green: computed SAXS profiles from calculated* $P(r)$ *functions. (b) DAMMIN models superposed to the crystallography HEWL structure (PDB ID 5L9J[61]).*

Discussion

The scavenging effect of 5-methyl uridine, cytidine, cytosine and uridine was observed in both buffer- and protein-containing samples (Figure 18 and Figure 19, respectively). The use of these compounds to limit radiation damage on HEWL solutions is compared with that of glycerol, which is a well-known additive for that purpose in SAXS experiments. All metrics in Figure 19 show a consistent scavenging

effect for all the tested compounds as a function of their concentrations. The scavenging power from the tested nucleosides and from the nitrogenous base (from 25 to 100 mM) was higher than that from glycerol at 100 and 678 mM (Figure 19). All the tested compounds at 100 mM have scavenging factors around 4-fold higher than the corresponding for 678 mM glycerol. The electronic contrast for samples containing the highest tested concentration (100 mM) of 5-methyl uridine, cytidine, cytosine and uridine was higher than that for 678 mM glycerol (Figure 20).

The question about which is the more suitable definition of critical dose is controversial. Jeffries and coworkers[54] used an increase of 0.1 nm in the initial radius of gyration as a definition of critical dose; Kuwamoto and coworkers[52] choose, by visual inspection, the dose where Rg/Rg_0 and $I(0)/I(0)_0$ start to increase exponentially; Crosas and coworkers[61] defined another critical dosed as the threshold where Rg/Rg_0 reaches an increment of 10% and Brooks-Bartlett and coworkers defined the critical dose where three consecutive data frames were found to be dissimilar (by using the CorMap test[56]) to the first frame[124]. The critical doses defined in this work where inspired in those from Crosas and Brooks-Bartlett, although the idea to monitor $I(0)/I(0)_0$ in parallel to Rg/Rg_0 came from Kuwamoto. The critical dose defined by Jeffries was discarded since errors on the structural parameters calculated from a SAXS experiments are in the order of 0.1 nm. There are two reasons to be stricter than Crosas in the threshold for the increment in Rg/Rg_0 and $I(0)/I(0)_0$: i) there is a huge quantity of frames (around 150) between the 5% and 10% limits in Fig. 2 in those samples containing 100 mM 5-methyl uridine, cytidine, cytosine and uridine and ii) results for 5% as a threshold are closer to the CorMap test results than for 10%.

The scavenging properties against radiation damage of 5-methyl uridine, cytidine, cytosine and uridine can be expanded towards different samples conditions like buffer acidity, macromolecular weight and protein concentration (Figure 21 and Figure 22). Therefore, the use of these new scavengers for SAXS experiments can be instrumental for collecting data even at high angles or for samples with low protein concentrations or low macromolecular weight.

Capítol 3

Enhanced stability against radiation damage of lysozyme crystals grown in Fmoc-CF hydrogels

The results presented in this chapter are part of the recently submitted paper in Crystal Growth & Design:

Authors: Contreras-Montoya, R.[#] **Castellví, A.**[#] Guillermo Escolano-Casado, Judith Juanhuix, Mayte Conejero-Muriel, M. Modesto T. Lopez-Lopez, Juan M. Cuerva, Luis Álvarez de Cienfuegos and José A. Gavira.

[#]These authors contributed equally to this work

Introduction

Dipeptides derivatives have been the focus of an extensive research due to their capacity to self-assemble under different stimuli presenting remarkable physicochemical properties[125–129]. In particular, Fmoc (Fluorenylmethyloxicarbonyl)-peptide hydrogels have found applications in diverse fields such as, tissue engineering, biomineralization, catalysis and drug delivery[130]. Most of these applications have been possible thanks to the excellent macroscopic hydrogel properties and the modular chemical composition of the peptide fibers. Highlighted examples are the use of Fmoc-RGD in tissue engineering to promote cell adhesion and increase cell proliferation and survival[131] and the use of Fmoc-DOPA-DOPA (DOPA = 3,4-dihydroxy-phenylalanine) as a template to chelate and precipitate cationic silver into silver nanoparticles[132].

The application of dipeptide hydrogels as a media in protein crystallization[133,134] has allowed to J. A. Gavira and coworkers to study the interaction between the peptide fibers and proteins and to evaluate the physicochemical properties of the resulting composite crystals, since the gel fibers are occluded inside the protein crystals[135,136]. By using L and D-homochiral enantiomeric dipeptides they also studied the influence of the peptide-chirality in the polymorphism of the resulting crystals[133]. Later, they could observed that the peptide fibers were able to modify the thermal stability and dissolution rate of the crystals[134,137], even in the case of therapeutic proteins such as insulin[137]. Recently, Gavira and coworkers have shown that lysozyme crystals grown in Fmoc-FF (Fmoc-Phe-Phe-OH) hybrid hydrogels containing carbon nanotubes give rise to composite crystals that have novel properties such as electron conduction and thermally enhanced catalytic activity[138].

Based on these precedents, Gavira and coworkers wondered if novel composite crystals having a technological advantage over existing ones could be obtained using Fmoc-CF (Fmoc-Cys-Phe-OH) peptide hydrogels as a media for protein crystallization (Figure 23). At this respect, Gavira and coworkers focused their attention to the degradation that protein crystals grown in the presence of Fmoc-CF hydrogel suffer upon exposure to X-ray irradiation.

Here is reported the results concerning the radiation damage study of composite lysozyme crystals grown in the presence of Fmoc-CF hydrogels.

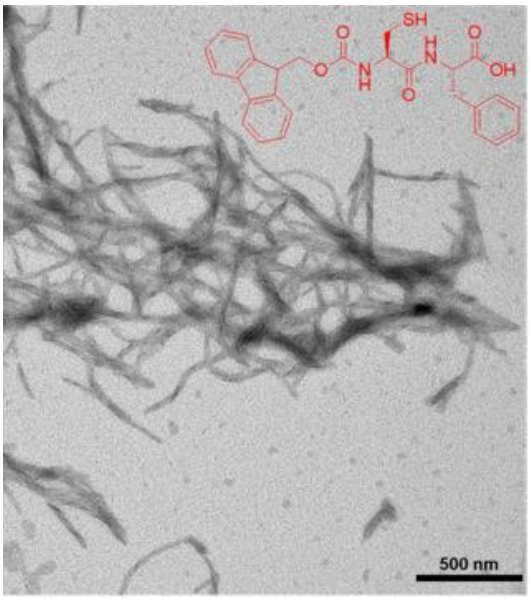

Figure 23 | *TEM image of Fmoc-CF xerogel and its chemical formula (in red).*

Materials and methods

Experimental

All materials were of analytical grade and used without further purification. Fmoc-Cys-Phe-OH was synthesized by solid phase protocol previously described[133].

Hydrogel preparation by solvent switch

Hydrogels Fmoc-CF were prepared in Eppendorf tubes by dissolving the peptide in DMSO followed by the addition of MiliQ water to reach a final volume of 100 µL[139]. The volume relationships DMSO:water were 15:85. The excess of DMSO in the formed hydrogels was then removed by the addition of 1 mL of MiliQ water on top of the hydrogels, changing the water every day.

Crystallization experiments

Lysozyme was purchased as lyophilized powder from Sigma (L6876). Lysozyme was dissolved and dialyzed against 50 mM Sodium Acetate pH 4.5 and the concentration determined spectrophotometrically at 280 nm prior setting the crystallization experiments and after filtration through a 0.45 µm pore size Millipore filter.

Counter-diffusion technique with two layers configuration (2L) of 50 µL each, was used to set-up crystallization experiments in Eppendorf tubes. Fmoc-CF, prepared at 1.0 & 2.0 wt% were used to set-up the crystallization experiments containing 80 mg/ml protein concentration and 6.0% NaCl, everything buffered with 50 mM sodium acetate at pH 4.5.

X-ray data collection and analysis

In order to clean the lysozyme crystals from the surrounding hydrogel (both agarose or Fmoc-CF), crystals were extracted from the corresponding crystallization experiment using a pipetman (200 µL), with the tip-end cut, and deposited over a drop containing the precipitant solution with the help of a LithoLoop (Molecular Dimensions Inc.). Lysozyme crystals of approximately 300 × 300 × 300 μm^3 were introduced into a polyimide capillary of 1.0 mm inner diameter (Goodfellow, IM307100) with the aid of a pipette. Sample dehydration was prevented by keeping a drop of reservoir solution near the crystal. The capillary was sealed with vacuum grease in both extremes and mounted on a SPINE magnetic cap compatible with the diffractometer.

Diffraction data sets were collected at the beamline BL13-XALOC using a Pilatus 6M photon-counting detector (DECTRIS, Baden, Switzerland). The beam profile had a Gaussian shape and was defocused to a FWHM dimension of 100 µm (h) × 53 µm (v) as measured by a Ce:YAG fluorescent screen at the sample position. The photon flux was attenuated to $3.45 \cdot 10^{10}$ ph/s (5% beam transmission) at the sample position as measured using a calibrated PIN Si diode. The sample to detector distance was set to 240 mm.

Lysozyme crystals grown in 0.5% (w/v) agarose and 1% and 2% (w/v) Fmoc-CF gels were measured maintaining the same irradiation conditions. For each crystal nine consecutive datasets were collected starting from the same initial angle. Each dataset of 90 images were collected with an angle increment per image of 1°. The average dose in the exposed region (AD-ER) was calculated with RADDOSE-3D[7]. All crystals were assumed to have the same cubic shape with side dimensions of 300 μm as measured by the on-beamline microscope. The amount of sulfur atoms in the solvent portion of lysozyme crystals was set to zero. The AD-ER was computed to be 0.03 MGy per dataset.

All datasets were indexed and integrated using XDS[93] and the values of the mean relative diffraction intensity (I_{Dn}/I_{D1}) extracted from XDSSTAT[94]. For each dataset, multiple observations of reflections were scaled and merged using AIMLESS[95] and the final structure factors generated with TRUNCATE (Supporting Table 10)[96]. For each crystal, structure solution and refinement were systematically performed with the corresponding first dataset (D1) in the resolution range from 40 to 1.35 Å (Supporting Table 11). Initial phases were found by molecular replacement with PHASER[140] and phase refinement were performed with phenix.refine[141] using anisotropic B-factors. All phases refinements were considered completed when R_{work} and R_{free} reached 0.14 and 0.17, respectively. Different Fourier maps between D1 and Dn datasets were calculated through the fast Fourier transform of $(F_{obs,Dn} - F_{obs,D1};\ \alpha_{D1})$, being $F_{obs,Dn}$ and $F_{obs,D1}$ the experimental structure factors from Dn and D1 datasets, respectively, and being α_{D1} the refined phases from the D1 dataset. Before the fast Fourier transform, $F_{obs,Dn}$ and $F_{obs,\ D1}$ were restrained in the same resolution range ($40 - 1.7$ Å) and scaled together in two different resolution bins (from 40 to 3.0 Å and from 3.0 to 1.7 Å) using SCALEIT[100]. The mean difference electron density in *Dn – D1* should be zero although local differences in electron densities are observed (positive and negative). Fast Fourier transforms were performed with FFT[142]. Maps and structures were visualized with PyMOL[143].

Results

The scavenging power of Fmoc-CF hydrogels was evaluated by analyzing the global diffracted intensity of lysozyme crystals grown in Fmoc-CF (at 1.0 wt% and 2.0 wt%) and agarose (at 0.5 wt%) hydrogels during nine consecutive irradiation cycles (named *D1* to *D9*), collected at room temperature. Lysozyme crystals grown in 0.5 wt% agarose were considered as controls for those experiments. Data collection statistics in the 40 – 1.7 Å resolution range are shown for agarose- and 2 wt% Fmoc-CF-containing crystals in the Supporting Table 10 for the first and 9th data sets.

The effects of X-ray irradiation were monitored at specific and local scale. To estimate the global damage (I_{Dn}/I_{D1}) it is monitored the decay of the total diffracted intensity of each cycle (I_{Dn}) by comparing it with the collected intensity of the first data set (I_{D1}). Lysozyme crystals grown in the presence of 1 and 2 wt% of Fmoc-CF did not show signs of protection against global damage (Figure 24a). However, we observed a marginal improvement of the crystal quality parameters (R_{mean} and $\langle I/\sigma \rangle$) for lysozyme crystals grown in the presence of 2 wt% Fmoc-CF (Supporting Table 10).

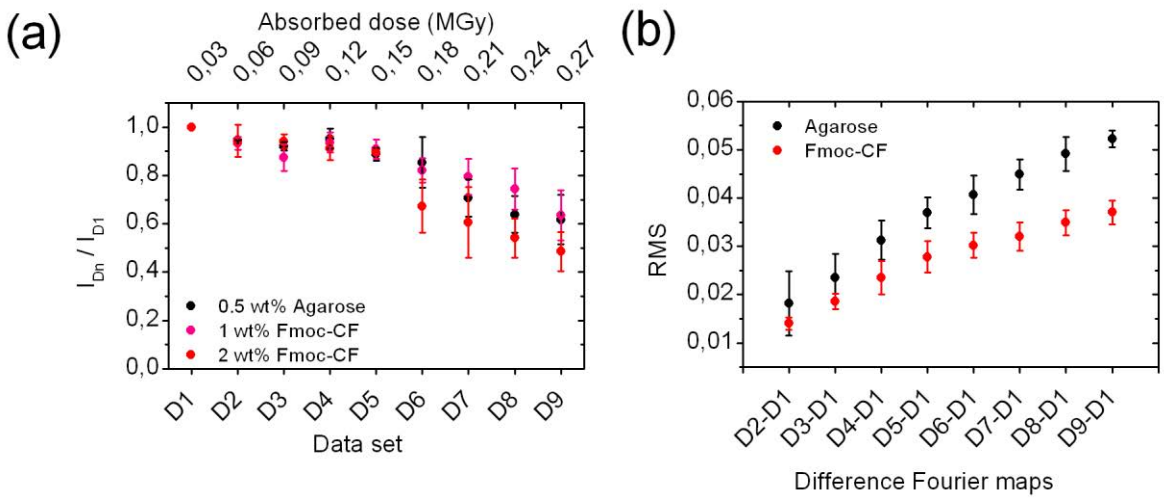

Figure 24 | *Global and specific damage on lysozyme crystals in the presence of agarose and Fmoc-CF hydrogels. (a) I_{Dn}/I_{D1} as a function of absorbed dose/dataset in lysozyme crystals in the presence of agarose and Fmoc-CF gels. Each point was calculated by triplicate. (b) RMS values as a function of Dn – D1 maps. Each point was calculated by triplicate.*

Local radiation damage in the crystal was monitored through the inspection of the difference electron density (Fourier) maps of the *Dn* and *D1* data sets calculated as *(Dn – D1)* (Figure 24b). The root mean square (RMS) value for the mean difference electron density in *(Dn – D1)* is an indicator of the local alteration induced by radiation damage between freshly (*D1*) and incremental damage (*Dn*) data sets. Local damage is preserved for lysozyme crystals grown in 2 wt% Fmoc-CF as it is shown by the RMS metric (Figure 24b). Although, local radiation damage is better observed in the most sensitive groups (disulfide and methionine) very reactive to the species generated during X-ray exposure. *D9 – D1* maps contoured at $-0.15\ e/\text{Å}^3$ over all disulfide bonds and methionines are shown in Figure 25 and Supporting Figure 41. Those maps showed significant specific protection of lysozyme crystals obtained in the presence of 2 wt% Fmoc-CF hydrogel (Figure 25 and Supporting Figure 41). When analyzed one by one the target groups specific protection was detected in Cys64-Cys80, Cys76-Cys94, Met12 and Met105 of crystals grown in 2 wt% Fmoc-CF, while for crystals grown in agarose, S-S and S-C bonds are broken in some degree due to the radiation effect. This damage was negligible in the case of Cys6-Cys126 (Figure 25 and Supporting Figure 41) and not detectable at 0.15 e/Å^3 contour level in the case of Cys30-Cys115 bound (Figure 25 and Supporting Figure 41).

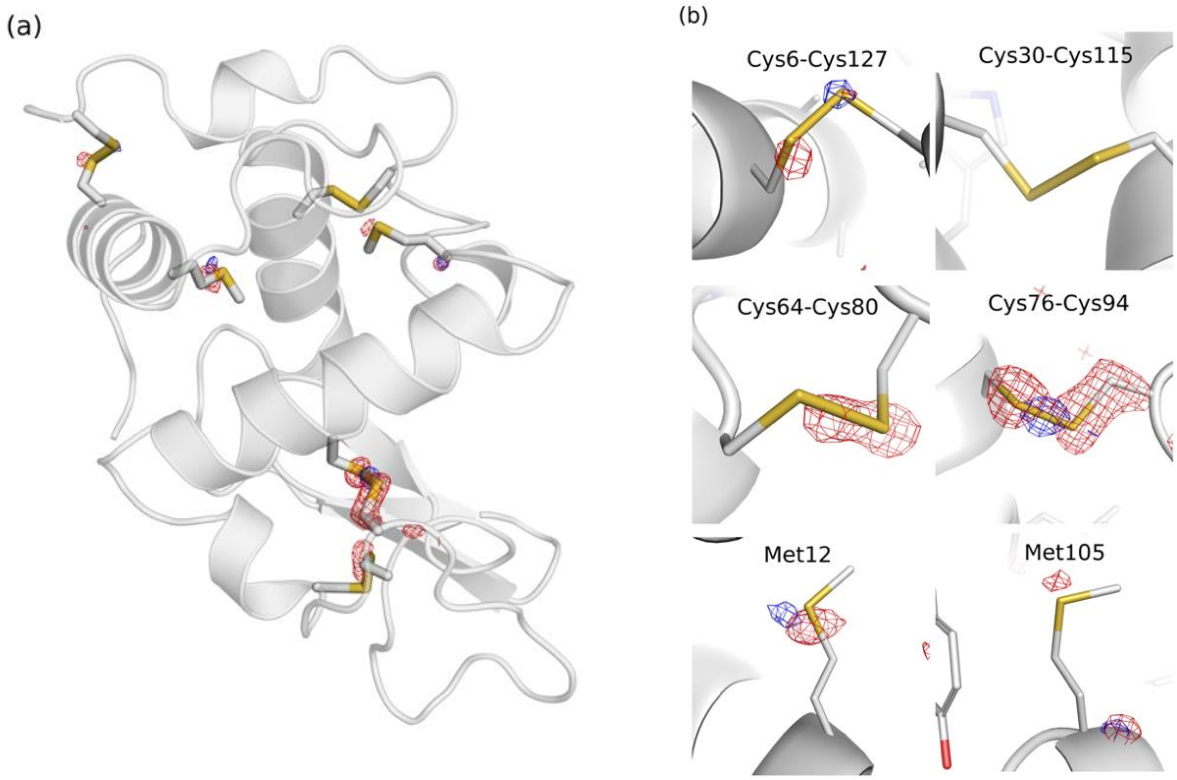

Figure 25 | *Fmoc-CF hydrogel protects disulfide bonds and methionines against radiation damage in lysozyme crystals. (a) A ribbon representation of the lysozyme structure showing the most sensitive groups to radiation damage, cysteine and methionines. The D9 – D1 maps (contoured at -0.15 e/Å^3) for agarose and Fmoc-CF are shown in red and blue respectively. (b) Shows the detail of the four cysteine bridges and the two methionines followed in this study (extended data in Supporting Figure 41). Note that the difference electron density are obtained from the RMS × σ: RMS (Agarose, D9-D1) = 0.051 with σ(Agarose, D9-D1) = -2.95 and RMS (Fmoc-CF, D9-D1) = 0.040 with σ(Fmoc-CF, D9-D1) = -3.76 (Supporting Figure 41). Data plotted for Aga_1 and Fmoc-CF crystals (Supporting Table 10 and Supporting Figure 41).*

Discussion

As shown in Figure 24a the presence of Fmoc-CF hydrogel does not prevent to lysozyme crystals to be damaged at global scale. This result is in agreement with those results obtained from other thiol-containing compounds tested in lysozyme crystals at room temperature[38]. However, from Figure 24b it is clear that the presence of 2 wt% Fmoc-CF in lysozyme crystals delays the local damage as observed by the smaller increment of RMS as a function of the Dn – D1. When compare to the reference, the RMS ratio between Fmoc-CF and agarose is maximum in the D9 – D1 and it is equal to 0.709 (Figure 24b). As far as I know, nobody had used until now the RMS metric for monitoring RD. Therefore, lysozyme crystals grown in Fmoc-CF hydrogels, unlike those grown in agarose, give rise to composite crystals that have an enhanced resistance against radiation damage. Fmoc-CF dipeptide shows a clear protection of the most sensitive groups (disulfide bonds and methionines) of the protein. The protection mediated by cysteine is exerted

only in its gel state since cysteine in solution has an adverse effect. Probably the reactive thiols groups of cysteine being locked within the rigid peptide fibers minimize cross-reactions with the protein. Once located inside the protein crystal the long peptide fibers are able to protect the protein against radiation damage.

It has to be noted that the protocol for obtaining the *Dn – D1* maps is far from the protocols usually used in the field. An effect from global damage is the degradation of the diffraction patterns as a function of the irradiation time. This effect is especially predominant for the highest resolution shells and it has to be corrected when the scaling step between datasets is performed. If the whole range of resolution is used for scale, the result will be a wrong scaling that will be subsequently translated as artefacts in the computed *Dn – D1* maps. If the progression of global damage is not severe those artifacts can be negligible, but if global damage is strong (as reached easily with experiments at room temperature) the results will be unintelligible. This point may give an answer to the lack of results in the literature about the use of difference Fourier maps for specific damage at room temperature. In order avoid artifacts, before to perform a different Fourier map, the $F_{obs,Dn}$ and $F_{obs,\ D1}$ parameters in this work were restrained in the same resolution range ($40 - 1.7$ Å) and scaled together in two different resolution bins (from 40 to 3.0 Å and from 3.0 to 1.7 Å (Figure 26). The result of this protocol is the generation of reliable different Fourier maps free of artifacts (Figure 26). This protocol, applied to agarose and Fmoc-CF samples, lead to the same results (Figure 27 and Supporting Figure 41).

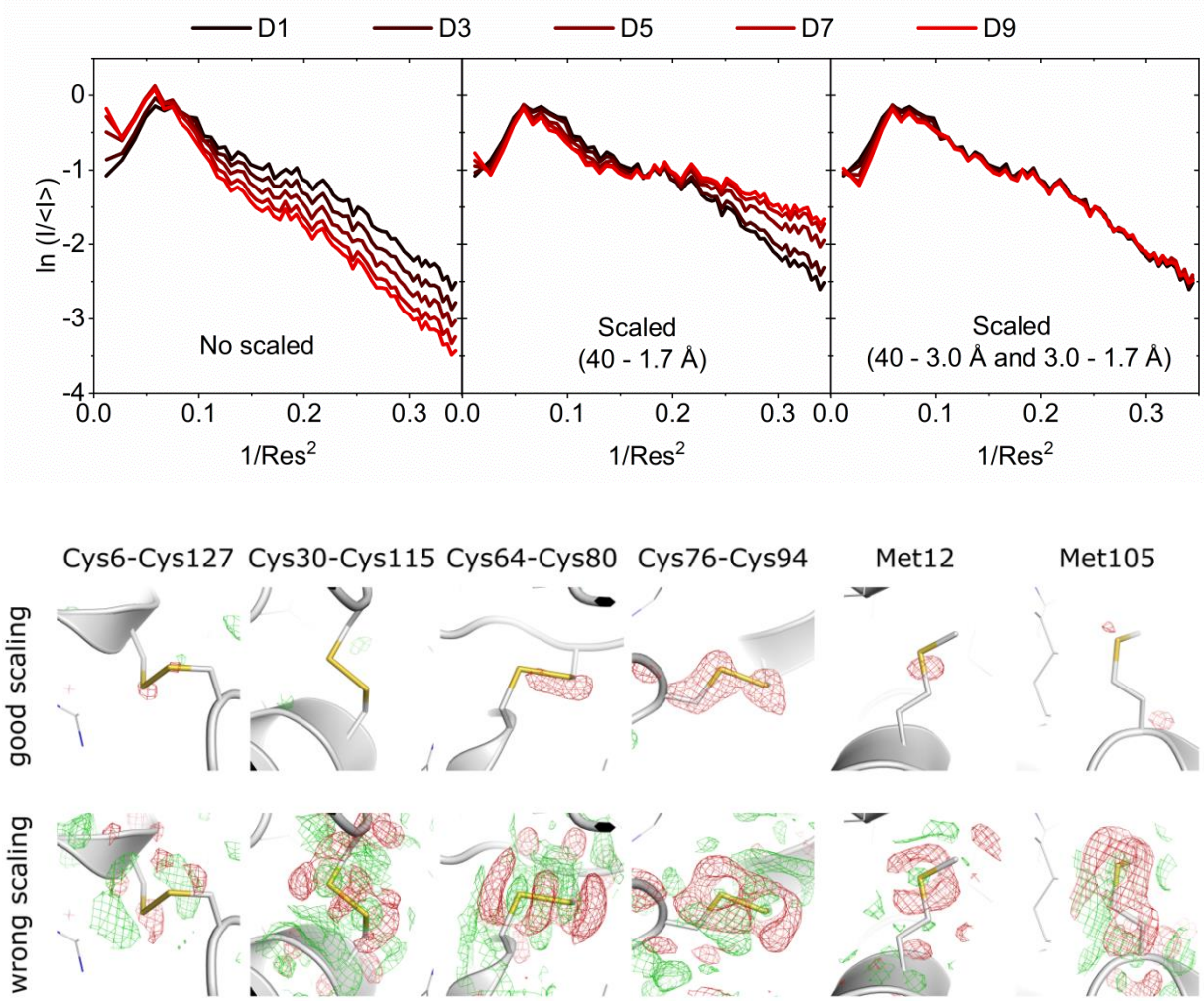

Figure 26 | *The result of considering the entire range of resolution is a wrong scaling between datasets that is subsequently translated as artifacts in the computed* $Dn - D1$ *maps. Top: Non-scaled datasets (left), scaled datasets in the* $40 - 1.7$ *Å resolution range (middle) and scaled datasets in two different resolution ranges (*$40 - 3.0$ *Å and* $3.0 - 1.7$ *Å) (right). Down: D9-D1 maps over all disulfide bonds and methionines using the right scaling protocol (upper row) and using the wrong scaling protocol (bottom row) for the Aga_1 crystal. All maps are contoured at 0.15 e/A*^{3} *(*$RMS_{GoogScaling} = 0.0508$, $RMS_{WrongScaling} = 0.07303$*). Difference electron density = RMS* $\times \sigma$*. Positive and negative difference electron density are plotted in green and red, respectively.*

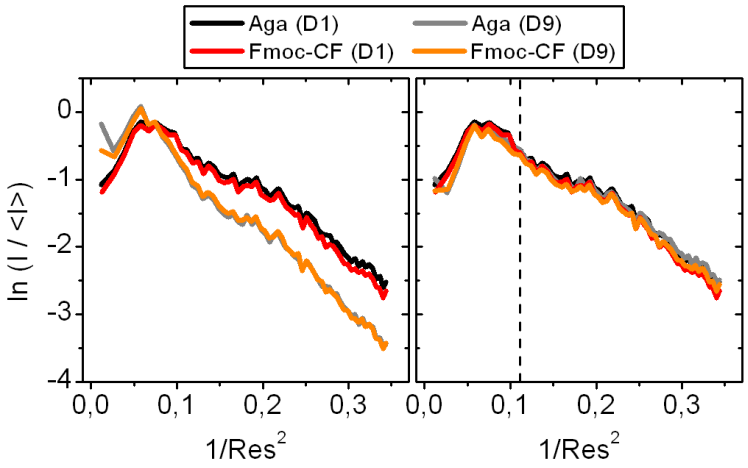

Figure 27 | Global and specific damage on lysozyme crystals in presence of agarose and Fmoc-CF hydrogels. Wilson plots from D1 and D9 datasets for lysozyme crystals in presence of agarose and Fmoc-CF gels. Left: non-scaled datasets. Right: scaled datasets in two different resolution ranges (40.0 – 3.0 Å and 3.0 – 1.7 Å). Dashed line represents Res = 3.0 Å. Data extracted from Aga_1 and Fmoc–CF_1 crystals (see Supporting Table 10).

Capítol 4

Efficacy of aldose reductase inhibitors is affected by oxidative stress induced under X-ray irradiation

The results presented in this chapter are published in:

Scientific Reports. (2019). **9**:3177. DOI: 10.1038/s41598-019-39722-0

Authors: **Albert Castellví**,[§] Isidro Crespo,[§] Eva Crosas, Ana Cámara-Artigas, José A. Gavira, Miguel A. G. Aranda, Xavier Parés, Jaume Farrés and Judith Juanhuix.

[§]These authors contributed equally to this work.

Introduction

The increase in the flux of the polyol pathway is the main mechanism by which hyperglycemia leads to diabetic complications, such as microvascular and macrovascular damage. This pathway is followed by only 3% of the cytosolic glucose in physiological conditions but increases to more than 30% under hyperglycemic conditions[144,145]. The key step in this pathway is the reduction of glucose to sorbitol catalyzed by aldose reductase (hAR, AKR1B1), a member of the NAD(P)H-dependent aldo-keto reductase superfamily[144–149]. One of the first cellular deleterious effects is NADPH depletion, reducing its availability for the regeneration of the powerful antioxidant glutathione (GSH) and weakening intracellular antioxidant defenses[145,149–151] (Figure 28). Moreover, in the second step of the polyol pathway, sorbitol is metabolized by sorbitol dehydrogenase (SDH) to fructose at the expense of producing additional NADH, which potentially increases the reactive oxygen species (ROS) via NADH oxidase (NOX) and electron leakage in the electron transport chain[151,152] (Figure 28). The inhibition of hAR would therefore block the polyol pathway, counteracting significantly the unbalanced conditions caused by intracellular oxidative stress typical of diabetes.

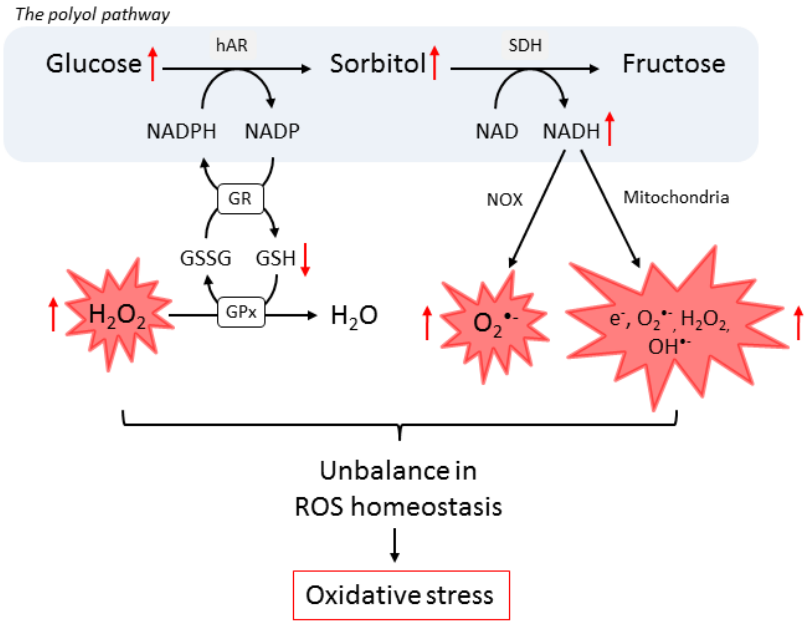

Figure 28 | *The polyol pathway. The 30% of glucose is shunted to the polyol pathway under hyperglycemia conditions, where hAR reduces glucose into sorbitol at the expense of NADPH. Since NADPH is essential for generation of GSH from GSSG, the depletion of NADPH by the hAR pathway may impair intracellular antioxidant defense. Sorbitol is then converted to fructose by SDH with the production of NADH, potentially leading to increased ROS via NOX and electron leakage in the electron transport chain.GR: glutathione reductase. GPx: glutathione peroxidase.*

Aldose reductase inhibitors (ARIs) have been indeed the focus of research for over 40 years since the discovery of the involvement of hAR in diabetic processes[145]. Unfortunately, the attempts to find an effective drug targeting hAR under diabetic conditions have been unsuccessful so far. Although several

inhibitors have been reported to effectively block the hAR activity *in vitro* using purified protein[150], their potency is severely reduced when tested in clinical trials. Early on, this effect was hypothesized to be related to the generation, in significant amounts, of an activated form of hAR under oxidative stress conditions, which differs from the native form in its kinetic constants and a marked reduction to ARIs sensitivity[153–155]. Remarkably, it has been shown that hAR can be activated also *in vitro* by mutagenesis of Cys298 residue (C298S[156,157], C298A[157,158]), which has been identified as the main target for various oxidative modifications[159–162], or by the incubation of the enzyme with chemical compounds[163]. The study of ARIs therefore requires the use of this hAR form present under intracellular oxidative stress conditions found in diabetes, which differs from the native form expressed in physiological conditions or prepared by recombinant techniques.

The oxidative stress causing metabolic abnormalities in cells exposed to hyperglycemia is mainly produced by the accumulation of intracellular free electrons and reactive oxygen species (ROS), notably $O2^{\bullet-}$, H_2O_2 and $OH^{\bullet}$, among others[164]. Cellular oxidative stress cannot be reproduced in vitro due to the complexity and diversity of factors influencing this condition. In consequence, *in vitro* studies under oxidative stress conditions utilize indirect methods to produce the same reactive species as those produced *in vivo*, such as the addition of chemical compounds. Another common method, which bypasses the potential bias in the result interpretation that the use of a particular chemical compound might introduce, is to employ electrons or ionizing radiation to create radical species in protein solutions[69,165–170]. As documented extensively in the literature, the radical species induced by irradiation are the same than those present under oxidative stress conditions[164,171]. The use of X-rays of a wavelength of ~1 Å (12.4 keV) is particularly convenient as the energy is deposited evenly over a thickness in the millimeter range or less in protein solutions or crystals.

Here we employ synchrotron X-ray irradiation at that wavelength to report a modification of hAR which reproduces the behavior of the activated form generated under diabetic oxidative stress conditions. This modification has been characterized by enzymatic assays after exposition of hAR in solution under different irradiation doses, by monitoring the progressive structural changes of hAR crystals as irradiation dose increases and by characterizing the structural changes in solution using mass spectrometry. The activity of the *in-vitro* potent ARIs Zenarestat[172], JF0048[173], Epalrestat[174] and Tolrestat[175] was also checked at different irradiation doses. A mechanism for the activation of hAR under oxidative stress conditions is proposed and some suggestions for the structure-based drug design targeting hAR are provided.

Materials and methods

Protein purification and crystallization

The hAR cDNA obtained from Alexandra Cousido-Siah and Alberto Podjarny (IGBMC-CNRS-Univ. Strasbourg) was cloned into the pET-15b expression vector. The expression of the His6-tagged protein in *Escherichia coli* strain BL21 (DE3) pLysS was induced at 20ºC by 1 mM IPTG at OD600 0.8-1 and cells were incubated for 16h in a 2 L culture. Then cells were disrupted by sonication and centrifuged at 4ºC in 20mM Tris-HCl pH 8.0, 250mM NaCl, 5mM imidazole buffer. The pellet was discarded and the supernatant was loaded in a nickel ion affinity chromatography column. The hAR was eluted in an imidazole gradient (5-250 mM). Then, thrombin cleavage of the His-tag was carried out overnight at 277 K. The buffer of the cleaved protein was changed to 50 mM ammonium citrate pH 5.0. The hAR crystals were grown by the hanging drop vapor diffusion method. 10 µL of protein at 30 mg/mL with a NADPH:protein ratio of 2:1, was mixed with 10 µL of 50 mM ammonium citrate pH 5.0, 10% (w/v) polyethylene glycol (PEG) 6000 and 1 mM DTT. The solution was equilibrated at 4ºC for a week against a 500 µL reservoir, consisting of 20% PEG 6000 and 120 mM ammonium citrate, pH 5.0. After drop equilibration, nucleation was induced by seeding at room temperature. Crystals grew until its maximum size (around 0.8 mm long) in three days and finally they were transferred into a cryoprotecting solution consisting of 85 mM ammonium citrate pH 5.0 and 40% PEG 6000 prior to be loop-mounted and stored in liquid nitrogen.

Protein irradiation in solution for the enzymatic assays

For a given sample, 3 µL at 2.3 mg/mL in 20 mM Tris-HCl, 250 mM NaCl pH 8.0 were introduced inside a polyimide cylindrical capillary of 1 mm internal diameter and 0.025 mm wall thickness. The ends were sealed with vacuum grease to prevent liquid evaporation. The capillary was placed in a magnetic base compatible with the BL13-XALOC goniometer (Supporting Figure 46). Homogeneous irradiation was ensured by scanning the whole sample volume at uniform speed using a top-hat rectangular-shape X-ray beam of 200×180 μm^2 (Supporting Figure 46). The photon flux at sample was measured prior to each experiment by a calibrated Si PIN diode. The photon energy was set to 12.661 keV (0.979 Å).

Enzymatic assays

The hAR activity was determined with a Varian Cary 400 (UV/VIS) spectrophotometer at 25ºC by monitoring at 340 nm the decrease of NADPH in 0.6 mL of 0.1 M sodium phosphate buffer pH 7.4, containing 2 µL of irradiated or native enzyme, 0.2 mM NADPH and 10 µM - 30 mM D,L-glyceraldehyde. For inhibition assays, activity was measured under the same conditions, in the presence of 6mM D,L-glyceraldehyde. Concentrated stocks of inhibitors were prepared in DMSO and diluted in the reaction mixture to reach a final compound concentration close to the IC_{50} value in a final DMSO concentration of 1% (v/v). Control activity was performed in the presence of 1% (v/v) DMSO (Supporting Figure 42). All

the experiments were performed at least in triplicate, using for each activity an independently irradiated protein sample.

From the slope of the absorbance vs time graph, the variation of absorbance per second was obtained, which was then converted to specific activity using NADPH molar extinction coefficient (ε = 6,220 $M^{-1}cm^{-1}$), enzyme concentration and sample volume applied and protein molecular weight (35.9kDa). Specific activities obtained for native protein at substrate concentrations ranging from 10 µM to 30 mM were fitted to the substrate inhibition equation:

$$V = \frac{V_{max} * [S]}{K_M + [S] * \left(1 + \frac{[S]}{Ki}\right)}$$

In the case of 1kGy irradiated protein, as no significant substrate inhibition was observed in the tested concentrations, data was fitted to the Michaelis-Menten equation:

$$V = \frac{V_{max} * [S]}{K_M + [S]}$$

MX data collection

Diffraction data collections at 100 K were performed in the BL13-XALOC beamline at the ALBA synchrotron using a Pilatus 6M photon-counting detector (DECTRIS, Baden, Switzerland). The beam was set at 13.750 keV photon energy (λ = 0.9017 Å) and the sample-detector distance was adjusted to collect the datasets at a resolution of 0.90 Å. The attenuated photon flux during data collections was 1.2×10^{11} photons/s as measured using a calibrated Si PIN diode at the sample position. The beam profile had a top-hat circular shape and was defocused to 190 µm in diameter as measured by a Ce:YAG fluorescent screen at the sample position (Supporting Figure 47). Twenty complete data sets (D1-D20) of 800 images each were collected with an angle increment of 0.25 deg and 0.1 s exposure time per image. The crystals were irradiated between datasets using a beam with a photon flux of 6.3×10^{11} photons/s to speed-up radiation damage effects. The total oscillation angle was identical for all burns and data collections.

MX data processing and structure refinement

All twenty datasets collected in the MX experiments were indexed and integrated using XDS[176] in $P2_1$ space and cell parameters similar to those previously reported. The datasets were scaled and the structure factors generated using AIMLESS[95] and TRUNCATE[96], respectively. The resolution cutoff for each dataset was chosen so that R_{merge} was around 30% in the last resolution shell. Following this criterion, the I/σ in the last resolution shell ranged between 3.6 and 4.7 for all the datasets (Supporting Table 12). The initial phases to solve the structure of the D1 dataset were calculated from PDB entry 2J8T[177] after removal of water molecules and alternative conformations with Phaser-MR[140]. To reduce the model bias, all the atom coordinates from the initial model were randomly shifted by 0.15 Å using PDBSET and the Cys298-Sγ and Cys298-Cβ atoms were removed. The initial phases for D2-D20 structures were extracted in the

course of a refinement process based on the previously solved structure after the removal of water molecules with a B-factor > 35 Å^2. All the structure refinements were carried out using SHELXL[178]. The examination of the density maps and the manual rebuilding of the model were done using Coot[179]. The refined parameters included atomic coordinates, atomic displacement parameters (ADP), and atomic occupancy. The bond length standard uncertainties were computed by inversion of the full normal matrix with SHELXL. No riding hydrogen atoms were included in the model. The difference Fourier maps were built using reflections between 50 Å and 1.2 Å resolution and were Wilson scaled together via SCALEIT[100]. The difference Fourier maps ($F_{obs,n}$ - $F_{obs,1}$, $\alpha_{calc,1}$) were calculated between each dataset n and the initial dataset using the phases of the fresh, not previously irradiated dataset, $\alpha_{calc,1}$. The complete data collection and refinement statistics are listed in Supporting Table 12 and Supporting Table 13, respectively. The crystal structures were deposited at the Protein Data Bank with PDB IDs 6F7R, 6F81, 6F82, 6F84 and 6F8O for datasets D1, D5, D10, D15 and D20, respectively.

MX structure alignment

The alignment between the crystallographic structures were carried out by LSQKAB using the method described by Kabsch[180] between residues Ser2 and Phe311. The root mean square deviation (RMSD) of the C298 residue and the whole structure excluding the disordered terminal residues (Ser2 to Phe311) were calculated for the Cα, main chain, side chain and all atoms (Supporting Table 14).

SAXS data collection

SAXS data from B21 Beamline (Diamond Light Source, Didcot, United Kingdom) was obtained using a Pilatus 2M photon-counting detector (DECTRIS, Baden, Switzerland) and a camera length of 4.014 m. The beam at the sample position was 4 mm (horizontal) × 0.96 mm (vertical) and had an incident flux of 8.5×10^{10} photons/s at 12.4 keV (λ = 0.999 Å). The hAR samples were measured in 100 mM sodium phosphate buffer, pH 7.4, at a concentration of 2.7 mg/ml. For the samples containing uridine, a 10X stock solution of the additive was prepared in the same buffer and ten-fold diluted to a final concentration of 10 mM prior to the measurements. All samples were analyzed in a cylindrical quartz capillary of 1.6 mm internal diameter with a wall thickness of 0.1 mm, held at 283 K under vacuum. Multiple frames of 10 s exposure time were recorded. The data were collected by using the BioSAXS sample changer robot[181]. The experiments were performed in static mode and without beam attenuation to speed-up radiation damage on the sample. The SAXS experiments with samples containing uridine were performed under the same conditions.

SAXS data analysis

Radius of gyration (R_g) was determined with the Guinier approximation[182] by using the PRIMUS software[183] included in the ATSAS package[114]. Radiation damage was monitored by the normalized radius of gyration calculation, R_g/R_{g0}, where R_g is the radius of gyration at a given dose and R_{g0} is that obtained

in the first data frame. An increase of more than 10% in the normalized radius of gyration is considered indicative of significant global structural radiation damage.

Dose calculations

The dose absorbed by the samples in the enzymatic and SAXS experiments was calculated by using the Lambert's Law:

$$D = \frac{F_{in} \ < Trans >_{container,1} \ E \ t \ < Abs >_{sample}}{m}$$

where F_{in} is the incoming photon flux, E is the photon energy, t is the accumulated exposure time, m is the mass of the irradiated sample, $<Trans>_{container,1}$ is the average transmission coefficient for one side of the container and $<Abs>_{sample}$ is the average absorption coefficient for the irradiated sample.

For these experiments $<Trans>_{container,1}$ was calculated following:

$$< Trans >_{container,1} = \frac{1}{2R_{ext}} \int_{-R_{ext}}^{R_{ext}} \exp(-\mu\rho d/2) dx$$

where μ is the attenuation coefficient of the container at the used photon energy, ρ is the density of the container, R_{ext} is the external radius and d is the beam path length through the container. $<Trans>_{container,1}$ was calculated to be 0.992 for the polyimide container (μ = 1.494 cm^2/g and ρ = 1.425 g/cm^3) and 0.690 for the quartz container (μ = 9.804 cm^2/g and ρ = 2.648 g/cm^3) (Supporting Figure 48).

In the case of enzymatic experiments $<Abs>_{sample}$ was calculated from:

$$< Abs >_{sample} = 1 - \frac{1}{< Trans >^2_{container,1}} \frac{1}{2R_{in}} \int_{-R_{in}}^{R_{in}} \frac{F_{out}(x)}{F_{in}} dx$$

where F_{out} is the output photon flux, $<Trans>_{container,1}$ is taken from the polyimide container and R_{in} is the internal radius of the container. F_{in} and $F_{out}(x)$ were measured experimentally by scanning the capillary the x direction with a calibrated Si PIN diode (Supporting Figure 49). For enzymatic experiments $<Abs>_{sample}$ was calculated to be 0.256.

Since the protein concentration for the SAXS experiments was very low (~75 μM), the protein solution was approximated to be only water (μ = 2.673 cm^2/g and ρ = 1 g/cm^3). With this assumption, $<Abs>_{sample}$ can be calculated through:

$$< Abs >_{sample} \approx 1 - \frac{1}{2R_{int}} \int_{-R_{int}}^{R_{int}} \exp(-\mu\rho D) dx$$

where D is the beam path length through the sample. For SAXS experiments $<Abs>_{sample}$ was calculated to be 0.282. All the attenuation lengths μ and density ρ values were extracted from the XCOM Photon Cross

Sections Database (https://physics.nist.gov/cgi-bin/Xcom/xcom2). The average dose in the exposed region (AD-ER) for the MX experiments was calculated with RADDOSE-3D[184].

Inhibitor compounds

Zenarestat (3-(4-bromo-2-fluorobenzoyl)-7-chloro-3,4-dihydro-2,4-dioxo-1(2H)-quinazolineacetic acid) was generously provided by A. Podjarny. JF0048 (2-(3-(4-chloro-3-nitrobenzyl)-2,4-dioxo-3,4-dihydropyrimidin-1(2H)-yl)acetic acid) was a gift from A.R. de Lera (Univ. Vigo), and was synthesized as described previously[173]. Tolrestat was a kind gift of Prof. T.G. Flynn (Queen's University, Kingston, Canada). Epalrestat was purchased from Sigma-Aldrich (reference SML0527).

Liquid chromatography– tandem mass spectrometry (LC-MS/MS)

Proteins were manually digested with trypsin (Sequencing grade modified, Promega). Briefly, proteins were reduced by treatment with a solution of 20 mM DTT in 50 mM NH4HCO3 for 30 min at 56ºC, and then alkylated by treatment with a 50 mM solution of iodine acetamide for 30 min at room temperature. Proteins were digested overnight, at 37ºC with 100 ng of trypsin. Tryptic peptides were cleaned up with C18 homemade stage tips. Eluted peptides were dried in a vacuum centrifuge. The dried-down peptide mixtures were re-suspended in 1% formic acid and analyzed in a nanoAcquity liquid chromatographer (Waters) coupled to a LTQ-Orbitrap Velos (Thermo Scientific) mass spectrometer. Peptides were trapped on a Symmetry C18TM trap column (5 µm particle size, 180 µm×20 mm; Waters), and were separated using a C18 reverse phase capillary column (ACQUITY UPLC M-Class Peptide BEH column; 130 Å, 1.7 µm, 75 µm×250 µm, Waters). The gradient used for the elution of the peptides was 1 to 40 % in 30 min, followed by a gradient from 40 to 60% in 5 min (A: 0.1% formic acid; B: 100% acetonitrile, 0.1% formic acid), with a 250 nL/min flow rate. Eluted peptides were subjected to electrospray ionization in an emitter needle (PicoTipTM, New Objective) with an applied voltage of 2000 V. For each irradiated, peptide masses (m/z 300-1700) were analyzed in data dependent mode where a full Scan MS was acquired in the Orbitrap instrument with a resolution of 60,000 FWHM at m/z 400. Up to the 15 most abundant peptides (having a minimum intensity of 500 counts) were selected from each MS scan and then fragmented in the linear ion trap using CID (38% normalized collision energy) with helium as the collision gas. The scan time settings were: Full MS: 250 ms (1 microscan) and MSn: 120 ms. The scan time settings were 250 ms (2 microscan) for full MS, and 300 ms for MSn. The raw data files were collected and generated using Thermo Xcalibur (v.2.2). All the steps in the LC-MS/MS measurements were performed at the Plataforma de Proteòmica of the Parc Científic de Barcelona.

Analysis of non-thiolated cysteines

The reduction state of cysteines was assayed following the Pierce procedure for quantitating sulfhydryl groups based on molar absorptivity. Briefly, the reduced cysteines are detected by their reaction with 5,5'-dithiobis-(2-nitrobenzoic acid) (DTNB)[185], which gives a product with a maximum absorbance at 412 nm. The reaction buffer used in the analysis of exposed cysteines consisted of 0.1 M sodium phosphate, 1 mM

EDTA, pH 8.0. The reaction buffer used in the analysis of total cysteines added 8 M urea. The DTNB solution was prepared by mixing 4 mg of the reagent with 1 mL of reaction buffer (with or without urea). Two µL of the irradiated or native protein were mixed with 2.5 µL of reagent preparation and 7.5 µL of reaction buffer, giving a final reaction volume of 10 µL. The reaction was left at room temperature until the measure was stable (from 15 min to 5 h). Experiments were carried out in triplicate for each dose and for the buffer with or without urea, and used native protein as a control for each dose measure. Absorbance at 412 nm was monitored with a Nanodrop 2000 (Thermo Scientific).

The number of reduced cysteines per protein molecule was calculated for each dose and the buffer with or without urea using the Lambert's law corrected to take into account the protein concentration:

$$Cys_{red}/_{protein} = \frac{Abs_{412nm}}{\varepsilon * l * [Protein]}$$

where ε is the extinction coefficient of DTNB and l is the path length, which was 0.1 cm in our setup. The values of the molar extinction coefficients were assumed to be ε = 14,150 and ε = 14,290 $M^{-1} \cdot cm^{-1}$ for the native and the denaturing conditions, respectively.

Results

X-ray irradiated hAR behaves as the activated form in enzymatic assays.

Enzymatic assays reveal that the activity of hAR at a concentration of 2.3 mg/mL increases moderately by ~50% when it receives a dose between 1 and 2 kGy, as compared to the non-irradiated protein, without significant general structural changes as shown by Small Angle X-ray Scattering (SAXS) measurements (Figure 29a). The radius of gyration (R_g) of hAR in solution remains constant within 0.1 nm variation, which is a well-stablished criterion to assess the preservation of the global protein structure under irradiation[55,186], until the protein receives a dose of ~1 kGy. Above 2 kGy, the relative activity of hAR decays concomitantly with the dramatic increase of the radius of gyration as a consequence of radiation damage[61]. The inhibitory effect of *in-vitro* potent ARIs Zenarestat, JF0048, Epalrestat and Tolrestat was checked for non-irradiated hAR, for hAR irradiated to the point where the highest activity is reached without significant protein unfolding or aggregation (1 kGy) and for over-irradiated, damaged hAR (8 kGy) (Figure 29b). While inhibiting native non-irradiated hAR, the studied compounds were significantly less effective in irradiated hAR. The kinetic analysis of non-irradiated and irradiated hAR at 1 kGy (Figure 29c) shows that the catalytic constant k_{cat} value remains unaltered (k_{cat}^{0kGy} = 45.0±3.0 min^{-1} *vs* k_{cat}^{1kGy} = 46.4±3.5 min^{-1}) while the Michaelis constant K_M value exhibits a 7-fold increase under irradiated conditions (K_M^{0kGy} = 55.3±13.1 µM *vs* K_M^{1kGy} = 382.8±141.6 µM). In agreement with previous reports[153,154,163,187], non-irradiated hAR is inhibited by over-saturating concentrations of the substrate D,L-glyceraldehyde. Conversely, irradiated hAR is not inhibited by its substrate at any of the working substrate concentrations, as previously reported for the activated hAR[153,154,163,187]. This behavior is consistent with the higher activity of the irradiated protein with respect to native non-irradiated protein at 6 mM D,L-

glyceraldehyde, while maintaining a similar k_{cat} value. In conclusion, the 1-kGy irradiated form of hAR solution at 2.3 mg/mL and the activated form of hAR found under hyperglycemic and activation conditions[155,188] show the same behavior in the enzymatic analyses of control hAR and hAR in the presence of the ARIs, respectively. X-ray irradiation is thus able to reproduce the functionality of hAR under oxidative stress conditions.

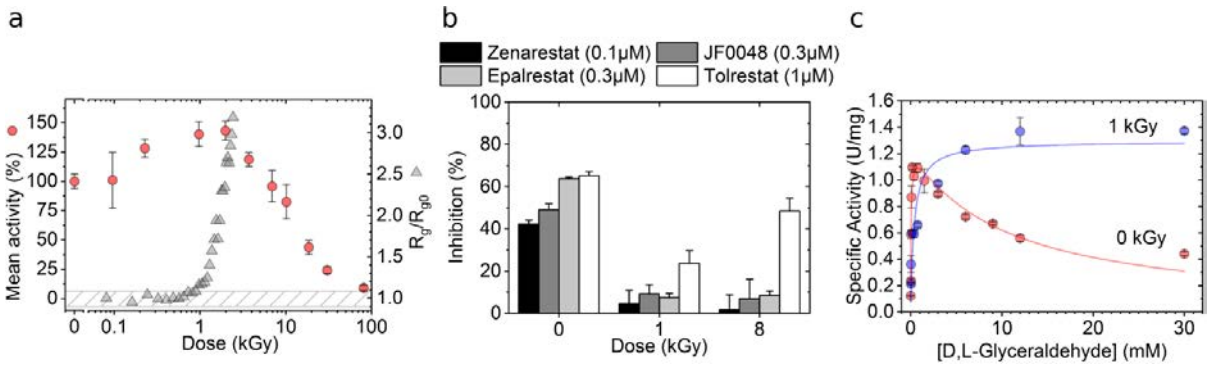

Figure 29 | *Activation of hAR with irradiation. (a) Evolution of hAR normalized mean activity (red circles) and radius of gyration, Rg (gray triangles), as a function of dose. At 6 mM D,L-glyceraldehyde substrate concentration, enzymatic activity increases with irradiation dose until hAR undergoes major structural changes due to radiation damage. (b) Inhibitory potency of Zenarestat (black bars), JF0048 (gray bars), Epalrestat (light gray bars) and Tolrestat (white bars) at 0 kGy, 1 kGy and 8 kGy doses. Tested concentrations close to the IC50 value were used for each compound. The not normalized specific activities of the inhibitors are found in Supp. Fig. 1. (c) Effect of irradiation on hAR kinetics. Native enzyme without irradiation loses 50% of its activity due to excess-substrate inhibition at 6 mM D, L-glyceraldehyde (red circles). Irradiation with a dose of 2 kGy increases the value of the Michaelis constant KM towards substrate by near one order of magnitude (7 times) while the inhibition disappears (blue circles).*

The only change in the crystallographic structure with accumulated dose is the modification of Cys298.

The effects of the X-ray irradiation on the hAR structure were monitored by macromolecular crystallography (MX). Twenty datasets (D1-D20) were collected at 100 K from one single crystal of hAR co-crystallized with NADPH by a large homogeneous X-ray beam profile at the XALOC synchrotron beamline[189]. The absorbed dose per each data set in the exposed region was 0.03 MGy. The crystal was irradiated with an absorbed dose of 0.15 MGy between consecutive datasets, so that the total dose received by the crystal was 3.45 MGy. Data collection statistics for all datasets and refinement statistics for D1 and D20 datasets are shown in Supporting Table 12 and Supporting Table 13. Remarkably, the resolution of the datasets experiences a constant, modest degradation from 0.92 Å in dataset D1 to 1.17 Å in dataset D20. We incidentally note that the doses absorbed by the cryocooled crystals are not to be compared with the absorbed doses by of the protein solution at room temperature, as the effects of the radiation damage strongly depend upon the protein concentration[190] and the temperature[61,191]. Rather than the actual dose, a

coarse correspondence on the radiation damage effects between experiments employing cryocooled protein crystals and those using protein solution at room temperature can be established as the global structure of the protein is preserved in MX and SAXS experiments, respectively.

While the backbone structure remains unchanged, the difference Fourier maps, $F_{obs,n}$-$F_{obs,1}$, reveal side-chain movements and specific radiation damage throughout the entire structure as accumulated absorbed dose increases. Signs of specific damage were not observed in the catalytic tetrad Tyr48, Lys77, His110 and Asp43[192] (Figure 30), which consistently agrees with the similar experimental k_{cat} values measured with the non-irradiated and irradiated enzyme. No conformational changes were observed at any irradiation in the other residues forming the active site of the protein except for the remarkable alteration on Cys298, which was developing upon irradiation (Figure 31), which has been reported to regulate the kinetic and inhibition properties of the enzyme although it does not participate in the catalysis[156,157,159].

Three different structural changes, seen as differential electron densities (blobs) in the difference Fourier maps at a resolution of 1.17 Å (Figure 31a), can be observed in Cys298 as absorbed dose increases: a loss of electron density (red blob) accounting for the disorder and desulfuration induced by the irradiation, an small increase of the electron density (green blob pointed by blue arrows) compatible with an induced movement of the residue towards this region (Supporting Figure 43), and the emergence of a positive electron density (green blob pointed by green arrows) at a distance of 1.47 Å from the Cβ-Cys298 atom for map D20-D1. This latter positive electron density is also observed in Fo-Fc electron density maps with progressively increasing absorbed dose (Figure 31b). The maximum value of this positive electron density in the Fo-Fc map at the highest-dose dataset D20 is placed at a distance of 1.46 Å from the Cβ-Cys298. This distance falls well within the typical covalent C−O distances in both difference Fourier and Fo-Fc maps, suggesting that the new electron density can be explained by the capture of an oxygen atom from the solvent (probably from OH•) by a radicalized intermediate species. This process would effectively change the Cys298 residue present in the native form to a serine residue. The refinement of a serine and cysteine sharing the same Cβ at the 298 position, which is the model with the minimum number of refined variables to avoid over-refinement, leads to unrestrained distances between Cβ atom and Oγ and Sγ atoms of 1.41±0.08 Å and 1.80±0.03 Å, respectively (Figure 31c). These distances are in excellent agreement with the tabulated values of 1.417 Å and 1.801 Å, respectively[193]. Moreover, the unrestrained distance between Cβ and Oγ atoms is constant for all datasets taken at different doses (Figure 31e), suggesting that the bond is stable and thus the residue in this state can properly be identified as serine. Sγ-Cys298 and Oγ-Ser298 are well-defined atoms, as hinted by their atomic displacement parameter (ADP) values (12.24 $Å^2$ and 15.64 $Å^2$, respectively), which are similar to that of the Cβ atom (14.67 $Å^2$).

The refined free occupancies for Sγ-Cys298 and Oγ-Ser298 at the maximum absorbed dose (dataset D20) are 0.68 and 0.25, respectively. As the overall occupancy for both species is lower than one, further minor concurrent species can be hypothesized to be coexisting with either a cysteine or a serine in the 298 position. Same hypothesis can be proposed from the evolution with absorbed dose of the electron density peaks in the difference Fourier maps (Figure 31d). The sum of the maximum intensity of the blobs

attributed to the cysteine desulfuration (Figure 31d, pink circles) and the blob assigned to the Oγ capture (Figure 31d, green squares) is consistently less than one for all datasets (Figure 31d, gray triangles) and increasing with dose, suggesting that these putative extra species in residue 298 would be present in all the doses and that these are created by the X-ray irradiation (Figure 31d, gray triangles).

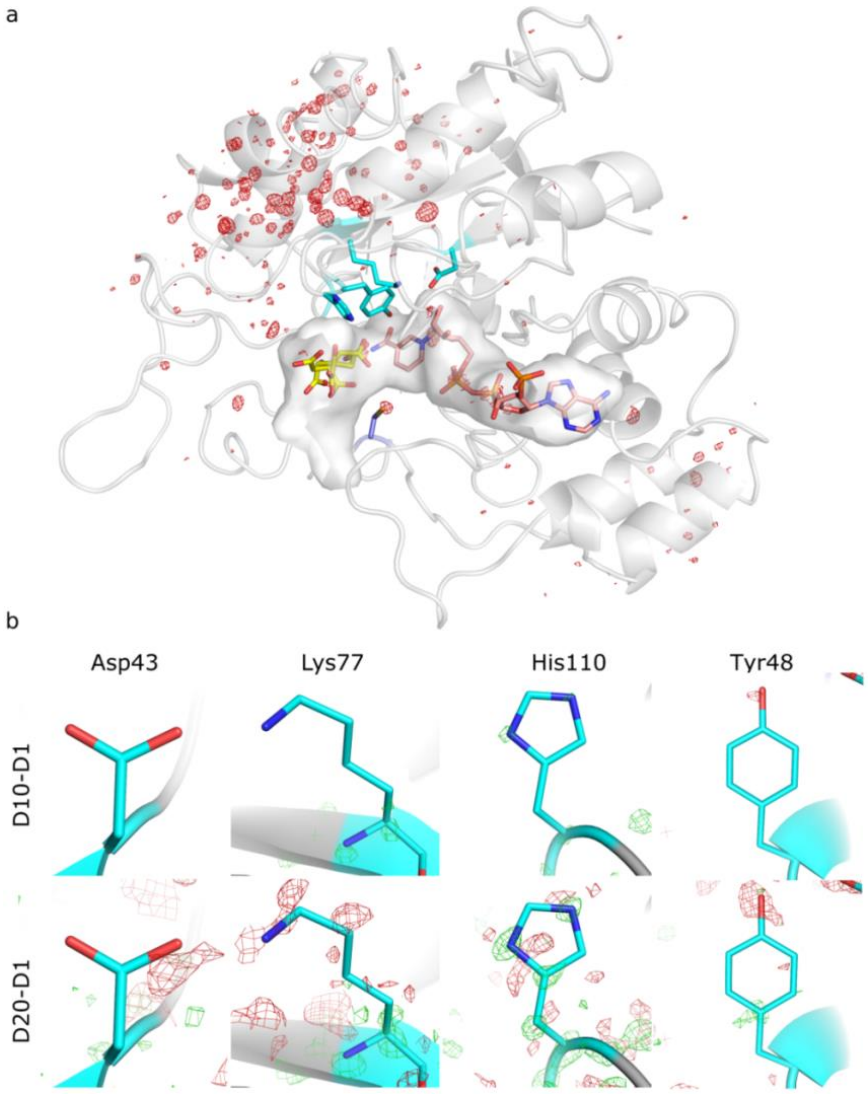

Figure 30 | *Absence of specific radiation damage in the binding pocket and in the catalytic tetrad. (a) Difference Fourier map ($F_{obs,20}$ - $F_{obs,1}$, $\alpha_{calc,1}$) of the most irradiated dataset, D20. The NADPH (pink) and a citrate molecule (yellow) are bound to the binding pocket. The residues of the catalytic tetrad are shown in cyan and Cys298 is navy blue. No signs of specific radiation damage are observed in the vicinity of the binding-pocket surface, except for the Cys298 residue. The map was contoured at 0.56 e/Å^3 (σ = ±5). (b) Detail of the difference Fourier maps ($F_{obs,10}$ - $F_{obs,1}$, $\alpha_{calc,1}$) (top row) and ($F_{obs,20}$ - $F_{obs,1}$, $\alpha_{calc,1}$) (bottom row) on the catalytic tetrad (Asp43, Lys77, His110 and Tyr48) at 1.2 Å resolution, calculated using the amplitudes of datasets D10 or D20 and the initial data set D1 and the phases $\alpha_{calc,1}$ of D1. The maps do not reveal signs of specific radiation damage in the residues of the catalytic tetrad. The D10-D1 and D20-D1 difference Fourier maps of the catalytic tetrad were contoured at 0.33 e/Å^3 (σ = ±4.97 and σ = ±2.97, respectively).*

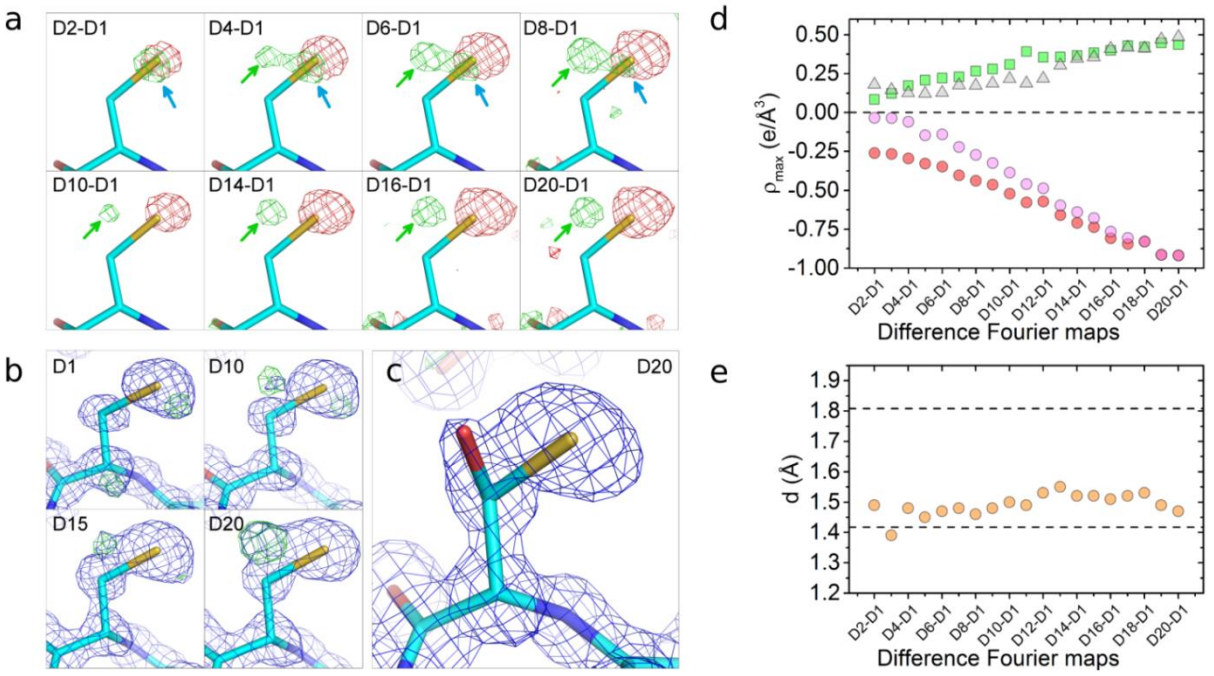

Figure 31 | *Specific changes in Cys298 as a function of dose. (a) Difference Fourier maps ($F_{obs,n}$ - $F_{obs,1}$, $\alpha_{calc,1}$) on Cys298 residue at 1.2 Å resolution, calculated between each dataset n and the initial dataset using the phases of the fresh, not previously irradiated dataset, αcalc,1. The difference Fourier maps are contoured at two different electron density sigma levels (0.145 e/Å³ for the first row, 0.267 e/Å³ for the second row) for clarity. The maps have sigma levels ranging from σ = ±9.00 (D2-D1 map) to σ = ±2.53 (D8-D1 map) for the first row, and from σ = ±3.99 (D10-D1 map) to σ = ±2.41 (D20-D1 map) for the second row. Electron densities colored in green and red represent positive and negative sigma levels, respectively. Red blobs are indicative of the loss of electron density due to movements and desulfuration of Cys298; green blobs pointed by blue arrows show the increase of electron density due to displacements of Cys298 and green blobs pointed by green arrows reveal the appearance of a new atom in the vicinity of Cys298. (b) Electron density maps at 0.92-1.17 Å resolution on the Cys298 residue as a function of dose. In blue, 3Fo-2Fc electron density maps at σ = 1.00; in green, Fo-Fc electron density maps at σ = 2.50 (Fo-Fc maps at σ = ±2.50 were not detected). (c) 2Fo-Fc electron density map for the D20 dataset on the Cys298/Ser298 amino acid. Fo-Fc maps at σ = ±2.50 were not detected. (d) Occupancy-related electron density maxima versus dataset. Red circles: occupancy-related electron density of Sγ atom decreases as Cys298 is desulfurated and the Sγ atom moves; green squares: occupancy-related electron density of Oγ atom increases as the Ser298 is formed; pink circles: loss of the electron density of the Sγ atom due to the desulfuration, calculated as the difference between the two previous electron densities; gray triangles: difference between the electron densities related to the desulfuration of Cys298 (pink circles) and the formation of the Ser298 (green squares). (e) Distances measured in the difference Fourier maps from the Cys298-Cβ atom to the center of the green blobs indicated by green arrows in (a) versus dataset. The top and bottom dashed lines represent the tabulated distances Cβ-Sγ and Cβ-Oγ in cysteine and serine residues, respectively.*

Liquid chromatography tandem mass spectrometry reveals C298S and C298A modifications.

Specific changes in Cys298 were also checked by liquid chromatography tandem mass spectrometry (LC-MS/MS) for the non-irradiated (0 kGy) and for the 1-kGy and 17-kGy irradiated proteins (Figure 32 and Supporting Figure 44). The Cys298-containing peptides were selected after trypsin digestion and fragmented into smaller ionized peptides. As expected, non-irradiated samples showed no modifications at any residue position (Figure 4a). At an irradiation level matching the maximum activity peak of hAR (1 kGy), only two different modifications were detected along the peptide sequence: C298S and C298A (Figure 4b). Over-irradiated samples at 17 kGy showed a C303A modification in addition to the C298S and C298A modifications (Supporting Figure 44), which points to desulfuration of Cys303 by radiation damage. LC-MS/MS measurements thus are consistent with the C298S modification seen in MX experiments in irradiated samples, and suggest that the C298A modification is one of the extra species hypothesized at the 298 position in MX experiments. We do not discard that other species already reported in literature, such as sulfenic acid, could also be present[194,195].

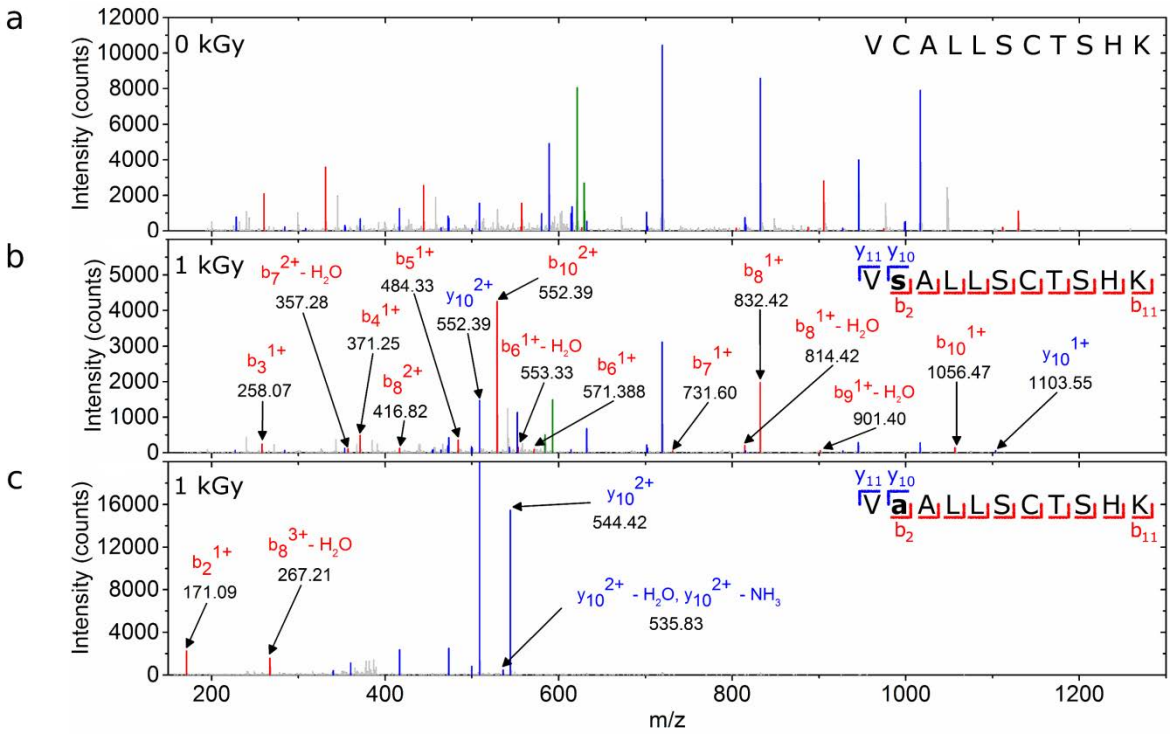

Figure 32 | *LC-MS/MS analysis. LC-MS/MS spectra for non-irradiated protein (b) and for the irradiated protein at 1 kGy subjected to modifications at position 298 from cysteine to serine (b) and alanine (c). Characteristic peaks from the peptide fragmentation are colored in red (b_n), blue (y_n) and green (precursor). Non-characteristic peaks from the sequence are marked in gray. For clarity, only peaks that contain information about modifications are labeled. Only peaks above 1% of the base peak and with match tolerance of 0.6 Da are represented.*

Modeling of the active site with and without inhibitor shows why inhibitors are not effective in the activated form.

Although Cys298 is not a catalytic residue in hAR, the conversion of this residue into a Ser or Ala is key in the functional properties of hAR and in the sensitivity to ARIs. This is explained by the localization of Cys298 between the substrate-binding pocket and the active site, where NADP+ and the catalytic tetrad are found. Cys298 is therefore controlling the substrate accessibility to the active site. The crystallographic structure reveals that the conversion of the Cys298 residue (Figure 33) into a serine (Figure 33b) changes the position of the atom in the γ position of the residue and the type of element, thus modifying the entrance to the substrate-binding pocket. The protein-ligand interaction may be consequently affected. This view is consistent with the enzymatic results described above, which show an increase in the K_M value and a reduction in the potency of the tested inhibitors.

The steric changes in the entrance of the binding pocket severely hinder the interactions between hAR and the inhibitors originally designed against the native form, including a cysteine in the 298 position (Figure 33). The alignment between the D20 dataset crystallographic structure and that with the various inhibitors shows that the Sγ-Cys298 atom has a very low displacement (Supporting Table 15). The distances of the Sγ-Cys298 atom to the closest atom of the studied inhibitors can thus be compared, and are shown to be always above 3 Å. The native form is therefore sterically compatible with the inhibitors, as expected as they were designed against it as a target. On the other hand, in the irradiated protein where cysteine has been replaced with serine, the distance between the Oγ-Ser298 atom and the closest atom of the aligned inhibitors is much shorter and could lead to steric collisions that may affect their binding to the active site. Remarkably, Tolrestat, which had the highest inhibitory potency among the tested compounds on the irradiated enzyme (Figure 29), also shows the longest distance between its closest atom and the Oγ-Ser298 atom, 2.6 Å. This fact reinforces the view that the activated form of hAR interacts less efficiently with inhibitors due to the conversion of Cys298 into Ser298 under oxidative stress conditions.

The activation of hAR is mediated by the free electrons present under oxidative stress conditions.

Specific radiation damage in MX experiments at cryogenic temperatures results essentially from the action of secondary electrons that are generated by the photoelectrons ejected from water and organic molecules. The secondary electrons are highly mobile and can either be spread through the solvent or be tunneled into the protein structure through the main chain until they find electrophilic sites such as metal centers and acidic or sulfur-containing residues, especially cysteine[21]. The other reactive species generated from water radiolysis show low mobility at cryogenic temperatures and their effect on the structural damage can be neglected. To test whether the loss of the thiol group in Cys298 of hAR, observed by MX experiments at cryogenic temperature. can be attributed to electron capture as well in protein solution at room temperature, the relative activity of hAR was measured as a function of dose in the presence of different compounds with variable scavenging properties depending on the reactive species (Figure 34).

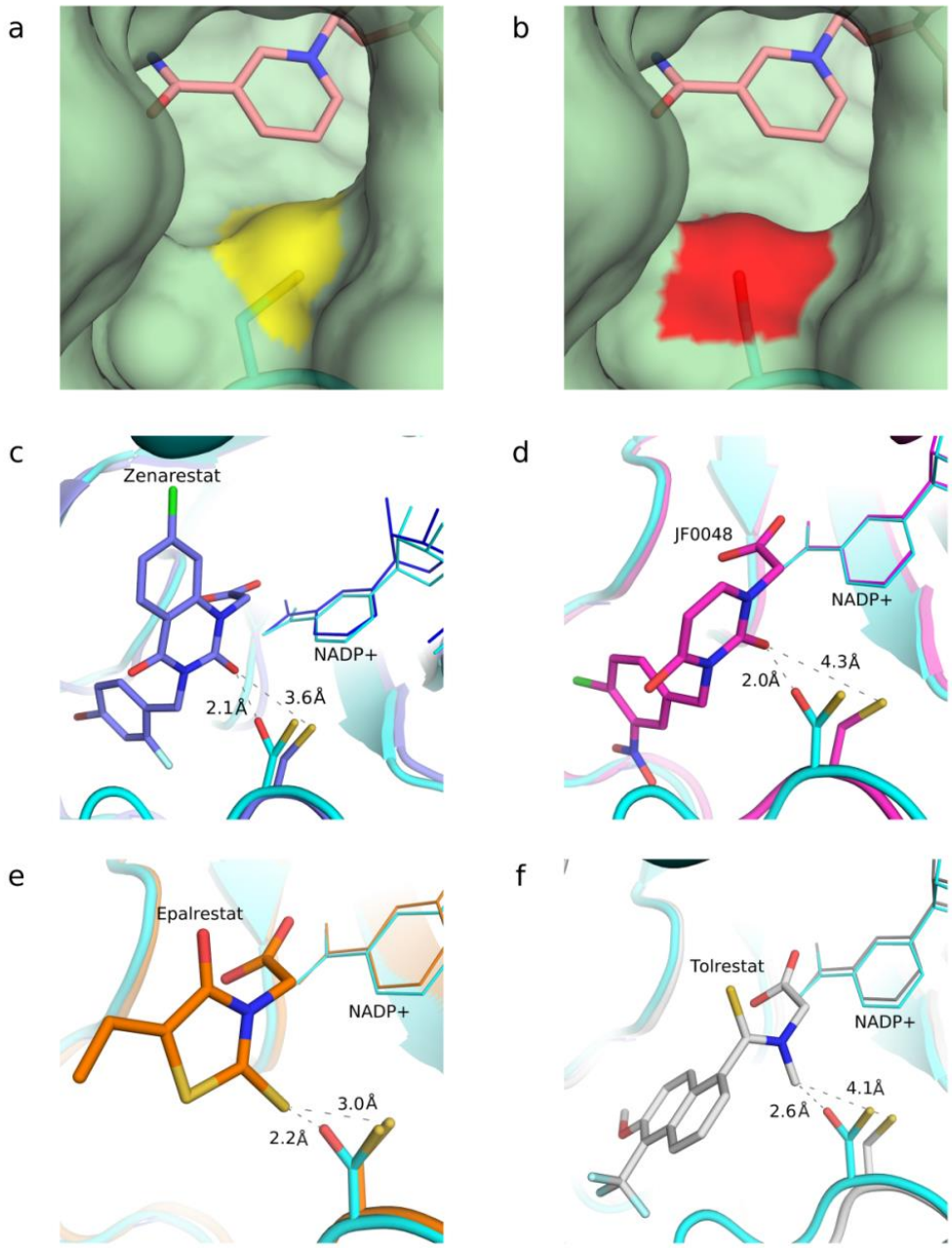

Figure 33 | *Changes on the topology of the hAR pocket entry channel and steric collisions of activated hAR with inhibitors. The conversion of Cys298 into Ser298 modifies the entrance of the substrate-binding pocket. (a) Entrance of the binding pocket of the native form of hAR. The sulfur atom of the Cys298 residue is marked in yellow. (b) Entrance of the binding pocket of the irradiated structure, which shows the Oγ-Ser298 atom, marked in red. In both cases, the nicotinamide ring of the cofactor is shown in pink color. (c-f): Interaction of the studied inhibitors with Cys298 and Ser298. The structure of the D20 dataset (in cyan) is superimposed with the crystallographic structures of hAR including the inhibitors Zenarestat (c, purple, PDB 1IEI), JF0048 (d, magenta, PDB 4XZH), Epalrestat (e, orange, PDB 4JIR) and Tolrestat (f, gray, PDB 1AH3). In all cases the inhibitors, designed against the native form, show severe steric collisions with Oγ-Ser298 but not with Sγ-Cys298. Sulfur atoms are displayed in yellow whereas oxygen atoms are displayed in red.*

Uridine has recently been reported effective only against radiation damage at room temperature and ineffective at cryogenic temperatures[61]. As the electrons are the main mobile reactive species at cryogenic temperatures[20], this suggests that uridine is only effective against ROS and not against free electrons and therefore it may be a probe to test the action of free electrons in the activation process. The relative activity of hAR in the presence of 10 mM uridine (Figure 34a, red dots) is similar to that of hAR without a scavenger (Figure 29a). In both cases the relative activity increases by ~50% at 1 kGy and follows a sigmoidal decay at higher doses. Uridine is thus not preventing the production of the activated form of hAR under X-ray irradiation by the action of its ROS scavenging properties. Nevertheless, uridine still prevents global radiation damage to hAR since the dose at which the enzymatic activity is reduced to the

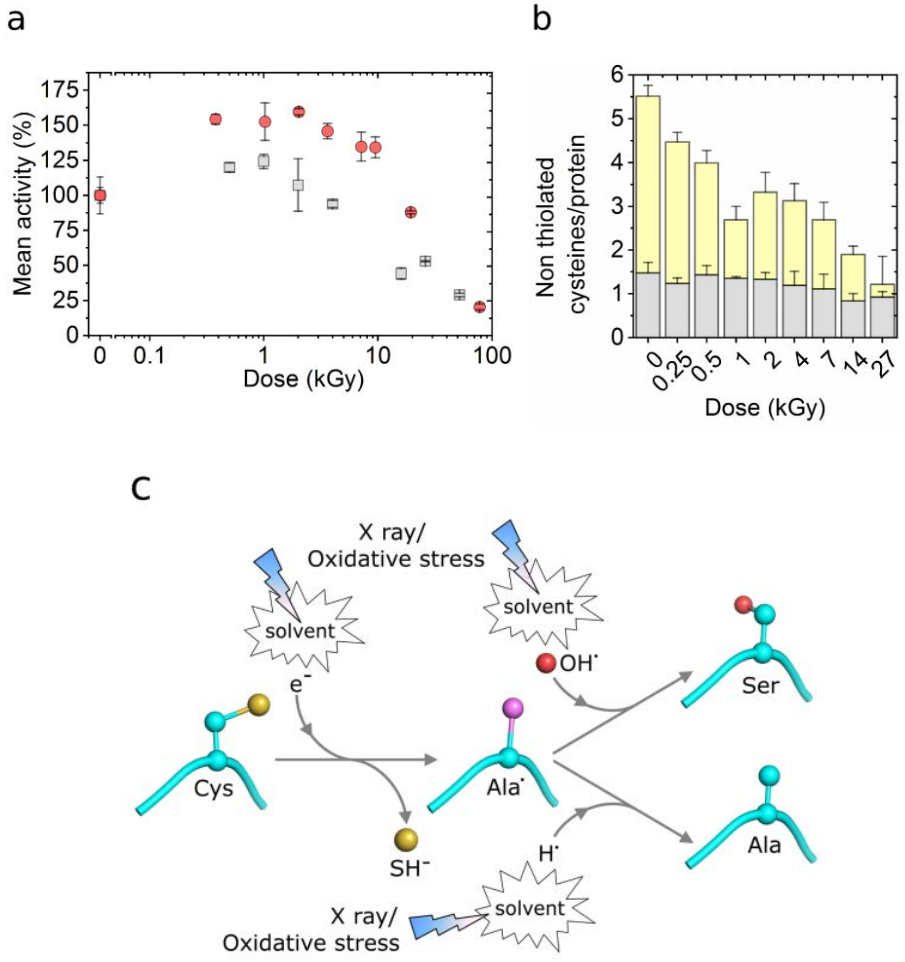

Figure 34 | *Indication that electrons are the main agent for the activation of hAR and proposed mechanism. (a) hAR activity in the presence of 10 mM uridine (red circles) and in the presence of 10 mM uridine plus 40 mM sodium nitrate (gray circles) as a function of irradiation dose. (b) Number of non-thiolated cysteines per protein molecule as a function of dose, as measured by the Ellman's assay. Accessible cysteines (in the absence of urea) are shown in gray, and buried cysteines (revealed in the presence of 8 M urea) are shown in yellow. (c) Scheme of the proposed mechanism for the C298S and C298A conversion induced by X-ray irradiation or oxidative stress. Carbon atoms are colored in cyan, carbon radicals in purple, oxygen atoms in red, and sulfur atoms in yellow. Hydrogen atoms are not shown for clarity.*

half with respect to the maximum relative activity is increased from 10.9±0.8 kGy without uridine (Figure 29a) to 26±2 kGy with 10 mM uridine (Figure 34a). The uridine protective effect is also observed in the conservation of the relative radius of gyration of hAR in solution as measured by SAXS (Supporting Figure 45). To further assess the action of electrons in the activation of hAR, sodium nitrate, a well-known electron scavenger[196], was added to the solution of hAR with 10 mM uridine. By adding 40 mM sodium nitrate, the relative activity of hAR increased only by 25% at 1 kGy with respect to non-irradiated sample, and decreased at higher doses with a sigmoidal behavior (Figure 34a). Remarkably, this activity increase in the presence of sodium nitrate (~25%) was significantly lower than that obtained with uridine only, which is fully compatible with the electron capture as the main source of activation of hAR. Electron capture is also consistent with the quantity of non-thiolated cysteines per hAR molecule as a function of dose measured by the Ellman's assay (Figure 34b). The number of buried non-thiolated cysteines per molecule decays as a function of dose, whereas the number of cysteines accessible to the Ellman's reagent per molecule remains approximately constant.

The activities at different doses and scavengers allow drawing an hypothesis of the mechanism for the conversion of residue Cys298 into Ser298 and to Ala298 based on the cysteine desulfuration involving highly mobile electrons either from the solvent or tunneled through the backbone and absorbed by hAR electrophilic centers such as sulfur atoms[21,197,198]. This hypothesis is reinforced by the desulfuration of non-exposed cysteines observed in our MX experiments under cryogenic conditions, in which electrons are essentially the only mobile reactive species[199]. Whichever the origin of the free electrons is, after the absorption by the cysteine and the loss of the thiol group, residue 298 enters in an excited, metastable state[197,198] which can bond either to a hydroxyl group to form a serine or to a hydrogen radical to form an alanine (Figure 34c). At this stage we cannot exclude other products generated by alternative or complementary mechanisms.

Discussion

The activated form of hAR, as found under oxidative stress conditions *in cellulo*, has been reported to have different kinetic constants than the native form, in particular a much larger K_M value and a more stable k_{cat} value[156,157,200], and to reduce the efficacy in clinical trials of ARIs developed and tested in vitro[156,158,200]. Here we have reproduced this characteristic behavior of the activated hAR in irradiated native protein solution. X rays are massively absorbed by the ~1000 mg/mL water content of the solution, rather than the protein at a concentration of 2.3 mg/mL, and they induce the same reactive species as those found under oxidative stress conditions[164,171], where the activated form has been found[153,155].

A generic unwanted side effect of using X-ray radiation to induce reactive species is to produce global structural changes in the protein as a consequence of the primary interaction of X rays with the protein atoms. These structural changes, which would not be produced in cells under oxidative stress conditions, could in principle limit the capacity of irradiation methods to mimic the catalytic behavior under stress conditions. In this respect, our data do not discard conclusively that there is no such global structural

changes at doses up to 1 kGy, when the values of the kinetic constants and the reduced potency of ARIs suggest a significant activation of hAR. However, our data support that, in case there was such global radiation damage on the protein, it is not affecting the catalytic reaction, as the k_{cat} value does not change at this dose level. Contrarily, the existence of relevant specific changes is supported by the dramatic increase in the K_M value, indicating that the interaction with the substrate is severely affected. The hypothesis that better matches this behavior of the kinetic parameters is a change in the D,L-glyceraldehyde substrate binding pocket. The Cys298 residue, which lies at the entrance of the binding pocket, is an excellent candidate for this change. This hypothesis is consistent with previous literature, which shows that the mutation of Cys298 increases the K_M value by one order of magnitude without severely affecting the k_{cat} value[156,157,200].

As radiation damage is expected to induce a loss of the catalytic activity, it is noticeable that the activity of hAR in solution increases by 50% when irradiated up to 1 kGy (Figure 29a). This moderate increase in the activity can be explained by the saturation at higher concentrations of the D,L-glyceraldehyde substrate which in turn leads to the loss of substrate inhibition, as indicated by the dramatic increase of the K_M value (Figure 29c). Consistently, the activity blockade by the ARIs, which also bind to the D,L-glyceraldehyde pocket, is also reduced (Figure 29b).

The structural studies at atomic resolution are in line with our proposed hypothesis that the presence of a serine or alanine in residue 298 instead of cysteine in an oxidative stress environment is causing the activation of the hAR. Other species reported to oxidize Cys298 such as sulfenic acid can not be excluded[195] to intervene in the activation. Irradiation of the native form induces the same structural changes at atomic level as those suggested for the activated form[155,157,187,201], that is, the modification of the residue 298 while the catalytic tetrad, as well as all the other residues around the binding pocket, remain unaltered (Figure 30). According to the results presented here, the activated form differs structurally from the native form by the replacement of the Cys298 residue by Ser298 and, to a lesser extent, by Ala298. We can not exclude further changes at this position which might as well modify the interaction with ARIs. The modification of this key residue affects the entrance to the substrate-binding pocket, resulting in an altered binding of the substrate and of the inhibitors, which finally leads to a reduction in the inhibitory potency of the drugs initially designed to bind to the native form of hAR.

Incidentally, we note that more substrates other than D,L-glyceraldehyde might be tested. However, given that glyceraldehyde is one of the smallest substrates for hAR, the accessibility of this substrate to the binding pocket is high, as it can be accommodated into the altered binding pocket more easily than other common, larger substrates such as glucose, xylose or 4-hydroxynonenal, among others. Therefore, it can be expected that the potency loss of the inhibitor compounds observed using glyceraldehyde as a substrate will also appear at least in a similar extent using other common substrates under the same oxidative stress conditions.

The conversion of the residue Cys298 into Ser298 and Ala298, and possibly other species, is hypothesized to be triggered by the presence of free electrons available under X-ray irradiation, as indicated by the lesser increase of activity upon irradiation in the presence of sodium nitrate (a known free electron scavenger) compared to the higher increase when adding uridine (a ROS scavenger) in the solution. The free electrons might be either induced in the solvent or tunneled into the protein structure through the protein main chain.

In spite of the degradation of the modified proteins and the continuous expression of the native form in living cells, the described activated forms prevail in cells from diabetic patients as the proteins newly expressed are modified recurrently under permanent oxidative stress conditions. Therefore, we propose that ARIs should be designed against the activated forms of hAR, here generated by X-ray irradiation, which show a similar behavior against ARIs to the activated forms of hAR found under hyperglycemic conditions[153,154,163]. The attempts to develop ARIs employing the native, genome coded form of hAR risk to fail when tested in real diabetic tissues or patients, as it happened in many previous cases[153,154]. In particular, ARIs should be designed excluding the interaction of the inhibitor with Sγ in Cys298 and taking into account the Oγ in residue Ser298 appearing in the activated form. In order to best mimic the physiological situation, we therefore suggest using irradiated protein in high-throughput drug discovery and drug development studies, including in vitro testing, to complement studies in site-directed mutants and to increase the rate of success of ARIs in subsequent clinical trials. The crystal structure of the irradiated hAR presented in this study (PDB: 6F8O), which includes the double modification C298S and C298A with respect to the native form, can also be employed as a target for an effective rational in silico drug discovery. The structure would allow taking into account and modeling the interactions between a lead molecule and the distinct active-site pocket of active hAR, especially near the residue 298. Furthermore, since the mechanisms that involve reactive species are common in oxidative stress and/or irradiation conditions, the controlled method of irradiation with X-rays presented in this work could become an instrumental approach to study other proteins that are also exposed to oxidative stress environments, like those related to cancer, Parkinson's, Alzheimer's or inflammatory disease.

Data availability

The data generated by the enzymatic assays, the liquid chromatography-tandem mass spectrometry measurements and the crystallography and small angle scattering experiments, including the raw images which support the findings of this study, are available from the Zenodo repository with the identifier DOI: 10.5281/zenodo.1265630. The hAR structures obtained using datasets D1 (non-irradiated), D5, D15 and D20 (maximum irradiation) are uploaded on the PDB database (www.rcsb.org) with ID 6F7R, 6F81, 6F82, 6F84, 6F8O, respectively.

Discussió general

L'addició de compostos *scavenger* dins de les mostres experimentals en SAXS i MX és una estratègia efectiva contra el DR. Els resultats experimentals descrits en els Capítols 1 i 2 d'aquesta Tesi demostren que els nucleòsids i les bases nitrogenades testejades són efectius compostos *scavenger*.

En el Capítol 1 s'ha caracteritzat la uridina com a compost scavenger per experiments de MX. S'ha demostrat que aquest compost té propietats mitigadores del DR global a temperatura ambient. No obstant, no esperem que l'ús de la uridina com a scavenger per MX s'estengui entre la comunitat per diferents raons: i) la difracció a temperatures criogèniques i l'emergència d'altres maneres de col·lectar dades, com ara la *serial crystallography*, han desplaçat l'interès per a utilitzar compostos *scavenger*, ii) el benefici de poder doblar, en alguns casos, la dosi tolerada pel cristall és en detriment d'arriscar-se a malmetre els preuats cristalls a l'hora d'introduir un additiu en altes concentracions[68] i iii) el dany per DR indirecte es minimitza significativament difractant a 100K. En relació a l'últim punt, cal fer notar que la col·lecció de dades a 100K està totalment implementada en la majoria de línies de llum de MX i que la col·lecció de dades en MX a temperatures inferiors o iguals a 100K representa el 86% de de les estructures dipositades al Protein Data Bank. No obstant, els resultats obtinguts per a la uridina com a *scavenger* efectiu a nivell global en cristalls de lisozim difractats a temperatura ambient és un fet molt remarcable donat que és un fet poc comú[38,67].

En el capítol 2, es caracteritzen tres compostos nucleòsids i una bases nitrogenada (5-metil uridina, uridina, citidina i citosina). Els resultats mostren clarament que aquests compostos són excepcionalment adients per als experiments de SAXS i, de fet, són els compostos *scavenger* amb millors propietats mitigadores que s'ha caracteritzat en el camp, per davant dels additius més comuns com el glicerol. D'entrada, aquests compostos no redueixen significativament el contrast entre la proteïna i el solvent. A més, els compostos s'han provat en diferents proteïnes amb diferents pesos moleculars (des de 7 a 250 kDa) i en solucions tamponants amb diferent pH (des de pH 3 a pH 8). Utilitzant aquests compostos s'han pogut resoldre a baixa resolució estructures que no es podien resoldre d'altra manera. Aquest fet és molt remarcable donat que millora la qualitat de les dades que actualment s'obtenen ens els experiments de SAXS. Més encara, l'alt poder mitigador del DR d'aquests compostos dona peu a ampliar l'abast de la

tècnica experimental de SAXS cap a proteïnes amb baixos pesos moleculars o a solucions altament diluïdes. Creiem que la futura publicació d'aquests resultats farà que l'ús d'aquests compostos s'estengui entre la comunitat experimental.

En el capítol 3, s'estudien les propietats mitigadores del DR de l'hidrogel peptídic Fmoc-CF en cristalls de lisozim a temperatura ambient en experiments de MX. Els hidrogels peptídics, per les seves propietats físico-químiques, estan despertant l'interès en el camp de la biomedicina per a la encapsulació de fàrmacs[139,202–204], en cristal·lografia de proteïnes per millorar la qualitat dels cristalls[134,205,206] i, sobretot, en aplicacions biotecnològiques[130,207–210], algunes d'elles amb base cristal·lina[138]. Els resultats obtinguts en el Capítol 3 demostren per primer cop que l'hidrogel Fmoc-CF efectivament proveeix protecció a nivell específic en cristalls de lisozim difractats a temperatura ambient. Aquests nou resultat és rellevant en dues vessants diferents. Per una banda, els resultats obtinguts demostren que l'hidrogel Fmoc-CF té propietats antioxidants útils en experiments *in vivo*. Per l'altra banda, l'hidrogel Fmoc-CF pot ser útil també per a la mitigació del DR en experiments de MX. En ambdues aplicacions, les molècules de lisozim actuen com a sondes en la detecció de les modificacions produïdes per ROS i per altres espècies reactives generades durant la irradiació.

Des del punt de vista metodològic, el Capítol 3 aporta una nova visió sobre l'anàlisi de les dades experimentals en MX que pateixen DR. L'escalat de les dades de difracció a temperatura ambient en dues capes de resolució diferents, l'alta resolució (40-3 A) i la baixa resolució (3-1.7 A), permet la visualització lliure d'artefactes del DR específic en MX, donat que es corregeixen els errors sistemàtics provocats pel dany global que vicien les dades. Aquesta manera d'escalar les dades a temperatura ambient no ha estat reportada en la literatura, i és rellevant per a la comunitat científica donat que sovint s'assenyala el soroll de les dades com a causant de l'aparició d'artefactes en els resultats[90]. De fet, RIDL[211], un programa recentment publicat dedicat a la generació automatitzada de mapes de diferències per a l'estudi del DR en MX, no distingeix entre dades col·lectades a temperatura ambient o criogèniques i en el que apareixen artefactes com els de la Figura 26. Per resoldre el problema que presenta aquest programa, s'ha creat un programa anàleg a RIDL que escala les dades de manera automàtica en capes de resolució i produeix mapes de diferències de densitat electrònica lliures d'artefactes.

En el capítol 4 s'ha estudiat un enzim, l'Aldosa Reductasa (hAR, AKR1B1), rellevant en les complicacions secundàries de la diabetis en condicions d'estrès oxidatiu, que són les condicions en què aquesta proteïna és més rellevant des del punt de vista farmacològic. Donat que les espècies reactives provocades per la irradiació per raigs X són les mateixes que les que es presenten en estrès oxidatiu, hem irradiat de manera controlada l'enzim per estudiar-lo en condicions que es presenten en condicions d'acumulació de ROS. D'aquest manera hem observat per assaigs enzimàtics i per tècniques estructurals (MX i MS/MS-LS) l'aparició de la forma activada d'aquest enzim, tal com ha estat descrita en la literatura en condicions d'hiperglucèmia i en les formes mutants C298A i C298S de la proteïna nativa. La forma activada de la hAR és descrita, per una banda, per unes constants cinètiques diferents de la forma nativa: la

constant de Michaelis K_M es veu alterada un ordre de magnitud ($K_M^{activada} \approx 10\ K_M^{nativa}$), mentre que el valor de la constant catalítica k_{cat} es veu poc alterat ($k_{cat}^{activada} \approx k_{cat}^{nativa}$). Per altra banda, en la forma activada es descriu una pèrdua d'inhibició dels compostos que eren potents sobre la forma nativa. Totes aquestes característiques s'han comprovat experimentalment en el Capítol 4 mitjançant la irradiació de l'enzim i la posterior caracterització cinètica. En aquest treball hem demostrat que la hAR nativa irradiada deixa d'estar inhibida per excés de substrat, i passa a tenir les propietats de la forma activa. La forma activada s'ha pogut caracteritzar estructuralment mitjançant MX. En presència d'irradiació, la tètrada catalítica no es veu alterada, i de fet l'únic canvi proper al lloc d'unió al substrat i al cofactor és el canvi en el residu C298, que es destiolitza i en part s'oxida. Aquest canvi representa de manera efectiva un canvi del residu, que passa de ser una Cys a Ser o Ala, i potser cap a alguna altra espècie no detectada que no descartem. Els resultats estructurals amb aquestes *mutacions efectives* C298S i C298A s'han dipositat al Protein Data Bank. Aquestes estructures es poden utilitzar com a diana en el disseny nous fàrmacs.

El mecanisme de l'activació de l'aldosa reductasa s'ha pogut proposar a partir de la utilització de compostos *scavenger*, amb efectes diferents en els diversos radicals. Aquest mecanisme, i la metodologia emprada per aconseguir els resultats és general i pot ser aplicada en altres enzims implicats en processos relacionats amb l'estrès oxidatiu. En aquest sentit, creiem que la metodologia emprada en el Capítol 4, que combina irradiació amb llum de sincrotró, assaigs enzimàtics, MX, SAXS i espectroscòpia de masses, pot esdevenir seminal en l'estudi funcional d'enzims implicats en malalties com ara neoplàsies, Parkinson o Alzheimer.

Conclusions

Capítol 1:

1. La uridina mitiga els efectes globals del DR en MX a temperatura ambient, en concentracions entre 250 i 1000 mM. L'efecte protector és proporcional a la concentració d'uridina i és màxim a 1 M. Aquest efecte protector permet incrementar la dosi crítica en ~70% i fer decréixer els *B-factors* en ~40%.

2. La uridina no mitiga els efectes específics del DR en MX a temperatura ambient. Tampoc s'observa protecció contra el DR en MX a temperatura criogènica (100K).

3. L'evolució dels *B-factors* en MX a temperatura ambient es modela millor amb una corba exponencial, en lloc d'una recta com estava reportat en la literatura.

4. En dosis moderades, el DR en MX a temperatura ambient no depèn de la taxa de dosi absorbida dins del rang estudiat (13.8 i 20 kGy/s). A dosis altes (per sobre de 1.2 MGy), els cristalls es veuen menys afectats pel DR amb taxes de dosi de 20 kGy/s.

Capítol 2:

5. La uridina, la 5-metil uridina, la citidina i la citosina són compostos *scavenger* efectius per a la reducció del DR en experiments de SAXS.

6. La addició de 100 mM de uridina, 5-metil uridina, citidina o citosina genera més contrast entre la mostra i el seu corresponent *buffer* que no pas 678 mM de glicerol.

7. L'addició de 100 mM de uridina, 5-metil uridina, citidina o citosina en mostres de SAXS no altera els paràmetres estructurals derivats d'aquestes.

8. La adició de 100 mM de 5-metil uridina en mostres de SAXS permet millorar la col·lecció de dades per als angles més alts ($3 \leq q \leq 6$ nm^{-1}). Aquest fet permet millorar la resolució de les dades obtingudes per aquesta tècnica.

9. L'addició de 100 mM de 5-metil uridina permet col·lectar dades de SAXS a baixes concentracions i a baixos pesos moleculars de proteïna, fet que amplia les possibilitats de la tècnica.

10. Els models estructurals resultants de les dades de SAXS per a baixes concentracions i baixos pesos moleculars de proteïna milloren en la presència de 100 mM de 5-methyl uridina.

Capítol 3:

11. L'hidrogel Fmoc-CF no protegeix del DR global a cristalls de lisozim difractats a temperatura ambient.

12. L'hidrogel Fmoc-CF, en canvi, sí protegeix a nivell específic del DR global en cristalls de lisozim difractats a temperatura ambient. El nivell de DR en ponts disulfur i metionines és menor en cristalls de lisozim crescuts en presència de Fmoc-CF, respecte de cristalls de lisozim crescuts en agarosa.

13. La mitjana de la desviació quadràtica (RMS) de la densitat electrònica mitjana d'un mapa de diferències [ACT1]és una mètrica robusta per a l'estudi del dany per radiació específic. Es creu que aquest resultat és aplicable en qualsevol estudi de DR en MX amb independència de la mostra.

14. Els mapes de diferència han de ser corregits pel dany global en experiments de MX a temperatura ambient mitjançant un escalat de les dades per capes de resolució.

Capítol 4:

15. La aldosa reductasa (hAR) irradiada a 1 kGy té les mateixes característiques cinètiques que la hAR sense irradiar amb les mutacions C298 i C298A. La hAR irradiada a 1 kGy també té les mateixes característiques cinètiques que la forma activa descrita *in vivo* en condicions d'hiperglucèmia.

16. La hAR sense irradiar presenta inhibició per excés de substrat per sobre de 2 mM de D,L-gliceraldehid. La hAR irradiada a 1 kGy deixa d'estar inhibida per excés de substrat (D,L-gliceraldehid) i per això mostra més activitat.

17. Els inhibidors Tolrestat, Epalrestat, JF0048 i Zenarestat deixen d'inhibir a la hAR a 1 kGy de irradiació.

18. Malgrat la irradiació, la hAR manté les mateixes condicions de monodispersitat fins a 1 kGy, i per tant és la dosi màxima a la que es pot estudiar l'enzim.

19. Cap residu proper al lloc d'unió al substrat i al cofactor, inclosa la tètrada catalítica, es veu alterat per la irradiació a altes dosis, excepte pel residu Cys298. En aquest residu el tiol es perd i s'observa les *mutacions efectives* C298S i C298A. No es descarten més formes en el mateix residu.

20. La superposició de l'estructura cristal·logràfica de la hAR a 3.45 MGy amb les estructures dels complexos amb Tolrestat, Epalrestat, JF0048 i Zenarestat mostren possibles col·lisions estèriques entre els inhibidors i el residu S298. Això explica el comportament de molts inhibidors de la hAR, que perden potència quan la hAR presenta la forma activada.

21. Es proposa que el mecanisme de l'activació de la hAR comença amb la captura d'un electró en el residu C298.

Apèndix

Supporting information: Uridine as a new scavenger for synchrotron-based structural biology techniques

The results presented in this appendix are has been published in:

Journal of Synchrotron Radiation. (2017). **24**, 53-62. DOI: 10.1107/S1600577516018452

Authors: Crosas, E.*, **Castellví, A**.*, Crespo, I., Fulla, D., Gil-Ortiz, F., Fuertes, G., Kamma-Lorger, C. S., Malfois, M., Aranda, M. A. G. & Juanhuix, J.

*These authors contributed equally to this work

Supporting Table 4 | *Crystal definition and classification according to the concentration of uridine, the beam size dimensions, dose rate and temperature. Crystals 12 and 16 were used to evaluate site-specific radiation damage.*

Crystal Number	[Uridine] (mM)	Beam size FWHM (h *x* v µm)	Dose Rate (kGy s^{-1})	T (K)
1-4	0	100 x 85	13.8	RT
5-8	200	100 x 85	13.8	RT
9-11	500	100 x 85	13.8	RT
12-15	0	90 x 80	20.0	RT
16-18	1000	90 x 80	20.0	RT
19-21	0	86 x 78	90.0	100
22	500	86 x 78	90.0	100
23-25	1000	86 x 78	90.0	100

Supporting Table 5 | *Data collection statistics for all crystals collected at room temperature extracted from the initial integration by XDS. Resolution range is 50-2.0 Å. Space group for all crystals is $P4_32_12$. Crystals 12 and 16 are used in the main text to evaluate the site-specific radiation damage.*

Crystal 1 (No uridine)

Dose (MGy)	Unique reflections	Complete-ness (%)	<I>/σ(I)	R-meas (%)	B-factor (Å^2)	a = b (Å)	c (Å)	Mosaicity (deg)	CC1/2	I_n / I_0
0.31	8495	98.9 (99.5)	30.76 (15.03)	4.5 (11.1)	23.15	79.2	37.9	0.034	99.9	1.00
0.62	8508	99.0 (99.5)	21.22 (8.48)	6.1 (21.4)	26.33	79.3	37.9	0.106	99.9	0.86
0.93	8492	98.8 (99.2)	21.12 (6.33)	6.2 (30.7)	30.28	79.3	37.9	0.085	99.9	0.64
1.24	8480	98.8 (99.4)	15.39 (2.08)	9.2 (90.6)	37.24	79.3	37.8	0.096	99.9	0.36
1.55	8484	99.0 (99.0)	6.27 (0.33)	27.9 (520.4)	44.99	79.3	37.8	0.184	99.4	0.14

Crystal 2 (No uridine)

Dose (MGy)	Unique reflections	Complete-ness (%)	<I>/σ(I)	R-meas (%)	B-factor (Å^2)	a = b (Å)	c (Å)	Mosaicity (deg)	CC1/2	I_n / I_0
0.31	8559	99.6 (99.9)	35.66 (19.06)	3.8 (8.8)	23.12	79.2	37.9	0.033	99.9	1.00
0.62	8564	99.6 (99.8)	33.48 (15.42)	4.0 (11.1)	25.68	79.3	37.9	0.033	99.9	0.86
0.93	8569	99.7 (99.9)	30.43 (10.7)	4.3 (16.3)	29.71	79.3	37.9	0.041	99.9	0.66
1.24	8564	99.8 (99.9)	22.01 (4.29)	6.0 (45.3)	35.84	79.3	37.9	0.067	99.9	0.41
1.55	8538	99.7 (99.6)	11.56 (0.84)	15.9 (239.5)	40.96	79.3	37.8	0.147	99.8	0.21

Crystal 3 (No uridine)

Dose (MGy)	Unique reflections	Complete-ness (%)	<I>/σ(I)	R-meas (%)	B-factor (Å^2)	a = b (Å)	c (Å)	Mosaicity (deg)	CC1/2	I_n / I_0
0.31	8564	99.8 (99.8)	39.44 (19.00)	3.4 (8.6)	24.14	79.2	37.9	0.054	99.9	1.00
0.62	8568	99.7 (99.4)	36.03 (14.52)	3.6 (11.5)	27.67	79.2	37.9	0.057	100.0	0.80
0.93	8575	99.8 (99.9)	28.21 (7.02)	4.7 (30.1)	33.91	79.3	37.9	0.072	100.0	0.54
1.24	8567	99.8 (99.6)	14.39 (1.06)	11.8 (200.8)	43.80	79.4	37.8	0.148	99.9	0.26
1.55	8300	97.2 (92.0)	5.37 (-)	45.8 (-)	52.79	79.4	37.8	0.270	99.0	0.09

Crystal 4 (No uridine)

Dose (MGy)	Unique reflections	Complete-ness (%)	<I>/σ(I)	R-meas (%)	B-factor (Å^2)	a = b (Å)	c (Å)	Mosaicity (deg)	CC1/2	I_n / I_0
0.62	8569	99.7 (100)	30.04 (12.81)	4.4 (13.1)	26.33	79.3	37.9	0.037	99.9	0.84

0.93	8577	99.7 (99.9)	25.68 (8.59)	5.0 (20.8)	30.64	79.3	37.9	0.039	99.9	0.62
1.24	8589	99.7 (99.5)	18.32 (3.07)	7.2 (68.4)	38.45	79.4	37.9	0.054	99.9	0.36
1.55	8596	99.7 (99.0)	8.00 (0.34)	20.3 (512.6)	50.12	79.5	37.9	0.107	99.8	0.13

Crystal 5 (200mM uridine)

Dose (MGy)	Unique reflections	Complete-ness (%)	<I>/σ(I)	R-meas (%)	B-factor (Å2)	a = b (Å)	c (Å)	Mosaicity (deg)	CC1/2	I_n / I_0
0.31	8329	97.2 (98.7)	34.08 (16.16)	3.8 (10.3)	24.29	79.1	37.9	0.034	99.9	1.00
0.62	8334	97.2 (98.3)	32.18 (13.72)	4.0 (12.1)	26.41	79.2	37.9	0.036	99.9	0.88
0.93	8332	97.2 (98.8)	29.41 (10.30)	4.3 (15.9)	29.55	79.2	37.9	0.041	99.9	0.72
1.24	8336	97.1 (97.5)	23.71 (6.37)	5.1 (28.6)	34.05	79.3	37.9	0.049	99.9	0.52
1.55	8351	97.3 (98.5)	16.6 (2.09)	7.7 (93.1)	41.62	79.3	37.9	0.073	99.9	0.31
1.86	8305	96.7 (94.9)	7.96 (0.13)	20.8 (1134)	54.50	79.4	37.8	0.145	99.8	0.12

Crystal 6 (200mM uridine)

Dose (MGy)	Unique reflections	Complete-ness (%)	<I>/σ(I)	R-meas (%)	B-factor (Å2)	a = b (Å)	c (Å)	Mosaicity (deg)	CC1/2	I_n / I_0
0.31	8535	99.5 (99.0)	36.25 (18.51)	3.7 (9.2)	23.73	79.2	37.9	0.039	99.9	1.00
0.62	8539	99.4 (98.8)	34.22 (15.42)	3.8 (10.9)	26.14	79.2	37.9	0.044	99.9	0.89
0.93	8539	99.5 (98.9)	32.71 (11.32)	3.9 (15.4)	29.61	79.3	37.9	0.054	100.0	0.76
1.24	8539	99.5 (98.7)	28.64 (6.04)	4.6 (30.8)	33.96	79.3	37.9	0.079	100.0	0.58
1.55	8537	99.5 (99.0)	19.27 (1.98)	8.2 (100.0)	39.00	79.4	37.9	0.132	99.9	0.38
1.86	8575	99.5 (98.7)	10.38 (0.54)	19.0 (345.5)	43.41	79.4	37.9	0.192	99.7	0.22

Crystal 7 (200mM uridine)

Dose (MGy)	Unique reflections	Complete-ness (%)	<I>/σ(I)	R-meas (%)	B-factor (Å2)	a = b (Å)	c (Å)	Mosaicity (deg)	CC1/2	I_n / I_0
0.31	8541	99.7 (99.9)	30.78 (13.4)	4.4 (12.1)	24.49	79.1	38.0	0.043	99.9	1.00
0.62	8553	99.8 (99.9)	28.78 (11.5)	4.7 (14.6)	26.46	79.1	37.9	0.041	99.9	0.88
0.93	8565	99.8 (99.9)	26.25 (8.97)	5.0 (19.1)	29.11	79.2	37.9	0.042	99.9	0.74
1.24	8582	99.9 (99.5)	22.52 (5.55)	5.8 (33.0)	33.46	79.2	37.9	0.047	99.9	0.55
1.55	8594	99.8 (99.4)	15.97 (1.82)	8.5 (112.3)	41.48	79.3	37.9	0.063	99.9	0.33
1.86	8597	99.7 (99.3)	7.8 (0.16)	23.6 (954.9)	54.46	79.5	37.8	0.102	99.7	0.13

Crystal 8 (200mM uridine)

Dose (MGy)	Unique reflections	Complete-ness (%)	<I>/σ(I)	R-meas (%)	B-factor (Å2)	a = b (Å)	c (Å)	Mosaicity (deg)	CC1/2	I_n / I_0

0.31	8452	98.6 (99.3)	31.2 (16.78)	4.3 (9.9)	23.40	79.1	37.96	0.026	99.9	1.00
0.62	8460	98.6 (99.2)	29.3 (14.4)	4.5 (11.5)	25.21	79.1	37.95	0.025	99.9	0.88
0.93	8463	98.6 (99.1)	27.54 (11.27)	4.6 (15.2)	28.25	79.17	37.94	0.027	99.9	0.74
1.24	8485	98.8 (98.7)	24.32 (7.00)	5.1 (25.5)	33.20	79.24	37.93	0.04	99.9	0.57
1.55	8491	98.7 (99.2)	17.34 (2.17)	7.5 (90.8)	41.78	79.34	37.92	0.068	99.9	0.34
1.86	8502	98.5 (98.1)	8.84 (0.22)	18.3 (647.9)	53.81	79.46	37.90	0.111	99.8	0.14

Crystal 9 (500mM uridine)

Dose (MGy)	Unique reflections	Complete-ness (%)	<I>/σ(I)	R-meas (%)	B-factor (Å2)	a = b (Å)	c (Å)	Mosaicity (deg)	CC1/2	I_n / I_0
0.31	8337	97.3 (98.8)	35.49 (18.22)	3.7 (9.0)	23.88	79.10	37.98	0.039	99.9	1.00
0.62	8345	97.3 (98.7)	33.61 (16.13)	3.8 (10.2)	25.39	79.13	37.97	0.037	99.9	0.90
0.93	8366	97.5 (99.0)	31.82 (13.59)	3.9 (12.1)	27.65	79.18	37.97	0.039	99.9	0.80
1.24	8365	97.4 (98.7)	30.35 (10.4)	4 (16.0)	30.74	79.23	37.97	0.041	99.9	0.68
1.55	8391	97.5 (99.0)	26.57 (6.39)	4.5 (27.6)	35.18	79.28	37.97	0.052	100	0.53
1.86	8387	97.5 (98.9)	20.06 (2.48)	6.2 (76.4)	41.61	79.33	37.97	0.073	99.9	0.35
2.17	8348	97.5 (98.9)	11.64 (0.61)	13.9 (296.3)	47.10	79.34	37.96	0.123	99.8	0.19

Crystal 10 (500mM uridine)

Dose (MGy)	Unique reflections	Complete-ness (%)	<I>/σ(I)	R-meas (%)	B-factor (Å2)	a = b (Å)	c (Å)	Mosaicity (deg)	CC1/2	I_n / I_0
0.31	8551	99.8 (99.9)	38.18 (21.88)	3.6 (7.9)	23.53	79.1	38.0	0.048	99.9	1.00
0.62	8551	99.8 (99.7)	36.67 (19.18)	3.6 (9.1)	25.36	79.1	38.0	0.049	99.9	0.92
0.93	8559	99.8 (99.6)	36.27 (16.37)	3.6 (10.4)	27.48	79.1	38.0	0.05	99.9	0.82
1.24	8565	99.8 (99.8)	32.81 (12.89)	3.8 (13.1)	30.26	79.2	38.0	0.055	99.9	0.71
1.55	8576	99.8 (99.7)	31.76 (9.11)	3.8 (19.6)	34.05	79.2	38.0	0.06	100	0.58
1.86	8585	99.8 (99.6)	26.11 (4.36)	4.8 (46.0)	39.36	79.3	38.0	0.08	100	0.41
2.17	8588	99.8 (99.5)	14.09 (1.12)	12.0 (189.6)	43.21	79.2	37.9	0.148	99.9	0.25

Crystal 11 (500mM uridine)

Dose (MGy)	Unique reflections	Complete-ness (%)	<I>/σ(I)	R-meas (%)	B-factor (Å2)	a = b (Å)	c (Å)	Mosaicity (deg)	CC1/2	I_n / I_0
0.31	8538	99.9 (99.7)	29.31 (9.98)	4.9 (19.0)	26.03	79.1	37.9	0.159	99.9	1.00
0.62	8541	99.8 (99.3)	27.47 (8.40)	5.2 (22.6)	27.58	79.1	37.9	0.163	99.9	0.91
0.93	8550	99.9 (99.5)	25.62 (6.75)	5.5 (28.8)	29.46	79.2	37.9	0.167	99.9	0.81
1.24	8567	99.9 (99.7)	23.09 (4.75)	6.2 (42.1)	32.31	79.2	37.9	0.172	99.9	0.68

1.55	8587	99.9 (99.7)	19.52 (2.58)	7.6 (77.8)	36.87	79.3	37.9	0.187	99.9	0.51
1.86	8594	99.9 (99.7)	14.05 (0.88)	11.8 (231.9)	44.94	79.4	38.0	0.226	99.9	0.32
2.17	8425	97.4 (91.6)	5.88 (-)	41.9 (-)	58.71	79.5	38.0	0.477	99.1	0.18

Crystal 12 (No uridine)

Dose (MGy)	Unique reflections	Complete-ness (%)	<I>/σ(I)	R-meas (%)	B-factor (Å2)	a = b (Å)	c (Å)	Mosaicity (deg)	CC1/2	I_n / I_0
0.36§	8586	99.9 (99.8)	16.76 (14.14)	5.9 (7.6)	21.52	79.3	37.9	0.035	99.4	1.00
0.72#	8579	99.8 (99.7)	21.96 (17.77)	5.0 (9.3)	26.80	79.3	37.9	0.04	99.7	0.82
1.08*	8581	99.8 (99.7)	26.94 (8.71)	5.0 (26.2)	33.38	79.3	37.9	0.061	99.9	0.51
1.44	8566	99.8 (99.9)	13.67 (2.23)	12.4 (118.9)	37.27	79.3	37.8	0.148	99.8	0.27
1.8	8580	99.7 (99.3)	7.94 (1.21)	21.3 (216.0)	39.37	79.3	37.9	0.152	99.5	0.13

§ data set used for PDB ID 5L9J; # data set used for PDB ID 5LA5; * data set used for PDB ID 5LA8.

Crystal 13 (No uridine)

Dose (MGy)	Unique reflections	Complete-ness (%)	<I>/σ(I)	R-meas (%)	B-factor (Å2)	a = b (Å)	c (Å)	Mosaicity (deg)	CC1/2	I_n / I_0
0.36	8563	99.7 (99.6)	42.67 (34.65)	3.8 (5.2)	21.79	79.3	37.9	0.057	99.8	1.00
0.72	8507	99.0 (98.4)	46.17 (38.02)	3.5 (5.4)	25.99	79.3	37.9	0.06	99.8	0.88
1.08	8577	99.8 (100)	34.92 (14.45)	3.8 (15.2)	31.16	79.3	37.9	0.072	99.9	0.55
1.44	8586	99.8 (99.5)	24.7 (5.33)	6.4 (47.9)	33.53	79.3	37.9	0.132	99.9	0.34
1.8	8589	99.7 (99.0)	14.22 (2.09)	12.1 (110.7)	35.868	79.3	37.835	0.185	99.8	0.21

Crystal 14 (No uridine)

Dose (MGy)	Unique reflections	Complete-ness (%)	<I>/σ(I)	R-meas (%)	B-factor (Å2)	a = b (Å)	c (Å)	Mosaicity (deg)	CC1/2	I_n / I_0
0.36	8122	94.6 (92.1)	33.64 (29.71)	4.8 (6.2)	22.08	79.2	38.0	0.054	99.7	1.00
0.72	8159	94.9 (92.5)	33.86 (16.93)	3.9 (11.0)	28.14	79.3	37.9	0.067	99.9	0.78
1.08	8133	94.6 (92.1)	28.93 (6.55)	4.9 (34.2)	33.25	79.3	37.9	0.114	100	0.49
1.44	8089	94.0 (91.2)	15.13 (1.61)	12.2 (143.1)	37.57	79.3	37.9	0.257	99.8	0.28
1.8	8042	93.6 (91.8)	9.13 (0.7)	21.7 (291.2)	39.54	79.3	37.8	0.282	99.6	0.15

Crystal 15 (No uridine)

Dose (MGy)	Unique reflections	Complete-ness (%)	<I>/σ(I)	R-meas (%)	B-factor (Å2)	a = b (Å)	c (Å)	Mosaicity (deg)	CC1/2	I_n / I_0
0.36	8526	99.2 (99.4)	40.09 (35.26)	4.1 (4.8)	21.25	79.2	37.9	0.053	99.7	1.00
0.72	8570	99.7 (99.6)	37.71 (22.58)	3.6 (7.6)	26.86	79.3	37.9	0.057	99.9	0.80

1.08	8585	99.9 (99.8)	34.8 (12.87)	3.7 (16.6)	32.25	79.3	37.9	0.081	99.9	0.52
1.44	8569	99.8 (99.7)	24.81 (4.73)	6.5 (55.6)	35.50	79.3	37.9	0.152	99.9	0.29
1.8	8535	99.8 (99.6)	14.96 (1.86)	11.9 (127.7)	38.99	79.3	37.9	0.223	99.8	0.16

Crystal 16 (1M uridine)

Dose (MGy)	Unique reflections	Complete-ness (%)	<I>/σ(I)	R-meas (%)	B-factor (Å2)	a = b (Å)	c (Å)	Mosaicity (deg)	CC1/2	I_n / I_0
0.36§	8525	99.6 (99.7)	44.45 (26.75)	3.1 (6.1)	23.59	79.1	37.9	0.058	99.9	1.00
0.72#	8523	99.4 (98.8)	42.24 (23.52)	3.2 (6.8)	25.46	79.1	37.9	0.063	99.9	0.92
1.08*	8544	99.7 (99.9)	42.53 (20.74)	3.0 (8.0)	27.81	79.2	37.9	0.069	100	0.84
1.44	8547	99.7 (99.6)	41.21 (16.04)	3.1 (11.0)	30.68	79.2	37.9	0.082	100	0.71
1.8	8535	99.6 (99.7)	35.37 (8.90)	3.7 (22.1)	34.62	79.2	37.9	0.145	100	0.52
2.16	8518	99.5 (99.7)	24.99 (4.21)	6.0 (48.8)	36.82	79.2	37.9	0.243	99.9	0.36
2.52	8475	99.3 (98.6)	16.16 (2.15)	9.1 (91.4)	39.12	79.1	37.8	0.323	99.9	0.23
2.88	8477	99.6 (99.7)	10.5 (1.15)	14.4 (167.7)	40.38	79.0	37.8	0.427	99.7	0.16
3.24	8319	99.0 (98.9)	5.65 (0.85)	23.4 (261.7)	39.90	78.7	37.6	0.391	99.1	0.10

§ data set used for PDB ID 5LAF; # data set used for PDB ID 5LAG; * data set used for PDB ID 5LAN.

Crystal 17 (1M uridine)

Dose (MGy)	Unique reflections	Complete-ness (%)	<I>/σ(I)	R-meas (%)	B-factor (Å2)	a = b (Å)	c (Å)	Mosaicity (deg)	CC1/2	I_n / I_0
0.36	8539	99.7 (99.7)	39.0 (22.78)	3.5 (7.2)	23.71	79.0	38.0	0.052	99.9	1.00
0.72	8544	99.7 (99.8)	37.38 (20.56)	3.6 (8.2)	25.18	79.0	38.0	0.051	99.9	0.91
1.08	8565	99.9 (99.9)	36.06 (16.20)	3.6 (10.4)	28.10	79.1	37.9	0.06	99.9	0.83
1.44	8561	99.8 (99.8)	34.44 (12.04)	3.7 (14.7)	30.95	79.2	37.9	0.08	100	0.70
1.8	8548	99.8 (99.5)	29.91 (7.87)	4.3 (24.5)	33.06	79.2	37.9	0.11	100	0.55
2.16	8532	99.8 (100)	24.06 (4.68)	5.9 (45.1)	34.15	79.2	37.9	0.15	99.9	0.44
2.52	8566	99.7 (99.3)	18.78 (2.73)	8.6 (77.3)	34.694	79.203	37.884	0.166	99.9	0.37
2.88	8555	99.7 (99.0)	14.63 (1.78)	11.8 (118.1)	35.808	79.239	37.886	0.174	99.8	0.28
3.24	8557	99.7 (99.0)	10.56 (1.21)	16.9 (172.2)	36.823	79.302	37.904	0.183	99.7	0.21

Crystal 18 (1M uridine)

Dose (MGy)	Unique reflections	Complete-ness (%)	<I>/σ(I)	R-meas (%)	B-factor (Å2)	a = b (Å)	c (Å)	Mosaicity (deg)	CC1/2	I_n / I_0
0.36	8552	99.7 (99.9)	18.49 (14.2)	4.9 (7.8)	22.22	79.1	37.9	0.032	99.6	1.00
0.72	8543	99.6 (99.7)	38.58 (21.32)	3.4 (8.3)	24.91	79.2	37.9	0.039	99.9	0.95
1.08	8557	99.7 (99.9)	36.47 (16.96)	3.5 (10.0)	27.52	79.2	37.9	0.054	99.9	0.88

1.44	8567	99.7 (99.3)	34.25 (11.97)	3.8 (16.3)	30.65	79.2	37.9	0.078	100	0.76
1.8	8549	99.7 (99.6)	28.13 (6.68)	5.0 (33.4)	33.66	79.2	37.9	0.13	99.9	0.60
2.16	8538	99.6 (99.3)	19.29 (3.03)	8.3 (75.9)	36.16	79.2	37.9	0.18	99.9	0.46
2.52	8550	99.6 (99.3)	13.36 (1.80)	13.4 (131.1)	37.37	79.2	37.9	0.213	99.8	0.35
2.88	8533	99.3 (98.1)	9.86 (1.19)	19.7 (200.1)	38.60	79.2	37.9	0.224	99.5	0.26
3.24	8565	99.3 (98.0)	7.56 (0.86)	26.0 (280.0)	39.29	79.2	37.9	0.213	99.2	0.19

Supporting Table 6 | *Data collection statistics for all crystals collected at 100 K extracted from the initial integration by XDS. Resolution range is 50-1.7 Å. Space group for all crystals is $P4_32_12$.*

Crystal 18 (No uridine)

Dose (MGy)	Unique reflections	Complete-ness (%)	<I>/σ(I) [A2][JJ3]	R-meas (%)	B-factor (Å^2)	a = b (Å)	c (Å)	Mosaicity (deg)	CC1/2	In / I0
1.61	13288	99.7 (99.6)	66.15 (36.44)	2.1 (4.3)	17.43	78.8	37.0 [A4]	0.181	100.0	1.00
45.93	13366	99.6 (99.2)	50.85 (21.29)	2.5 (7.5)	21.94	79.0	37.1 [JJ5]	0.174	100.0	0.66
101.33	13415	99.6 (99.5)	27.6 (6.05)	4.1 (27.1)	29.33	79.0	37.1	0.189	99.9	0.37
145.65	13345	99.5 (99.3)	17.96 (2.21)	5.8 (79.9)	34.70	79.1	37.1	0.209	99.9	0.23

Crystal 19 (No uridine)

Dose (MGy)	Unique reflections	Complete-ness (%)	<I>/σ(I)	R-meas (%)	B-factor (Å^2)	a = b (Å)	c (Å)	Mosaicity (deg)	CC1/2	In / I0
1.61	12646	95.0 (97.1)	72.99 (39.44)	1.9 (3.9)	17.84	78.7	37.0	0.156	100.0	1.00
45.93	12695	95.0 (97.5)	56.91 (20.03)	2.1 (7.8)	22.65	78.9	37.1	0.181	100.0	0.69
101.33	12579	94.5 (95.7)	28.53 (4.85)	3.8 (33.1)	30.56	78.8	37.1	0.245	100.0	0.40
145.65	12473	94.3 (95.4)	17.75 (1.86)	5.8 (89.7)	34.57	78.7	37.1	0.297	99.9	0.25

Crystal 20 (No uridine)

Dose (MGy)	Unique reflections	Complete-ness (%)	<I>/σ(I)	R-meas (%)	B-factor (Å^2)	a = b (Å)	c (Å)	Mosaicity (deg)	CC1/2	In / I0
1.61	13255	99.7 (99.3)	59.78 (36.77)	2.5 (4.3)	16.36	78.8	37.0	0.113	99.9	1.00
45.93	13379	99.8 (99.9)	55.62 (19.44)	2.2 (8.8)	21.13	79.0	37.1	0.134	100.0	0.74
101.33	13386	99.7 (99.7)	34.49 (4.38)	3.7 (39.5)	28.74	79.1	37.1	0.164	100.0	0.44
145.65	13417	99.5 (98.5)	23.60 (1.59)	5.5 (124.9)	34.43	79.2	37.1	0.188	100.0	0.28

Crystal 21 (500mM uridine)

Dose (MGy)	Unique reflections	Complete-ness (%)	<I>/σ(I)	R-meas (%)	B-factor (Å^2)	a = b (Å)	c (Å)	Mosaicity (deg)	CC1/2	In / I0
1.61	13265	99.7 (99.0)	48.02 (34.84)	3.4 (4.6)	16.96	78.7	37.0	0.126	99.9	1.00
45.93	13395	99.8 (99.6)	47.64 (19.92)	2.8 (8.2)	21.94	78.9	37.1	0.137	100.0	0.75
101.33	13423	99.8 (99.1)	30.83 (4.36)	3.9 (45.3)	30.44	79.1	37.2	0.172	100.0	0.45
145.65	13570	99.8 (99.3)	19.36 (1.19)	5.9 (165.1)	37.33	79.2	37.2	0.176	100.0	0.29

Crystal 22 (1M uridine)

Dose (MGy)	Unique reflections	Complete-ness (%)	<I>/σ(I)	R-meas (%)	B-factor (Å^2)	a = b (Å)	c (Å)	Mosaicity (deg)	CC1/2	In / I0
1.61	13070	99.6 (99.6)	48.60 (15.04)	2.7 (11.6)	22.17	78.2	37.1	0.314	100.0	1.00
45.93	13200	99.7 (99.6)	40.05 (8.28)	3.1 (22.2)	26.85	78.5	37.2	0.308	100.0	0.66
101.33	13323	99.7 (99.6)	24.45 (2.01)	4.6 (98.1)	35.37	78.7	37.3	0.298	100.0	0.36
145.65	13379	99.5 (98.1)	16.93 (0.46)	6.6 (445.7)	43.58	78.7	37.3	0.335	100.0	0.22

Crystal 23 (1M uridine)

Dose (MGy)	Unique reflections	Complete-ness (%)	<I>/σ(I)	R-meas (%)	B-factor (Å^2)	a = b (Å)	c (Å)	Mosaicity (deg)	CC1/2	In / I0
1.61	13251	99.7 (99.8)	50.96 (27.63)	2.8 (5.9)	20.05	78.6	37.0	0.113	99.9	1.00
45.93	13339	99.7 (99.9)	42.13 (16.32)	3.1 (10.4)	24.88	78.8	37.1	0.107	99.9	0.67
101.33	13378	99.7 (99.6)	30.16 (4.63)	3.7 (41.1)	32.73	79.0	37.2	0.116	100.0	0.40
145.65	13373	99.5 (99.2)	21.78 (1.32)	4.9 (152.1)	39.18	79.0	37.2	0.136	99.9	0.27

Crystal 24 (1M uridine)

Dose (MGy)	Unique reflections	Complete-ness (%)	<I>/σ(I)	R-meas (%)	B-factor (Å^2)	a = b (Å)	c (Å)	Mosaicity (deg)	CC1/2	In / I0
1.61	13247	99.7 (99.0)	70.14 (34.77)	1.9 (4.6)	19.53	78.6	37.0	0.145	100.0	1.00
45.93	13338	99.7 (99.6)	58.05 (19.75)	2.2 (8.5)	23.84	78.8	37.2	0.140	100.0	0.71
101.33	13341	99.7 (99.1)	34.15 (4.88)	3.3 (38.1)	31.17	78.9	37.2	0.167	100.0	0.43
145.65	13340	99.7 (99.1)	22.12 (1.61)	4.9 (121.2)	36.66	78.9	37.2	0.195	100.0	0.28

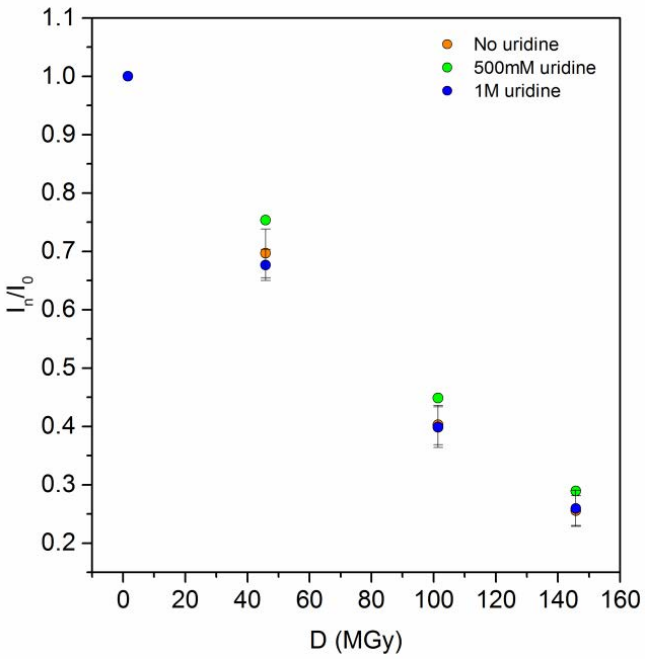

Supporting Figure 35 | *Decay of the mean normalized intensity (I/I_0) with absorbed dose on lysozyme crystals at 100 K without uridine in the solution (orange, crystals 18-20), with 500 mM uridine (green, crystal 21) and with 1 M uridine (blue, crystals 22-24). I/I_0 is calculated in the 50-1.7 Å resolution range.*

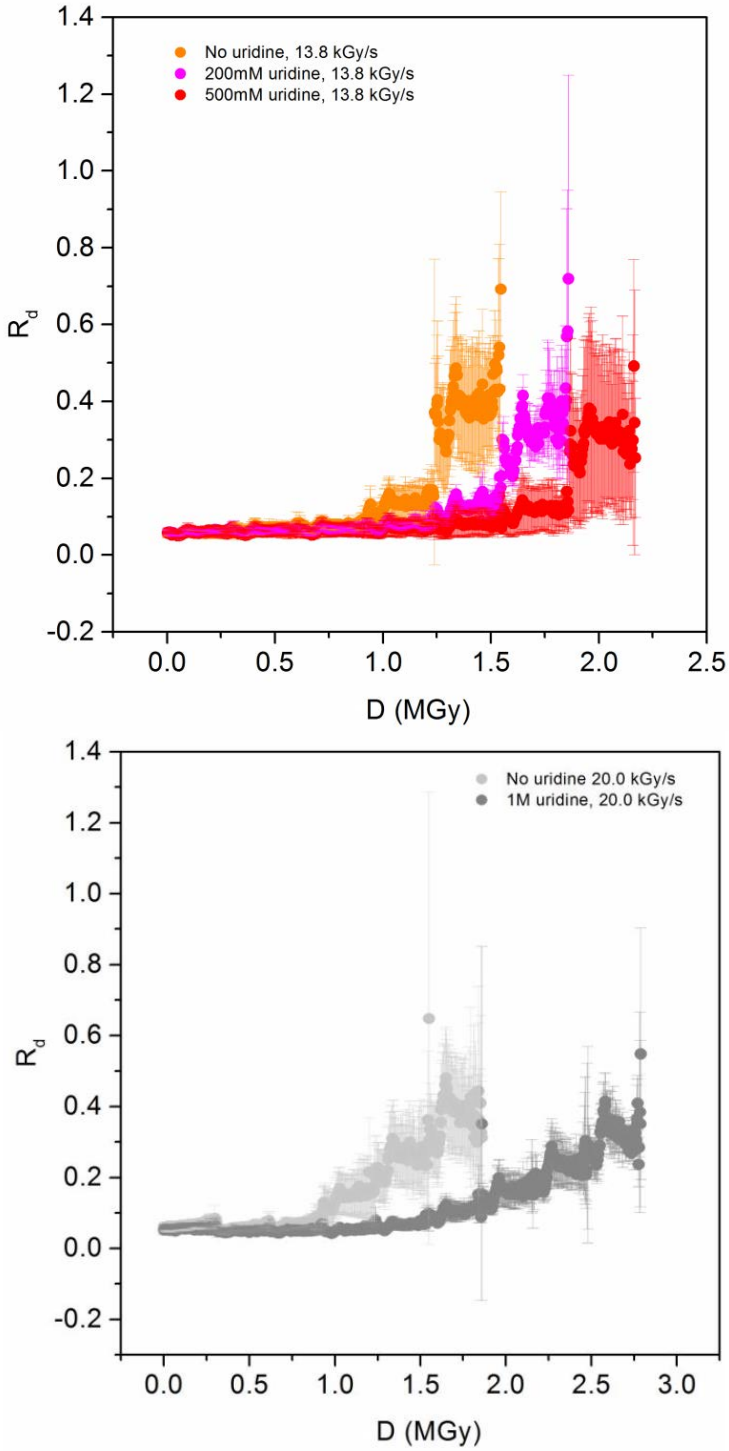

Supporting Figure 36 | *Evolution of the [A6][JJ7]damage R-factor (R_d) as a function of dose for native lysozyme crystals and lysozyme crystals soaked in different concentrations of uridine (200mM, 500mM and 1M). (a) Data collected at 13.8 kGy s^{-1} and (b) data collected at 20.0 kGy s^{-1}. R_d is calculated in the resolution range 50-2 Å. Each point in the plot is the mean obtained by 3 or 4 independent measures from different crystals. The associated error bar to each point shows the standard deviation of the mean.*

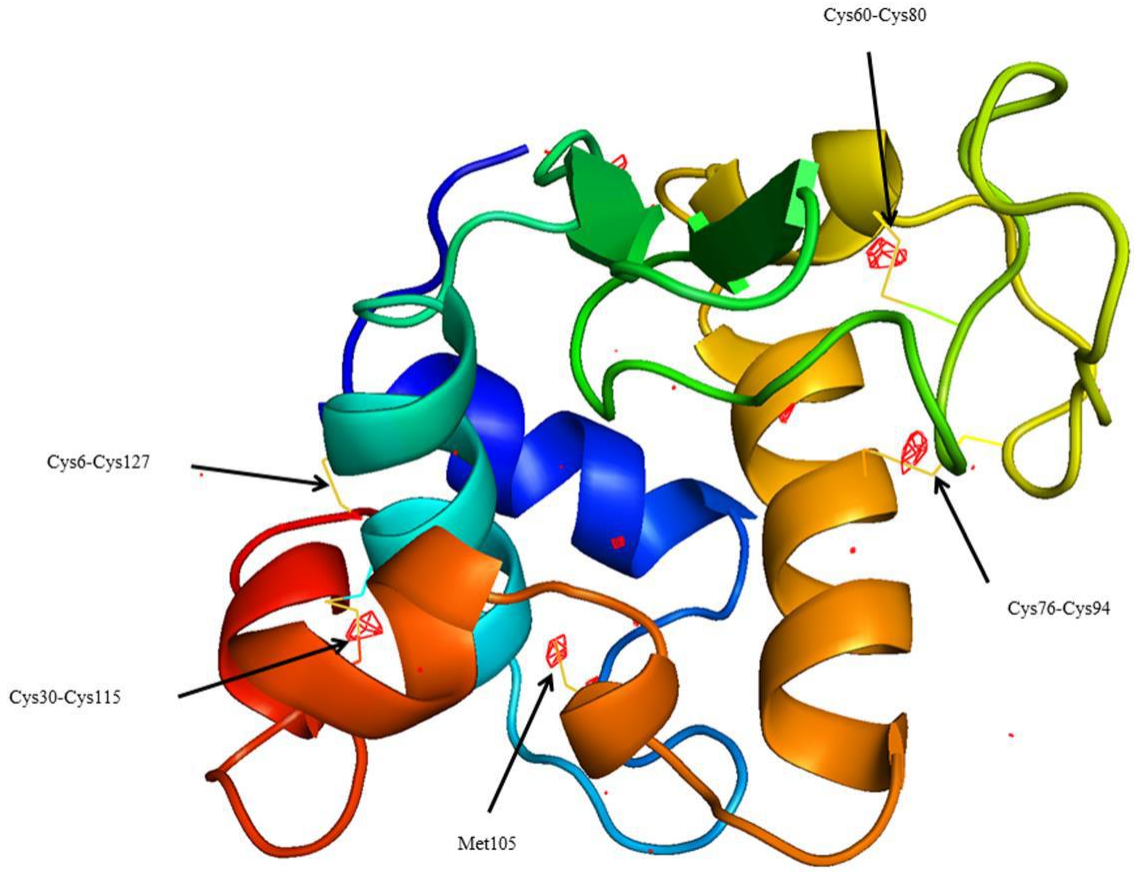

Supporting Figure 37 | *($F_{obs,3}$ - $F_{obs,1}$, $\alpha_{calc,1}$) map of a crystal with 1 M of uridine at room temperature (crystal 16 from table S2) contoured at -4σ. The arrows point to the four disulphide bonds and to Met105.Only four relevant peaks are observed in Cys30-Cys115, Cys76-Cys94, Cys64-Cys80 and Met105. At -5σ no significant peaks are observed.*

Supporting information: Expanding the small angle scattering experiments to low-molecular weight and low-concentration protein samples

Supporting Table 7 | *Frames where the critical doses were reached and their corresponding scavenging factors. All the tabulated frames arise from the intersection between a 4th order interpolation polynomial and the threshold conditions in which the critical doses are defined. The number of frames in parenthesis correspond to the second set of seven consecutive data frames with* $\boldsymbol{C = 17}$.

Sample	Frames			Scavenging factors		
[Lyz] = 7.00 mg/ml	$Rg/Rg_0 = 1.05$	$I(0)/I(0)_0 = 1.05$	CorMap test	$Rg/Rg_0 = 1.05$	$I(0)/I(0)_0 = 1.05$	CorMap test
Control	11	11	11	1	1	1
100 mM glycerol	25	29	18	2.27	2.64	1.64
678 mM glycerol	50	50	51	4.55	4.55	4.64
25 mM 5-methy uridine	118	77	70	10.73	7.00	6.36
50 mM 5-methyl uridine	132	112	63	12.00	10.18	5.73
100 mM 5-methyl uridine	225	177	97	20.45	16.09	8.82
25 mM cytidine	108	82	73	9.82	7.45	6.64
50 mM cytidine	127	126	139	11.55	11.45	12.64
100 mM cytidine	223	217	178	20.27	19.73	16.18
25 mM cytosine	79	84	72	7.18	7.64	6.55
50 mM cytosine	79	98	139	7.18	8.91	12.64
100 mM cytosine	198	202	177	18.00	18.36	16.09
25 mM uridine	89	66	50	8.09	6.00	4.55
50 mM uridine	115	97	54	10.45	8.82	4.91
100 mM uridine	174	136	42 (117)	15.82	12.36	3.82 (10.63)

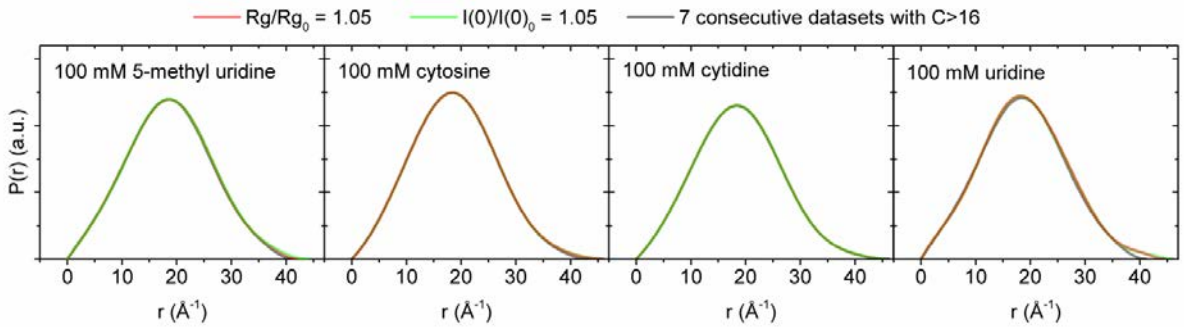

Supporting Figure 38 | *Pair distribution functions are independent of the used metric and the used additive. Pair distribution functions, P(r), for those samples containing 5-metrhyl uridine, cytosine, cytidine and uridine at 100 mM. For each sample, all frames below the three defined critical doses were considered.*

Supporting Table 8 | *Structural parameters calculated from the pair distribution function in Supporting Figure 38.*

Parameters	100 mM 5-methyl uridine		
	CorMap	$Rg/Rg_0 = 1.05$	$I(0)/I(0)_0 = 1.05$
# frames	97	225	117
R_g (nm)	14.28	14.38	14.46
I(0) (a.u.)	0.30	0.30	0.30
V_p	22900	22500	22800
D_{max} (nm)	41.33	42.46	43.98

Parameters	100 mM cytidine		
	CorMap	$Rg/Rg_0 = 1.05$	$I(0)/I(0)_0 = 1.05$
# frames	178	223	217
R_g (nm)	14.29	14.41	14.43
I(0) (a.u.)	0.31	0.31	0.31
V_p	22300	22200	22200
D_{max} (nm)	43.36	46.07	45.78

Parameters	100 mM cytosine		
	CorMap	$Rg/Rg_0 = 1.05$	$I(0)/I(0)_0 = 1.05$
# frames	177	198	202
R_g (nm)	14.34	14.35	14.36
I(0) (a.u.)	0.29	0.29	0.29
V_p	22200	22100	22100
D_{max} (nm)	46.24	45.80	45.75

Parameters	100 mM uridine		
	CorMap	$Rg/Rg_0 = 1.05$	$I(0)/I(0)_0 = 1.05$
# frames	42	174	136
R_g (nm)	14.23	14.48	14.51
I(0) (a.u.)	0.30	0.31	0.31
V_p	22800	23200	23000
D_{max} (nm)	41.16	44.48	46.14

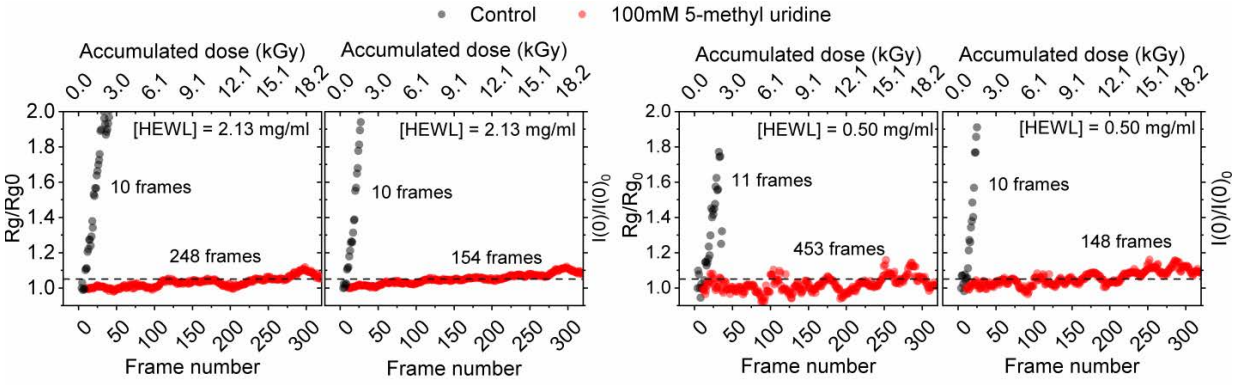

Supporting Figure 39 | *The addition of 100 mM 5-methyl uridine reduces the radiation damage in HEWL solutions at 2.13 and 0.50 mg/ml. The scavenging effect is monitored though the increase of the radius of gyration,* $\boldsymbol{Rg/Rg_0}$*, and the normalized intensity at zero,* $\boldsymbol{I(0)/I(0)_0}$*, as a function of the accumulated dose and frame number. Dashed lines represents the limits where* $\boldsymbol{Rg/Rg0 = 1.05}$ *and* $\boldsymbol{I(0)/I(0)_0 = 1.05}$*. Buffer conditions for all samples: 40 mM sodium acetate (pH 3.8), 150 mM sodium chloride and 0 or 100 mM 5-methyl uridine.*

Supporting Table 9 | *Frames where the critical doses were reached in the Supporting Figure 39. All the tabulated frames arise from the intersection between a 4th order interpolation polynomial and the threshold conditions in which the critical doses are defined.*

Sample [Lyz] = 2.13 mg/ml	Frames	
	$Rg/Rg_0 = 1.05$	$I(0)/I(0)_0 = 1.05$
Control	10	10
100 mM 5-methyl uridine	248	154

Sample [Lyz] = 0.50 mg/ml	Frames	
	$Rg/Rg_0 = 1.05$	$I(0)/I(0)_0 = 1.05$
Control	11	10
100 mM 5-methyl uridine	453	148

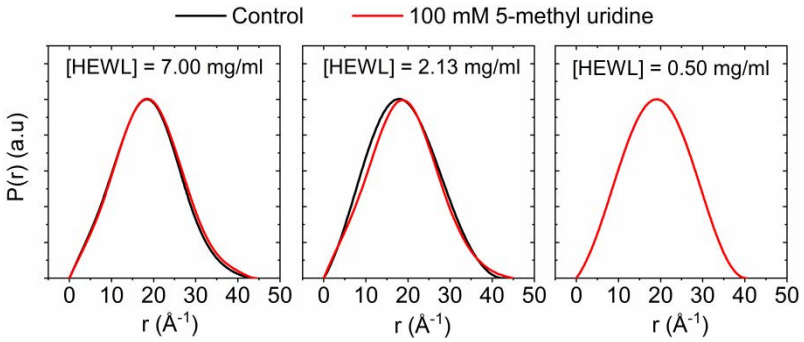

Supporting Figure 40 | *Pair distribution functions for HEWL samples at 0.5, 2.13 and 7.0 mg/ml.*

Supporting information: Enhanced Stability Against Radiation Damage of Lysozyme Crystals Grown in Fmoc-CF Hydrogels

Supporting Table 10 | *Data collection statistics of lysozyme crystals containing 0.5 wt% agarose (Aga_1, Aga_2 and Aga_3) and lysozyme crystals containing 2 wt% Fmoc-CF (Fmoc-CF_1, Fmoc-CF_2 and Fmoc-CF_3). For each crystal, the first and the 9th (dark background) datasets were processed in the* $\mathbf{40-1.7}$ *Å resolution range to analyze global damage and also for the calculation of Dn–D1 maps. Values in parentheses are for high resolution shell.*

Sample	**Aga_1**	**Aga_1**	**Aga_2**	**Aga_2**	**Aga_3**	**Aga_3**
Data set	D1	D9	D1	D9	D1	D9
Absorbed Dose (MGy)	0.03	0.29	0.03	0.29	0.03	0.29
Data Statistics						
Space Group	P 4_3 2_1 2	P 4_3 2_1 2	P 4_3 2_1 2	P 4_3 2_1 2	P 4_3 2_1 2	P 4_3 2_1 2
Unit cell (a=b, c) (Å)	79.18, 37.94	79.22, 37.94	79.15, 37.97	79.20, 37.98	79.20, 37.95	79.24, 37.97
I_n / I_1	1.00	0.47	1.00	0.42	1.00	0.62
Resolution range (Å)	39.59–1.70 (1.73–1.70)	39.61–1.70 (1.73–1.70)	39.57–1.70 (1.73–1.70)	39.60–1.70 (1.73–1.70)	37.95–1.70 (1.73–1.70)	37.97–1.70 (1.73–1.70)
Completeness (%)	99.6 (99.3)	99.8 (99.4)	99.5 (99.6)	99.8 (99.7)	98.3 (99.2)	98.8 (98.5)
Rmeas (%)	5.2 (7.9)	5.1 (32.0)	5.1 (8.2)	4.2 (39.8)	4.7 (8.1)	3.8 (38.1)
Total number of observations	83149 (4312)	87269 (4533)	84181 (4525)	87847 (4595)	83104 (4480)	87798 (4509)
<I/σ>	33.2 (21.5)	24.0 (5.9)	33.4 (21.0)	26.5 (5.2)	35.5 (22.9)	31.4 (6.1)
$CC_{1/2}$ (%)	99.6 (99.5)	99.8 (99.4)	99.6 (99.6)	99.9 (93.7)	99.7 (99.9)	99.9 (94.8)
Multiplicity	6.1 (5.9)	6.3 (6.2)	6.1 (6.2)	6.4 (6.3)	6.2 (6.2)	6.5 (6.3)
Mosaicity (°)	0.05	0.12	0.05	0.06	0.05	0.08

Sample	**Fmoc - CF_1**	**Fmoc - CF_1**	**Fmoc - CF_2**	**Fmoc - CF_2**	**Fmoc - CF_3**	**Fmoc - CF_3**
Data set	D1	D9	D1	D9	D1	D9
Absorbed Dose (MGy)	0.03	0.29	0.03	0.29	0.03	0.29
Data Statistics						
Space Group	P 4_3 2_1 2	P 4_3 2_1 2	P 4_3 2_1 2	P 4_3 2_1 2	P 4_3 2_1 2	P 4_3 2_1 2
Unit cell (a=b, c) (Å)	79.21, 38.00	79.25, 38.01	79.23, 38.00	79.29, 38.02	79.19, 37.96	79.22, 37.97
I_n / I_1	1.00	0.64	1.00	0.55	1.00	0.48
Resolution range (Å)	39.61–1.70 (1.73–1.70)	39.62–1.70 (1.73–1.70)	39.61–1.70 (1.73–1.70)	39.64–1.70 (1.73–1.70)	39.59–1.70 (1.73–1.70)	39.61–1.70 (1.73–1.70)
Completeness (%)	99.8 (99.8)	99.9 (99.6)	96.0 (96.3)	96.8 (96.4)	96.8 (97.0)	97.1 (96.9)
Rmeas (%)	4.3 (7.3)	3.7 (19.3)	4.0 (7.8)	3.9 (25.1)	4.3 (8.4)	4.2 (32.2)
Total number of observations	83297 (4411)	86947 (4609)	83793 (4220)	87517 (4429)	84624 (4421)	87629 (4509)
<I/σ>	39.0 (23.4)	35.8 (9.7)	40.1 (21.5)	30.7 (7.3)	38.5 (21.7)	28.7 (6.1)
$CC_{1/2}$ (%)	99.7 (99.7)	99.8 (98.6)	99.8 (99.6)	99.9 (96.5)	99.8 (99.6)	99.9 (95.5)
Multiplicity	6.0 (6.1)	6.3 (6.4)	6.3 (6.1)	6.6 (6.4)	6.4 (6.3)	6.6 (6.5)
Mosaicity (°)	0.07	0.07	0.08	0.09	0.06	0.07

Supporting Table 11 | *Data collection and refinement statistics of lysozyme crystals. For each crystal, the first dataset (D1) was used to calculate the phases employed subsequently for the calculation of Dn–D1 maps. Values in parentheses are for the high resolution data shell.*

Sample	**Aga_1**	**Aga_2**	**Aga_3**	**Fmoc-CF_1**	**Fmoc-CF_2**	**Fmoc-CF_3**
Data set	D1	D1	D1	D1	D1	D1
Absorbed Dose (MGy)	0.03	0.03	0.03	0.03	0.03	0.03
Data Statistics						
Space group	P 4_3 2_1 2	P 4_3 2_1 2	P 4_3 2_1 2	P 4_3 2_1 2	P 4_3 2_1 2	P 4_3 2_1 2
Unit cell (a=b, c) (Å)	79.18 37.94	79.13 37.97	79.19 37.94	79.20 37.99	79.21 37.98	79.18 37.95
Resolution (Å)	39.60-1.35 (1.37-1.35)	39.56-1.35 (1.37-1.35)	37.95-1.35 (1.37-1.35)	39.60-1.35 (1.37-1.35)	39.60-1.35 (1.37-1.35)	39.59-1.35 (1.37-1.35)
Completeness(%)	99.6 (97.1)	99.1 (93.2)	98.1 (95.8)	99.8 (99.0)	95.6 (86.7)	97.9 (98.2)
R_{meas} (%)	6.4 (33.6)	6.7 (22.8)	6.1 (25.1)	5.5 (26.9)	4.9 (18.3)	5.3 (35.4)
Total number of observations	161850 (6185)	152154 (5211)	153645 (5583)	154410 (5677)	141049 (4555)	160865 (6124)
$\langle I/\sigma \rangle$	22.1 (4.9)	22.6 (6.0)	23.3 (6.3)	25.7 (5.5)	27.0 (6.5)	24.0 (4.5)
$CC_{1/2}$ (%)	99.6 (93.9)	99.4 (96.2)	99.5 (96.5)	99.6 (95.7)	99.7 (97.5)	99.7 (92.9)
Multiplicity	6.0 (4.8)	5.7 (4.2)	5.8 (4.5)	5.7 (4.3)	5.5 (4.0)	6.1 (4.8)
Refinement						
R-work/R-free	0.144/0.174	0.144/0.173	0.148/0.181	0.142/0.170	0.144/0.179	0.137/0.166
B-factor (Å^2)	15.55	15.66	15.52	16.01	15.89	16.16
R.m.s. bond						
lengths (Å)	0.005	0.005	0.005	0.005	0.005	0.005
angles (°)	0.760	0.766	0.764	0.754	0.759	0.756
Ramachandran						
Outliers (%)	0	0	0	0	0	0
Allowed (%)	1.57	0.79	1.57	1.57	1.57	1.57
Favored (%)	98.43	99.21	98.43	98.43	98.43	98.43

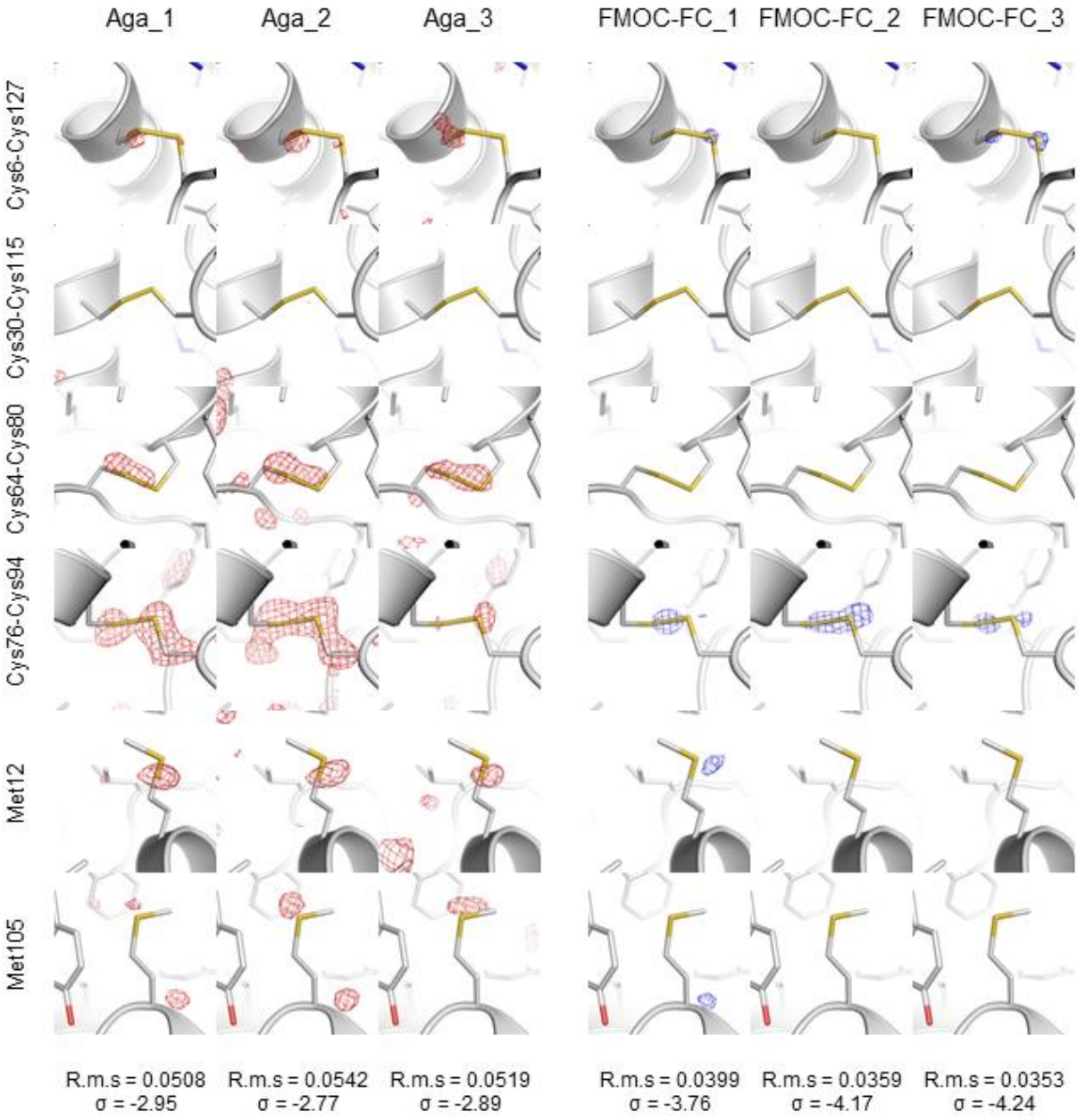

Supporting Figure 41 | *D9-D1 difference maps (blue for Fmoc-FC and red for agarose) over all disulfide bonds and methionines from the six measured lysozyme crystals. It is shown the significant local protection of lysozyme crystals grown in 2 wt% Fmoc-FC gel. All maps are contoured at 0.15 e/Å3 (Difference electron density = RMS × σ).*

Supporting information: Efficacy of aldose reductase inhibitors is affected by oxidative stress induced under X-ray irradiation

The results presented in this appendix are has been published in:

Scientific Reports. (2019). **9**:3177. DOI: 10.1038/s41598-019-39722-0

Authors: **Albert Castellví**,§ Isidro Crespo,§ Eva Crosas, Ana Cámara-Artigas, José A. Gavira, Miguel A. G. Aranda, Xavier Parés, Jaume Farrés and Judith Juanhuix.

§These authors contributed equally to this work.

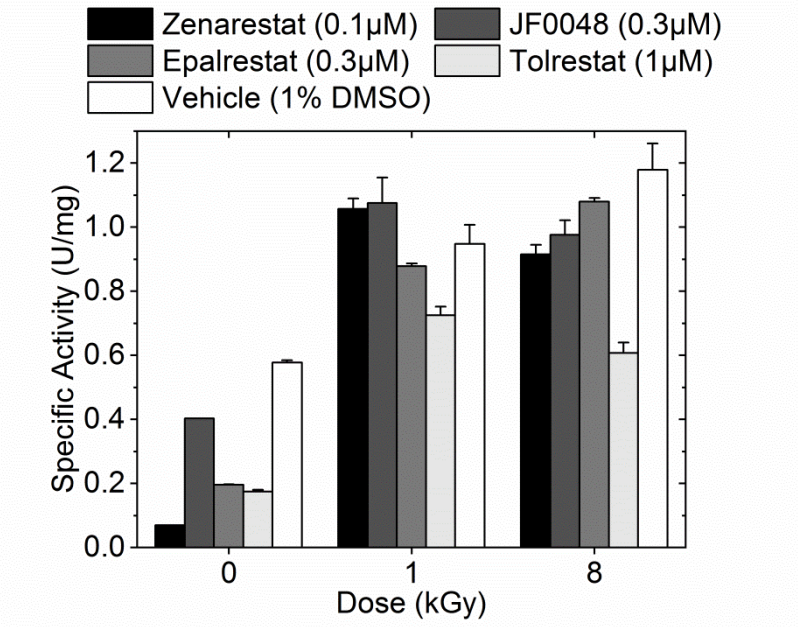

Supporting Figure 42 | *Specific activity of hAR in presence of the inhibitors at different absorbed doses. Control activities in presence of vehicle (1% DMSO) are also displayed. As described in Materials and Methods, the inhibitors were solubilized in DMSO and diluted in the reaction mixture to 1% (v/v). Note that the presence of DMSO alters the activities of the vehicle control, acting as inhibitor of the hAR in native form, that is, at zero dose [1]. The inhibitory effect of DMSO is not known for irradiated hAR. To remove the effect of DMSO in activity assays, which adds complexity to the analysis, we normalize the data in Figure 1b with respect to the vehicle control at every dose. The raw activities shown in this figure can not be compared to the normalized activities of Figures 1a and 1c in the main text, which were obtained from samples without DMSO.*

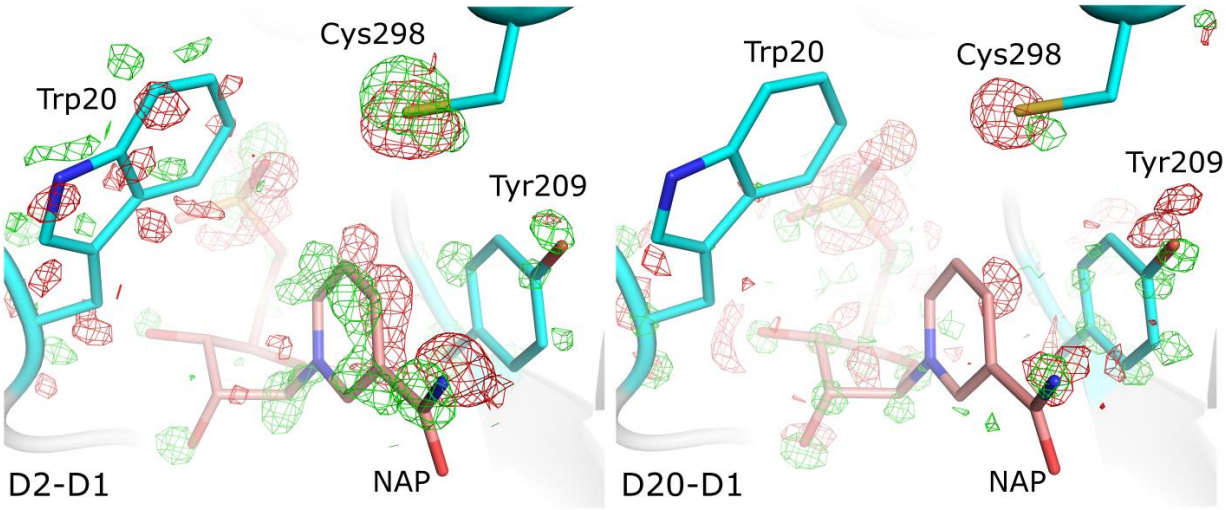

Supporting Figure 43 | *Radiation induces movements in the vicinity of Cys298. Difference Fourier maps D2-D1 (a) and D20-D1 (b) in the vicinity of Cys298, calculated as in Figure 2 of the article. The D2-D1 difference Fourier map reveals structural changes over $NADP^+$ (NAP), Trp20 and Cys298 (also slightly damaged), whereas the D20-D1 difference Fourier map reveals structural changes only over Tyr209. Both maps are contoured at $\sigma = \pm 3$.*

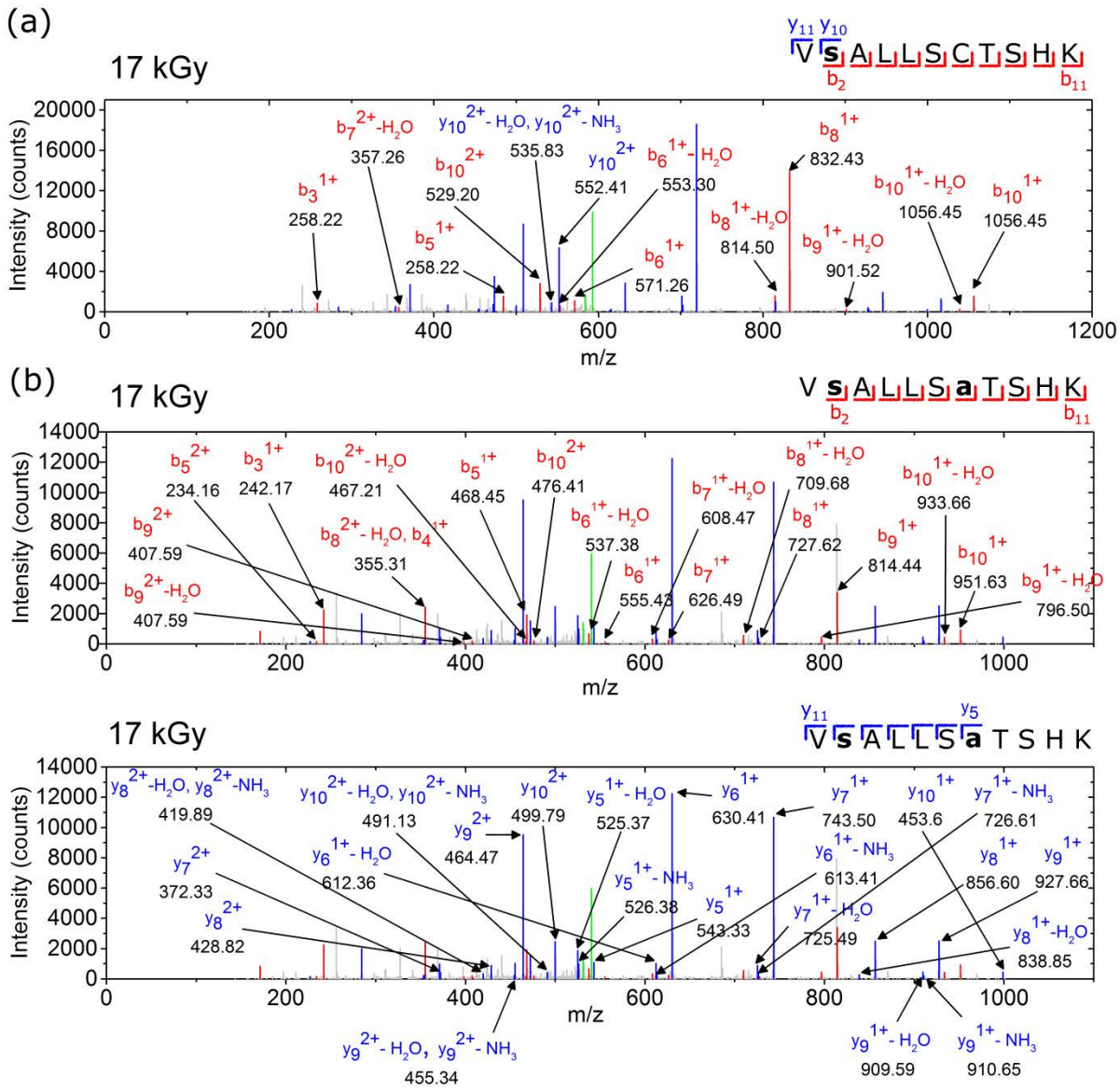

Supporting Figure 44 | *LC-MS/MS analysis at 17 kGy. Two modifications were observed at an absorbed dose of 17 kGy in different Cys298-containing peptides: (a) peptide with the single C298S modification and (b) peptide with C298 and C303A modifications. Characteristic peaks from the peptide fragmentation are colored in red (b_n), blue (y_n) and green (precursor), and labelled in separate plots in (b) for clarity. Non-characteristic peaks from the sequence are marked in grey. For clarity, only peaks that contain information about the peptide modifications are labeled. Only peaks above 1% of the base peak and a matching tolerance of 0.6 Da are represented.*

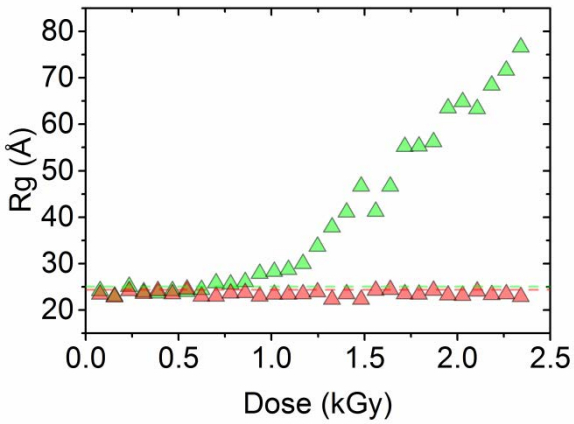

Supporting Figure 45 | *Uridine prevents global radiation damage of hAR in solution at radiation doses over 1 kGy. Evolution of the normalized radius of gyration R_g/R_{g0} of hAR in solution at a concentration of 2.3 mg/mL as a function of dose, as calculated in SAXS experiments performed in the beamline B21 at the Diamond Light Source. The hAR without any additive (green triangles) shows global radiation damage effects at absorbed doses above 1 kGy. The addition of 10 mM uridine to the hAR solution (red triangles) dramatically delays the global radiation damage to doses above 2.5 kGy. The dashed lines mark the initial radius of gyration incremented by 1 Å, above which the protein is considered damaged, unfolded or aggregated, according to Hopkins and Thorne[55] or Jeffries et al.[54].*

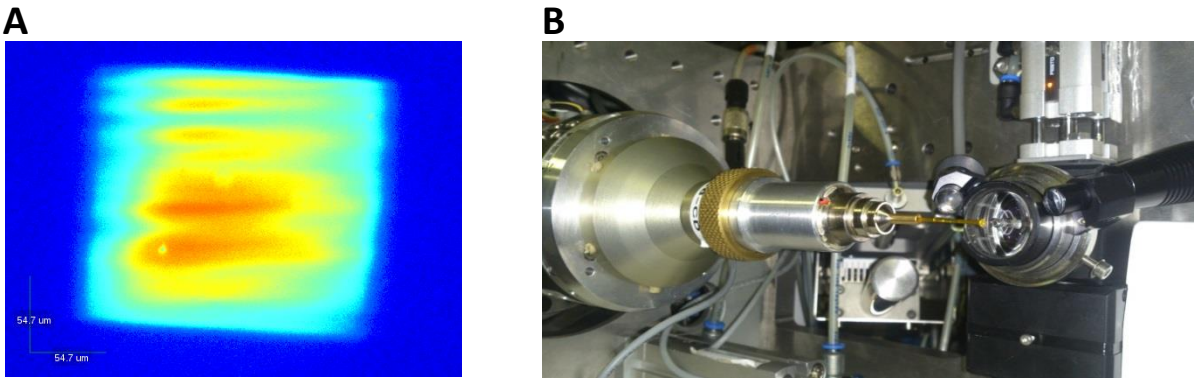

Supporting Figure 46 | *Homogeneous irradiation of hAR solution for enzymatic experiments. (a) Homogeneous irradiation of the hAR solution was achieved using a top-hat square-shaped beam (200×180 μm^2) as measured by a Ce:YAG fluorescence screen at the sample position, and scanning it through the axial section of the capillary. (b) The enzyme sample was inserted in a polyimide capillary and mounted in a SPINE magnetic base compatible with the goniometer available in the BL13-XALOC beamline at the ALBA synchrotron.*

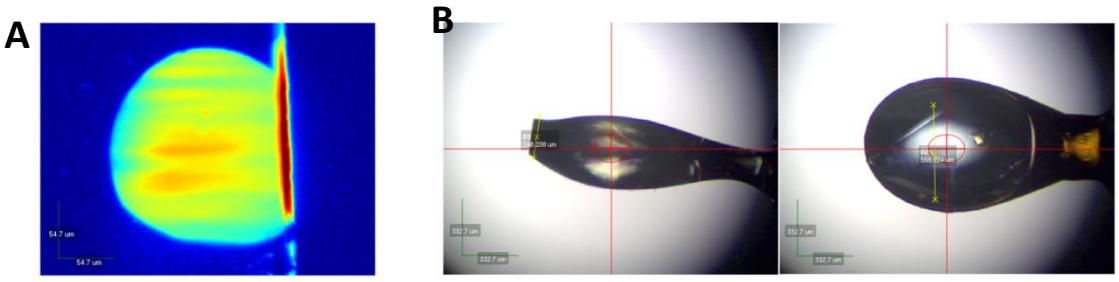

Supporting Figure 47 | *Homogeneous irradiation of the crystal in MX experiments. (a) The crystal was exposed to a top-hat, circular-shaped X-ray beam in the BL13-XALOC beamline at the ALBA Synchrotron. The beam was circular with 190 µm in diameter, as measured by a Ce:YAG fluorescence screen at the sample position. The circular beam spot appears to be cut in the right side due to the rim of the fluorescence screen used exclusively to measure the beam size. (b) The hAR crystal as aligned with the X-ray beam.*

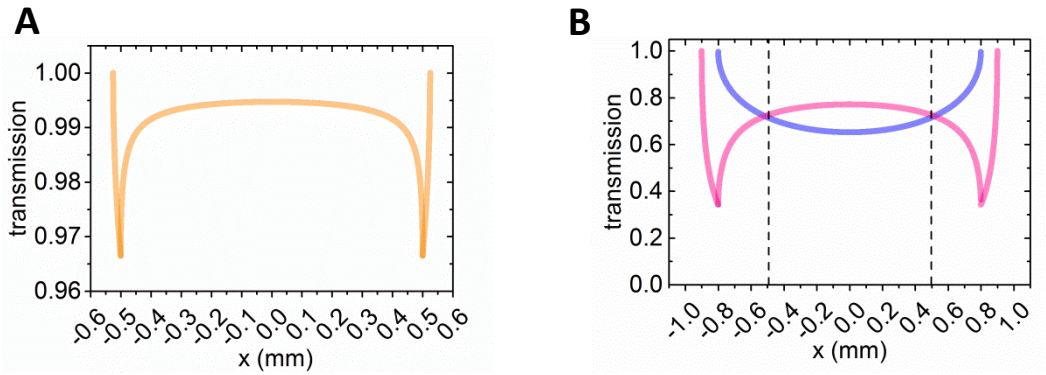

Supporting Figure 48 | *Calculated transmission coefficients. (a) Calculated transmission coefficient for the polyimide capillary (µ = 1.494 cm^2/g and ρ = 1.425 g/cm^3; R_{int} = 0.5 mm and R_{out} = 0.025 mm) used in the enzymatic experiments. (b) In pink: calculated transmission coefficient for a quartz capillary (µ = 9.804 cm^2/g and ρ = 2.648 g/cm^3; R_{int} = 0.8 mm and R_{ext} = 0.9 mm) used in SAXS experiments. In blue: calculated transmission coefficient for the sample (considered to be water: µ = 2.673 cm^2/g and ρ = 1 g/cm^3) used in SAXS experiments.*

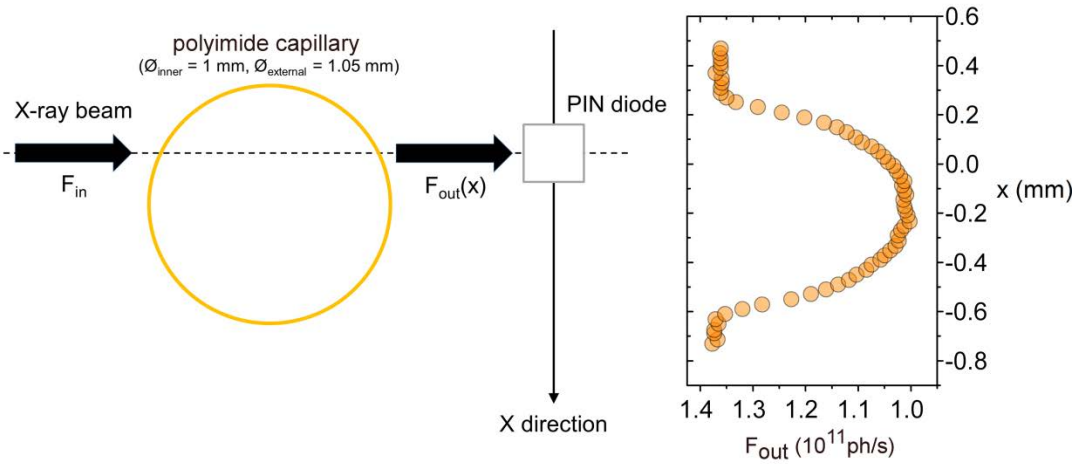

Supporting Figure 49 | *Experimentally measured absorption in irradiation experiments of enzyme samples in solution. The control sample was inserted in a polyimide capillary and irradiated using a top-hat circular-shaped beam (Supplementary Fig. 6). The beam was scanned vertically and the transmitted flux was measured using a PIN diode placed after the capillary. The value extracted experimentally is compatible with the calculated transmissions.*

Supporting Table 12 | *Data collection statistics for the MX experiments. Macromolecular crystallography data collection statistics for all datasets D1-D20. Spatial group for all datasets is $P2_1$; values in parenthesis refer to the highest resolution shell;* $R_{meas} = \sum_{hkl}\{N(hkl)/[N(hkl)-1]\}^{1/2} \times \sum_i |I_i(hkl) - \langle I(hkl)\rangle| / \sum_{hkl}\sum_i I_i(hkl)$.

Dataset	**D1**	**D2**	**D3**	**D4**	**D5**	**D6**	**D7**	**D8**	**D9**	**D10**
Dose (MGy)	0.03	0.21	0.39	0.57	0.75	0.93	1.11	1.29	1.47	1.65
Resolution (Å)	49.37-0.92 (0.94-0.92)	49.38-0.94 (0.96-0.94)	49.39-0.96 (0.98-0.96)	49.41-0.96 (0.98-0.96)	49.42-0.97 (0.99-0.97)	49.43-0.98 (1.00-0.98)	49.44-0.99 (1.01-0.99)	49.45-1.01 (1.03-1.01)	49.46-1.02 (1.04-1.02)	49.47-1.03 (1.05-1.03)
R_{meas}	0.038 (0.352)	0.037 (0.325)	0.038 (0.306)	0.039 (0.347)	0.039 (0.340)	0.040 (0.341)	0.041 (0.342)	0.041 (0.331)	0.042 (0.341)	0.043 (0.343)
Total number of observations	754031 (33632)	710512 (34066)	667577 (29233)	668072 (29091)	650322 (30432)	632865 (30825)	614656 (30107)	579058 (27350)	563270 (25865)	547873 (25354)
$\langle I/\sigma_I \rangle$	18.9 (3.6)	19.3 (4.0)	19.5 (4.1)	18.7 (3.7)	18.3 (3.9)	18.0 (3.9)	17.6 (3.9)	17.6 (4.1)	17.2 (3.9)	16.9 (4.0)
$CC_{1/2}$	0.999 (0.889)	0.999 (0.909)	0.999 (0.916)	0.999 (0.895)	0.999 (0.895)	0.999 (0.896)	0.999 (0.900)	0.999 (0.896)	0.999 (0.891)	0.999 (0.886)
Completeness (%)	99.5 (96.7)	99.6 (99.7)	99.5 (95.8)	99.5 (95.5)	99.7 (99.8)	99.7 (99.7)	99.7 (99.7)	99.7 (99.6)	99.7 (99.6)	99.7 (99.6)
Multiplicity	3.6 (3.3)	3.6 (3.5)	3.6 (3.3)	3.6 (3.3)	3.6 (3.4)	3.6 (3.6)	3.6 (3.6)	3.6 (3.5)	3.6 (3.4)	3.6 (3.4)
Mosaicity	0.12	0.12	0.12	0.12	0.13	0.13	0.13	0.13	0.13	0.13
Unit cell										
a (Å)	47.35	47.36	47.36	47.37	47.37	47.37	47.37	47.37	47.38	47.38
b (Å)	66.60	66.62	66.63	66.64	66.65	66.66	66.67	66.68	66.69	66.69
c (Å)	49.40	49.41	49.42	49.44	49.45	49.46	49.47	49.48	49.49	49.50
β (º)	92.05	92.05	92.03	92.03	92.02	92.02	92.02	92.02	92.01	92.01

Dataset	**D11**	**D12**	**D13**	**D14**	**D15**	**D16**	**D17**	**D18**	**D19**	**D20**
Dose (MGy)	1.83	2.01	2.19	2.37	2.55	2.73	2.91	3.09	3.27	3.45
Maximum resolution (Å)	49.48-1.04 (1.06-1.04)	49.49-1.06 (1.08-1.06)	49.50-1.07 (1.09-1.07)	49.50-1.08 (1.10-1.08)	49.51-1.09 (1.11-1.09)	49.52-1.11 (1.13-1.11)	49.53-1.12 (1.14-1.12)	49.54-1.13 (1.15-1.13)	49.55-1.15 (1.17-1.15)	49.55-1.17 (1.19-1.17)
R_{meas}	0.045 (0.347)	0.045 (0.317)	0.047 (0.322)	0.047 (0.327)	0.048 (0.341)	0.048 (0.327)	0.049 (0.334)	0.049 (0.312)	0.051 (0.333)	0.051 (0.335)
Total number of observations	532877 (24366)	504817 (24543)	489531 (21636)	476693 (20243)	464295 (19609)	442939 (21812)	431245 (21087)	416503 (18088)	398521 (19234)	379104 (18037)
$\langle I/\sigma_I \rangle$	16.5 (3.9)	16.6 (4.5)	16.3 (4.3)	15.9 (4.2)	15.6 (4.1)	15.7 (4.7)	15.4 (4.6)	15.4 (4.7)	15.1 (4.7)	15.2 (4.6)
$CC_{1/2}$	0.999 (0.889)	0.999 (0.898)	0.999 (0.900)	0.999 (0.902)	0.999 (0.892)	0.999 (0.899)	0.999 (0.898)	0.999 (0.909)	0.998 (0.905)	0.999 (0.905)
Completeness (%)	99.5 (95.9)	99.6 (99.5)	99.5 (95.8)	99.5 (95.7)	99.4 (94.9)	99.6 (99.4)	99.6 (99.5)	99.2 (91.3)	99.6 (99.3)	99.6 (99.5)
Multiplicity	3.6 (3.5)	3.6 (3.6)	3.6 (3.4)	3.6 (3.3)	3.6 (3.3)	3.7 (3.6)	3.7 (3.6)	3.7 (3.5)	3.7 (3.6)	3.7 (3.5)
Mosaicity	0.13	0.13	0.14	0.14	0.14	0.14	0.14	0.14	0.14	0.14
Unit cell										
a (Å)	47.38	47.38	47.38	47.38	47.38	47.38	47.38	47.38	47.38	47.38
b (Å)	66.70	66.71	66.71	66.72	66.73	66.74	66.74	66.75	66.76	66.77
c (Å)	49.51	49.51	49.52	49.53	49.54	49.55	49.55	49.56	49.57	49.58
β (º)	92.01	92.01	92.01	92.01	92.00	92.00	92.00	92.00	92.00	92.00

Supporting Table 13| *Refinement statistics for the MX experiments. Refinement statistics for datasets D1, D5, D10, D15 and D20. A random set of 5% of the reflections is selected to calculate* $\boldsymbol{R_{free}} = \sum_{hkl}||\boldsymbol{F_{obs}}(\boldsymbol{khl})| - |\boldsymbol{F_{calc}}(\boldsymbol{khl})|| / \sum_{hkl}|\boldsymbol{F_{obs}}(\boldsymbol{khl})|$; $\boldsymbol{R_{work}}$ *is calculated as for* $\boldsymbol{R_{free}}$ *considering the reflections not selected in the test set; the number of reflections considered was selected following the* $\boldsymbol{F_{obs}} > \boldsymbol{4\sigma}(\boldsymbol{F_{obs}})$ cutoff.

Refinement statistics

Dataset	**D1**	**D5**	**D10**	**D15**	**D20**
Dose (MGy)	0.03	0.75	1.65	2.55	3.45
PDB code	6F7R	6F81	6F82	6F84	6F8O
Resolution range (Å)	10 - 0.92	10 - 0.97	10 - 1.03	10 - 1.09	10 - 1.17
No. reflections all/free	177397/9549	153232/8104	127646/6716	107020/5563	86605/4591
R_{work}, R_{free}	0.104/0.131	0.108/0.135	0.110/0.139	0.120/0.152	0.119/0.163
Average B factor, all atoms (Å^2)	13.0	14.0	15.0	16.0	19.0
R.m.s. deviations					
Bond lengths (Å)	0.0158	0.0165	0.0164	0.0265	0.0178
Bond angles (°)	2.22	2.28	2.33	2.41	2.38
Ramachandran Plot					
Favoured (%)	97	98	98	98	99
Allowed (%)	3	2	2	2	1
Outliers (%)	0	0	0	0	0

Supporting Table 14 | *Alignment of the D20 dataset crystallographic structure versus the structures containing the various inhibitors. Root mean square deviations (RMSD), calculated for C_α atoms, main chains, side chains and all atoms, between the D20 dataset crystallographic structure and the structures with Zenarestat, Tolrestat, Epalrestat and JF0048 inhibitors. The structures were aligned using the whole structure excluding the disordered terminal residues (Ser2 to Phe311).*

		RMSD	
D20 (with C298) *vs.*		From Ser2 to Phe311	Cys298
Zenarestat (PDB 1IEI)	C_α atoms	0.695	0.225
	Main chain	0.722	1.718
	Side chain	1.529	0.427
	All	1.189	1.067
Tolrestat (PDB 1AH3)	C_α atoms	0.558	0.767
	Main chain	0.579	0.704
	Side chain	1.142	0.915
	All	0.893	0.808
Epalrestat (PDB 4JIR)	C_α atoms	0.459	0.079
	Main chain	0.470	0.103
	Side chain	0.871	0.182
	All	0.698	0.117
FJ0048 (PDB 4XZH)	C_α atoms	0.633	0.420
	Main chain	0.639	0.384
	Side chain	1.529	0.427
	All	0.989	0.751

Bibliografia

1. Garman, E. & Nave, C. Radiation damage to crystalline biological molecules: current view. *J. Synchrotron Radiat.* **9,** 327–328 (2002).

2. Garman, E. F. & Weik, M. X-ray radiation damage to biological macromolecules: Further insights. *J. Synchrotron Radiat.* **24,** 1–6 (2017).

3. Garman, E. F. & Weik, M. Radiation damage to macromolecules: kill or cure? *J. Synchrotron Radiat.* **22,** 195–200 (2015).

4. Garman, E. F. & Weik, M. Radiation damage to biological macromolecules: some answers and more questions. *J. Synchrotron Radiat.* **20,** 1–6 (2013).

5. Garman, E. F. & Nave, C. Radiation damage in protein crystals examined under various conditions by different methods. *J. Synchrotron Radiat.* **16,** 129–132 (2009).

6. Carman, E. F. & McSweeney, S. M. Progress in research into radiation damage in cryo-cooled macromolecular crystals. *J. Synchrotron Radiat.* **14,** 1–3 (2007).

7. Zeldin, O. B., Gerstel, M. & Garman, E. F. *RADDOSE-3D* : time- and space-resolved modelling of dose in macromolecular crystallography. *J. Appl. Crystallogr.* **46,** 1225–1230 (2013).

8. Berger, M. J. *et al.* XCOM: Photon Cross Sections Database. (2010). doi:10.18434/T48G6X

9. Thompson, A. C. *X-ray Data Booklet*. (Lawrence Berkeley National Laboratory, University of California, 2001).

10. Garman, E. F. Radiation damage in macromolecular crystallography : what is it and why should we care ? *Acta Crystallogr. Sect. D* **66,** 339–351 (2010).

11. Nass, K. Radiation damage in protein crystallography at X-ray free-electron lasers. *Acta Crystallogr. Sect. D Struct. Biol.* **75,** 211–218 (2019).

12. Krause, M. O. & Oliver, J. H. Natural Widths of Atomic K and L Levels, KAlpha X'ray Lines and Several KLL Auger Lines. *J. Chem. Phys. Ref. Data* **8,** 329–337 (1979).

13. Carl Caleman *et al.* On the feasibility of nanocrystal imaging using intense and ultrashort x-ray pulses. *ACS Nano* **5,** 139–146 (2011).

14. Neutzo, R., Wouts, R., Van Der Spoel, D., Weckert, E. & Hajdu, J. Potential for biomolecular imaging with femtosecond X-ray pulses. *Nature* **406,** 752–757 (2000).

15. Chapman, H. N., Caleman, C., Timneanu, N. & Chapman, H. N. Diffraction before destruction. (2014).

16. Sanishvili, R. *et al.* Radiation damage in protein crystals is reduced with a micron-sized X-ray beam. *PNAS* **108,** 6127–6132 (2011).

17. Chapman, H. N. *et al.* Femtosecond X-ray protein nanocrystallography. 3–8 (2011). doi:10.1038/nature09750

18. Berglund, G. I. *et al.* The catalytic pathway of horseradish peroxidase at high resolution. *Nature* **417,** 463–468 (2002).

19. Graceffa, R. *et al.* Sub-millisecond time-resolved SAXS using a continuous-flow mixer and X-ray microbeam. 820–825 (2013). doi:10.1107/S0909049513021833

20. De La Mora, E., Carmichael, I. & Garman, E. F. Effective scavenging at cryotemperatures: Further increasing the dose tolerance of protein crystals. *J. Synchrotron Radiat.* **18,** 346–357 (2011).

21. Jones, G. D., Lea, J. S., Symons, M. C. & Taiwo, F. A. Structure and mobility of electron gain and loss centres in proteins. *Nature* **330,** 772–773 (1987).

22. Symons, M. C. R. Mechanism of radiation damage to proteins and DNA - An EPR perspective. *Prog. React. Kinet. Mech.* **24,** 139–164 (1999).

23. Zakurdaeva, O. A., Nesterov, S. V. & Feldman, V. I. Radiolysis of aqueous solutions of poly(ethylene oxide) at 77 K. *High Energy Chem.* **39,** 201–206 (2005).

24. Carpentier, P., Royant, A., Weik, M. & Bourgeois, D. Ways & Means Raman-Assisted

Crystallography Suggests a Mechanism of X-Ray-Induced Disulfide Radical Formation and Reparation. *Struct. Des.* **18,** 1410–1419 (2010).

25. Sutton, K. A. *et al.* Insights into the mechanism of X-ray-induced disulfide-bond cleavage in lysozyme crystals based on EPR, optical absorption and X-ray diffraction studies. *Acta Crystallogr. Sect. D Biol. Crystallogr.* **69,** 2381–2394 (2013).

26. Ravelli, R. B. G. & McSweeney, S. M. . The 'fingerprint' that X-rays can leave on structures. *Structure* **8,** 315–328 (2000).

27. Sevilla, M. D., D'Arcy, J. B. & Morehouse, K. M. An electron spin resonance study of .gamma.-irradiated frozen aqueous solutions containing dipeptides. Mechanisms of radical reaction. *J. Phys. Chem.* **83,** 2887–2892 (1979).

28. Filali-Mouhim, A. *et al.* Lysozyme fragmentation induced by gamma-radiolysis. *Int. J. Radiat. Biol.* **72,** 63–70 (1997).

29. Kohan, L. M. *et al.* Self-radiolysis of tritiated water. 1. A comparison of the effects of 60Co γ-rays and tritium β-particles on water and aqueous solutions at room temperature. *RSC Adv.* **3,** 19282–19299 (2013).

30. Mustaree, S. *et al.* Self-radiolysis of tritiated water. 3. the OH scavenging effect of bromide ions on the yield of H2O2 in the radiolysis of water by 60Co γ-rays and tritium β-particles at room temperature. *RSC Adv.* **4,** 43572–43581 (2014).

31. Buxton, G. V, Greenstock, C. L., Helman, W. P. & Ross, A. B. Critical Review of rate constants for reactions of hydrated electrons, hydrogen atoms and hydroxyl radicals in aqueous solution. *Journal of Physical and Chemical Reference Data* **17,** 513 (1988).

32. Yamaguchi, H., Uchihori, Y., Yasuda, N., Takada, M. & Kitamura, H. Estimation of yields of OH radicals in water irradiated by ionizing radiation. *J. Radiat. Res.* **46,** 333–341 (2005).

33. Watanabe, R. & Saito, K. Monte Carlo simulation of water radiolysis in oxygenated condition for monoenergetic electrons from 100eV to 1MeV. *Radiat. Phys. Chem.* **62,** 217–228 (2001).

34. O'Leary, M. *et al.* Observation of dose-rate dependence in a Fricke dosimeter irradiated at low dose rates with monoenergetic X-rays. *Sci. Rep.* **8,** 2–10 (2018).

35. Dealmeida, C. E. *et al.* A feasibility study of Fricke dosimetry as an absorbed dose to water standard for192Ir HDR sources. *PLoS One* **9,** 1–13 (2014).

36. Head, D. & Walker, D. C. Nitrous oxide as a scavenger in the radiolysis of water. *Nature* **207,** 517–518 (1965).

37. Ingelman-Sundberg, M. & Johansson, I. Mechanisms of hydroxyl radical formation and ethanol oxidation by ethanol-inducible and other forms of rabbit liver microsomal cytochromes P-450. *J. Biol. Chem.* **259,** 6447–6458 (1984).

38. Kmetko, J., Warkentin, M., Englich, U. & Thorne, R. E. Can radiation damage to protein crystals be reduced using small-molecule compounds? *Acta Crystallogr. D. Biol. Crystallogr.* **67,** 881–893 (2011).

39. Kiselar, J. G., Maleknia, S. D., Sullivan, M., Downard, K. M. & Chance, M. R. Hydroxyl radical probe of protein surfaces using synchrotron X-ray radiolysis and mass spectrometry. **78,** (2002).

40. Frankel, L. K. *et al.* Radiolytic Mapping of Solvent-Contact Surfaces in Photosystem II of Higher Plants. **288,** 23565–23572 (2013).

41. Xu, G. & Chance, M. R. Hydroxyl Radical-Mediated Modification of Proteins as Probes for Structural Proteomics. *Chem. Rev.* **107,** 3514–3543 (2007).

42. Gupta, S., Feng, J., Chan, L. J. G., Petzold, C. J. & Ralston, C. Y. Synchrotron X-ray footprinting as a method to visualize water in proteins. *J. Synchrotron Radiat.* **23,** 1056–1069 (2016).

43. Wang, J. X-ray radiation-induced addition of oxygen atoms to protein residues. *Protein Sci.* **25,** 1407–1419 (2016).

44. Xu, X. *et al.* Dynamics in a Pure Encounter Complex of Two Proteins Studied by Solution Scattering and Paramagnetic NMR Spectroscopy. 6395–6403 (2008).

45. von Sonntag, C. on. *The Chemical Basis of Radiation Biology*. (London:Taylor & Francis, 1987).

46. Shimazu, F., Kumta, U. S. & Tappel, A. L. Radiation Damage to Methionine and its Derivatives. *Radiat. Res.* **22,** 276–287 (1964).

47. Lind, S. C. Actions of Radiations on Living Cells. *J. Phys. Chem.* **51,** 1451–1451 (1947).

48. Christensen, D. M., Iddins, C. J. & Sugarman, S. L. Ionizing radiation injuries and illnesses. *Emerg. Med. Clin. North Am.* **32,** 245–265 (2014).

49. Bury, C. *et al.* Radiation damage to nucleoprotein complexes in macromolecular crystallography. *J. Synchrotron Radiat.* **22,** 213–224 (2015).

50. Wlodawer, A., Minor, W., Dauter, Z. & Jaskolski, M. Protein crystallography for aspiring crystallographers or how to avoid pitfalls and traps in macromolecular structure determination. *FEBS J.* **280,** 5705–5736 (2013).

51. Skou, S., Gillilan, R. E. & Ando, N. Synchrotron-based small-angle X-ray scattering of proteins in solution. *Nat. Protoc.* **9,** 1727–39 (2014).

52. Kuwamoto, S., Akiyama, S. & Fujisawa, T. Radiation damage to a protein solution, detected by synchrotron X-ray small-angle scattering: Dose-related considerations and suppression by cryoprotectants. *J. Synchrotron Radiat.* **11,** 462–468 (2004).

53. Rodacka, A. The effect of radiation-induced reactive oxygen species (ROS) on the structural and functional properties of yeast alcohol dehydrogenase (YADH). *Int. J. Radiat. Biol.* **92,** 11–23 (2016).

54. Jeffries, C. M., Graewert, M. A., Svergun, D. I. & Blanchet, C. E. Limiting radiation damage for high-brilliance biological solution scattering: practical experience at the EMBL P12 beamline PETRAIII. *J. Synchrotron Radiat.* **22,** 273–279 (2015).

55. Hopkins, J. B. & Thorne, R. E. Quantifying radiation damage in biomolecular small-angle X-ray scattering. *J. Appl. Crystallogr.* **49,** 880–890 (2016).

56. Franke, D., Jeffries, C. M. & Svergun, D. I. Correlation Map, a goodness-of-fit test for one-dimensional X-ray scattering spectra. *Nat. Methods* **12,** 419–422 (2015).

57. Kirby, N. *et al.* Improved radiation dose efficiency in solution SAXS using a sheath flow sample environment. *Acta Crystallogr. Sect. D Struct. Biol.* **72,** 1254–1266 (2016).

58. Meisburger, S. P. *et al.* Breaking the radiation damage limit with cryo-SAXS. *Biophys. J.* **104,** 227–236 (2013).

59. Meents, A., Gutmann, S., Wagner, A. & Schulze-briese, C. Origin and temperature dependence of radiation damage in biological samples at cryogenic temperatures. *PNAS* **107,** 3–8 (2010).

60. Warkentin, M. *et al.* Global radiation damage: Temperature dependence, time dependence and how to outrun it. *J. Synchrotron Radiat.* **20,** 7–13 (2013).

61. Crosas, E. *et al.* Uridine as a new scavenger for synchrotron-based structural biology techniques. *J. Synchrotron Radiat.* **24,** 53–62 (2017).

62. Garman, E. F. Radiation damage in macromolecular crystallography: what is it and why should we care? *Acta Crystallogr. Sect. D Biol. Crystallogr.* **66,** 339–351 (2010).

63. Weinert, T. *et al.* Serial millisecond crystallography for routine room-temperature structure determination at synchrotrons. *Nat. Commun.* **8,** (2017).

64. Polsinelli, I. *et al.* Comparison of helical scan and standard rotation methods in single-crystal X-ray data collection strategies. *J. Synchrotron Radiat.* **24,** 42–52 (2017).

65. Garman, E. F. & Owen, R. L. Cryocooling and radiation damage in macromolecular crystallography. *Acta Crystallogr. Sect. D Biol. Crystallogr.* **62,** 32–47 (2006).

66. Jeffries, C. M. *et al.* Preparing monodisperse macromolecular samples for successful biological small-angle X-ray and neutron-scattering experiments. *Nat. Protoc.* **11,** 2122–2153 (2016).

67. Allan, E. G., Kander, M. C., Carmichael, I. & Garman, E. F. To scavenge or not to scavenge, that is STILL the question. *J. Synchrotron Radiat.* **20,** 23–36 (2013).

68. Barker, A. I., Southworth-Davies, R. J., Paithankar, K. S., Carmichael, I. & Garman, E. F. Room-temperature scavengers for macromolecular crystallography: Increased lifetimes and modified dose dependence of the intensity decay. *J. Synchrotron Radiat.* **16,** 205–216 (2009).

69. Gerschman, R., Gilbert, D. L., Nye, S. W., Dwyer, P. & Fenn, W. O. Oxygen Poisoning and X-irradiation: A Mechanism in Common. *Science (80-.).* **119,** 26–29 (1954).

70. Halliwell, B. & Gutteridge, J. M. C. *Free Radicals in Biology and Medicine*. *Mycological Research* (Press, Oxford university, 2007).

71. D'Autréaux, B. & Toledano, M. B. ROS as signalling molecules: Mechanisms that generate specificity in ROS homeostasis. *Nat. Rev. Mol. Cell Biol.* **8,** 813–824 (2007).

72. Paiva, C. N. & Bozza, M. T. Are Reactive Oxygen Species Always Detrimental to Pathogens? *Antioxid. Redox Signal.* **20,** 1000–1037 (2013).

73. Cadenas, E. & Davies, K. J. A. Mitochonrial free radical generation,oxidative stress,and aging. *Free Radic. Biol. Med.* **29,** 222–230 (2000).

74. Babior, B. M., Lambeth, J. D. & Nauseef, W. The neutrophil NADPH oxidase. *Arch. Biochem. Biophys.* **397,** 342–344 (2002).

75. Sevier, C. S. & Kaiser, C. A. Ero1 and redox homeostasis in the endoplasmic reticulum. *Biochim. Biophys. Acta - Mol. Cell Res.* **1783,** 549–556 (2008).

76. Chung, H. Y. *et al.* Xanthine dehydrogenase/xanthine oxidase and oxidative stress. *Age (Omaha).* **20,** 127–140 (1997).

77. Coon, M. J., Ding, X., Pernecky, S. J. & Vaz, A. D. N. Cytochrome P450: progress and predictions. *FASEB* **6,** 669–673 (1992).

78. Kanti Das, T., Wati, M. R. & Fatima-Shad, K. Oxidative Stress Gated by Fenton and Haber Weiss Reactions and Its Association With Alzheimer's Disease. *Arch. Neurosci.* **2,** (2014).

79. Imlay, J. A. Iron-sulphur clusters and the problem with oxygen. *Mol. Microbiol.* **59,** 1073–1082 (2006).

80. Imlay, J. A. The molecular mechanisms and physiological consequences of oxidative stress: Lessons from a model bacterium. *Nat. Rev. Microbiol.* **11,** 443–454 (2013).

81. Sharma, P., Jha, A. B., Dubey, R. S. & Pessarakli, M. Reactive Oxygen Species, Oxidative Damage, and Antioxidative Defense Mechanism in Plants under Stressful Conditions. *J. Bot.* **2012,** 1–26 (2012).

82. Mittler, R. ROS Are Good. *Trends Plant Sci.* **22,** 11–19 (2017).

83. Giorgio, M., Mirella, T., Enrica, M. & Giuseppe Pelicci, P. Hydrogen peroxide: a metabolic by-product or a common mediator of ageing signals? *Nat Rev Mol Cell Biol.* **8,** 722–728. (2007).

84. Cabiscol, E., Tamarit, J. & Ros, J. Oxidative stress in bacteria and protein damage by reactive oxygen species. *Int. Microbiol.* **3,** 3–8 (2000).

85. Ezraty, B., Gennaris, A., Barras, F. & Collet, J.-F. Oxidative stress, protein damage and repair in bacteria. *Nat. Rev. Microbiol.* **15,** 385–396 (2017).

86. Daly, M. J. *et al.* Small-molecule antioxidant proteome-shields in Deinococcus radiodurans. *PLoS One* **5,** 10–15 (2010).

87. Daly, M. J. Death by protein damage in irradiated cells. *DNA Repair (Amst).* **11,** 12–21 (2012).

88. Slade, D. & Radman, M. *Oxidative Stress Resistance in Deinococcus radiodurans*. *Microbiology and Molecular Biology Reviews* **75,** (2011).

89. Greenstock, B. Y. C. L. Pulse Radiolysis Studies. (1969).

90. Barker, A. I., Southworth-Davies, R. J., Paithankar, K. S., Carmichael, I. & Garman, E. F. Room-temperature scavengers for macromolecular crystallography: Increased lifetimes and modified dose dependence of the intensity decay. *J. Synchrotron Radiat.* **16,** 205–216 (2009).

91. De La Mora, E., Carmichael, I. & Garman, E. F. Effective scavenging at cryotemperatures: Further increasing the dose tolerance of protein crystals. *J. Synchrotron Radiat.* **18,** 346–357 (2011).

92. Juanhuix, J. *et al.* Developments in optics and performance at BL13-XALOC, the macromolecular crystallography beamline at the Alba Synchrotron. *J. Synchrotron Radiat.* **21,** 679–689 (2014).

93. Kabsch, W. *XDS*. *Acta Crystallogr. Sect. D Biol. Crystallogr.* **66,** 125–132 (2010).

94. Diederichs, K. Some aspects of quantitative analysis and correction of radiation damage. *Acta Crystallogr. D. Biol. Crystallogr.* **62,** 96–101 (2006).

95. Evans, P. Scaling and assessment of data quality. *Acta Crystallogr. Sect. D Biol. Crystallogr.* **62,** 72–82 (2006).

96. French, S. & Wilson, K. On the treatment of negative intensity observations. *Acta Crystallogr. Sect. A* **34,** 517–525 (1978).

97. Dong, J. *et al.* Bound-solvent structures for microgravity-, ground control-, gel- and microbatch-grown hen egg-white lysozyme crystals at 1.8 ?? resolution. *Acta Crystallogr. Sect. D Biol. Crystallogr.* **55,** 745–752 (1999).

98. Murshudov, G. N., Vagin, A. A. & Dodson, E. J. Refinement of macromolecular structures by the maximum-likelihood method. *Acta Crystallogr. Sect. D Biol. Crystallogr.* **53,** 240–255 (1997).

99. Emsley, P., Lohkamp, B., Scott, W. G. & Cowtan, K. Features and development of Coot. *Acta Crystallogr. D. Biol. Crystallogr.* **66,** 486–501 (2010).

100. Howell, P. L. Identification of heavy-atom derivatives by normal probability methods. *J. Appl. Crystallogr.* **25,** 81–86 (1992).

101. Southworth-Davies, R. J., Medina, M. a, Carmichael, I. & Garman, E. F. Observation of decreased radiation damage at higher dose rates in room temperature protein crystallography. *Structure* **15,** 1531–41 (2007).

102. Project, C. C. The CCP4 suite: Programs for protein crystallography. *Acta Crystallogr. Sect. D Biol. Crystallogr.* **50,** 760–763 (1994).

103. Kmetko, J., Husseini, N. S., Naides, M., Kalinin, Y. & Thorne, R. E. Quantifying X-ray radiation damage in protein crystals at cryogenic temperatures. *Acta Crystallogr. Sect. D Biol. Crystallogr.* **62,** 1030–1038 (2006).

104. Warkentin, M. *et al.* Global radiation damage at 300 and 260 K with dose rates approaching 1 MGy s \n -1. *Acta Crystallogr. Sect. D Biol. Crystallogr.* **68,** 124–133 (2012).

105. Kikhney, A. G. & Svergun, D. I. A practical guide to small angle X-ray scattering (SAXS) of flexible and intrinsically disordered proteins. *FEBS Lett.* **589,** 2570–2577 (2015).

106. Singh, R. K. *et al.* Small-angle X-ray Scattering Studies of the Oligomeric State and Quaternary Structure of the Trifunctional Proline Utilization A (PutA) Flavoprotein from Escherichia coli. *J. Biol. Chem.* **286,** 43144–43153 (2011).

107. Cooley, R. B., Donnell, J. P. O. & Sondermann, H. Coincidence detection and bi-directional transmembrane signaling control a bacterial second messenger receptor. *Elife* 1–19 (2016). doi:10.7554/eLife.21848

108. Lawson, M. R., Dyer, K. & Berger, J. M. Ligand-induced and small-molecule control of substrate loading in a hexameric helicase. *PNAS* **113,** 13714–13719 (2016).

109. Badmalia, M. D., Singh, S. & Garg, R. Visualizing Temperature Mediated Activation of Gelsolin and Its Deactivation By Pip 2 : A Saxs Based Study. *Sci. Rep.* 1–15 (2017). doi:10.1038/s41598-017-04975-0

110. Jeffries, C. M., Graewert, M. A. & Svergun, D. I. Limiting radiation damage for high-brilliance biological solution scattering : practical experience at the EMBL P12 beamline PETRAIII Limiting radiation damage for high-brilliance biological solution scattering : practical experience at the EMBL P12 beaml. 273–279 (2015). doi:10.1107/S1600577515000375

111. Zhang, F. *et al.* Protein Interactions Studied by SAXS : Effect of Ionic Strength and Protein Concentration for BSA in Aqueous Solutions. *J. Phys. Chem. B* **111,** 251–259 (2007).

112. Castellví, A. *et al.* Efficacy of aldose reductase inhibitors is affected by oxidative stress induced under X-ray irradiation. *Sci. Rep.* **9,** 3177 (2019).

113. Sadqi, M. *et al.* The native state conformational ensemble of the SH3 domain from α- spectrin. *Biochemistry* **38,** 8899–8906 (1999).

114. Petoukhov, M. V. *et al.* New developments in the ATSAS program package for small-angle scattering data analysis. *J. Appl. Crystallogr.* **45,** 342–350 (2012).

115. Konarev, P. V., Volkov, V. V., Sokolova, A. V., Koch, M. H. J. & Svergun, D. I. PRIMUS: A Windows PC-based system for small-angle scattering data analysis. *J. Appl. Crystallogr.* **36,** 1277–1282 (2003).

116. Franke, D., Jeffries, C. M. & Svergun, D. I. Correlation Map, a goodness-of-fit test for one-dimensional X-ray scattering spectra. *Nat. Methods* **12,** 419–22 (2015).

117. Svergun, D. I. Determination of the regularization parameter in indirect-transform methods using perceptual criteria. *J. Appl. Crystallogr.* **25,** 495–503 (1992).

118. Konarev, P. V. & Svergun, D. I. A posteriori determination of the useful data range for small-angle scattering experiments on dilute monodisperse systems. *IUCrJ* **2,** 352–360 (2015).

119. Svergun, D. I. Restoring low resolution structure of biological macromolecules from solution scattering using simulated annealing. *Biophys. J.* **76,** 2879–86 (1999).

120. Kozin, M. B. & Svergun, D. I. Automated matching of high- and low-resolution structural models. *J. Appl. Crystallogr.* **34,** 33–41 (2001).

121. Zeldin, O. B., Gerstel, M. & Garman, E. F. RADDOSE-3D : time- and space-resolved modelling of dose in macromolecular crystallography. 1225–1230 (2013). doi:10.1107/S0021889813011461

122. Konarev, P. V. & Svergun, D. I. A posteriori determination of the useful data range for small-angle scattering experiments on dilute monodisperse systems. *IUCrJ* **2,** 352–360 (2015).

123. Rambo, R. P. & Tainer, J. A. Accurate assessment of mass, models and resolution by small-angle scattering. *Nature* **496,** 477–481 (2013).

124. Brooks-Bartlett, J. C. *et al.* Development of tools to automate quantitative analysis of radiation damage in SAXS experiments. *J. Synchrotron Radiat.* **24,** 63–72 (2017).

125. Das, T., Häring, M., Haldar, D. & Díaz Díaz, D. Phenylalanine and derivatives as versatile low-molecular-weight gelators: Design, structure and tailored function. *Biomater. Sci.* **6,** 38–59 (2018).

126. Draper, E. R. & Adams, D. J. Low-Molecular-Weight Gels: The State of the Art. *Chem* **3,** 390–410 (2017).

127. Fleming, S. & Ulijn, R. V. Design of nanostructures based on aromatic peptide amphiphiles. *Chem. Soc. Rev.* **43,** 8150–8177 (2014).

128. Dasgupta, A., Mondal, J. H. & Das, D. Peptide hydrogels. *RSC Adv.* **3,** 9117–9149 (2013).

129. Adler-Abramovich, L. & Gazit, E. The physical properties of supramolecular peptide assemblies: from building block association to technological applications. *Chem. Soc. Rev.* **43,** 7236 (2014).

130. Tao, K., Levin, A., Adler-Abramovich, L. & Gazit, E. Fmoc-modified amino acids and short peptides: Simple bio-inspired building blocks for the fabrication of functional materials. *Chem. Soc. Rev.* **45,** 3935–3953 (2016).

131. Zhou, M. *et al.* Self-assembled peptide-based hydrogels as scaffolds for anchorage-dependent cells. *Biomaterials* **30,** 2523–2530 (2009).

132. Fichman, G. *et al.* Seamless Metallic Coating and Surface Adhesion of Self-Assembled Bioinspired Nanostructures Based. *ACS Nano* 7220–7228 (2014).

133. Conejero-Muriel, M. *et al.* Influence of the chirality of short peptide supramolecular hydrogels in protein crystallogenesis. *Chem. Commun.* **51,** 3862–3865 (2015).

134. Conejero-Muriel, M., Contreras-Montoya, R., Díaz-Mochón, J. J., Álvarez De Cienfuegos, L. & Gavira, J. A. Protein crystallization in short-peptide supramolecular hydrogels: A versatile strategy towards biotechnological composite materials. *CrystEngComm* **17,** 8072–8078 (2015).

135. Gavira, J. A. & García-ruiz, J. M. Agarose as crystallisation media for proteins II : trapping of gel fibres into the crystals. *Acta Crystallogr. Sect. D* **58,** 1653–1656 (2002).

136. Gavira, J. A., Van Driessche, A. E. S. & Garcia-Ruiz, J. M. Growth of ultrastable protein-silica composite crystals. *Cryst. Growth Des.* **13,** 2522–2529 (2013).

137. Alvarez de Cienfuegos, L., Gavira, J. A., Diaz-Mochon, J. J., Conejero-Muriel, M. T. & Contreras-Montoya, R. *Pharmaceutically active protein crystals grown in-situ within a*

hydrogel. (2017).

138. Contreras-Montoya, R. *et al.* Catalytic and Electron Conducting Carbon Nanotube–Reinforced Lysozyme Crystals. *Adv. Funct. Mater.* **29,** 1–10 (2019).

139. Mahler, A., Reches, M., Rechter, M., Cohen, S. & Gazit, E. Rigid, self-assembled hydrogel composed of a modified aromatic dipeptide. *Adv. Mater.* **18,** 1365–1370 (2006).

140. McCoy, A. J. *et al.* Phaser crystallographic software. *J. Appl. Crystallogr.* **40,** 658–674 (2007).

141. Adams, P. D. *et al.* PHENIX: A comprehensive Python-based system for macromolecular structure solution. *Acta Crystallogr. Sect. D Biol. Crystallogr.* **66,** 213–221 (2010).

142. Read, R. J. & Schierbeek, A. J. A phased translation function. *J. Appl. Crystallogr.* **21,** 490–495 (1988).

143. Schrodinger. The PyMOL Molecular Graphics System. (2011).

144. Sawaya, M. R. *et al.* Characterization of WY 14,643 and its Complex with Aldose Reductase. *Sci. Rep.* **6,** 34394 (2016).

145. Chatzopoulou, M., Alexiou, P., Kotsampasakou, E. & Demopoulos, V. J. Novel aldose reductase inhibitors: a patent survey (2006 – present). *Expert Opin. Ther. Pat.* **22,** 1303–1323 (2012).

146. Thiagarajan, D. *et al.* Aldose Reductase Acts as a Selective Derepressor of PPARγ and the Retinoic Acid Receptor. *Cell Rep.* **15,** 181–196 (2016).

147. Bornfeldt, K. E. & Tabas, I. Insulin resistance, hyperglycemia, and atherosclerosis. *Cell Metab.* **14,** 575–585 (2011).

148. Brownlee, M. Biochemistry and molecular cell biology of diabetic complications. *Nature* **414,** 813–820 (2001).

149. Nishikawa, T. *et al.* Normalizing mitochondrial superoxide production blocks three pathways of hyperglycaemic damage. *Nature* **404,** 787–790 (2000).

150. Maccari, R. & Ottanà, R. Targeting Aldose Reductase for the Treatment of Diabetes Complications and Inflammatory Diseases: New Insights and Future Directions. *J. Med. Chem.* (2014).

151. Ameziane-El-Hassani, R., Schlumberger, M. & Dupuy, C. NADPH oxidases: new actors in

thyroid cancer? *Nat. Rev. Endocrinol.* **12,** 485–494 (2016).

152. Hesselink, M. K. C., Schrauwen-Hinderling, V. & Schrauwen, P. Skeletal muscle mitochondria as a target to prevent or treat type 2 diabetes mellitus. *Nat. Rev. Endocrinol.* **12,** 633–645 (2016).

153. Das, B. & Srivastava, S. K. Activation of Aldose Reductase from Human Tissues. *Diabetes* **34,** 1145–1151 (1985).

154. Srivastava, S. K., Ansari, N. H., Hair, G. A., Awasthi, S. & Das, B. Activation of human erythrocyte, brain, aorta, muscle, and ocular tissue aldose reductase. *Metabolism* **35,** 114–118 (1986).

155. Grimshaw, C. E. & Lai, C. J. Oxidized aldose reductase: In vivo factor, not in vitro artifact. *Arch. Biochem. Biophys.* **327,** 89–97 (1996).

156. Borhani, D. W., Harter, T. M. & Petrash, J. M. The crystal structure of the aldose reductase·NADPH binary complex. *J. Biol. Chem.* **267,** 24841–24847 (1992).

157. Balendiran, G. K. *et al.* The Role of Cys-298 in Aldose Reductase Function. *J. Biol. Chem.* **286,** 6336–6344 (2011).

158. Brownlee, J. M., Carlson, E., Milne, A. C., Pape, E. & Harrison, D. H. T. Structural and thermodynamic studies of simple aldose reductase – inhibitor complexes. *Bioorg. Chem.* **34,** 424–444 (2006).

159. Cappiello, M. *et al.* Specifically targeted modification of human aldose reductase by physiological disulfides. *J. Biol. Chem.* **271,** 33539–33544 (1996).

160. Corso, A. Del *et al.* Site-specific inactivation of aldose reductase by 4-hydroxynonenal. *Arch. Biochem. Biophys.* **350,** 245–248 (1998).

161. Baba, S. P., Wetzelberger, K., Hoetker, J. D. & Bhatnagar, A. Posttranslational glutathiolation of aldose reductase (AKR1B1): a possible mechanism of protein recovery from S-nitrosylation. *Chem. Biol. Interact.* **178,** 250–8 (2009).

162. Díez-Dacal, B. *et al.* Molecular Interactions and Implications of Aldose Reductase Inhibition by PGA1 and Clinically Used Prostaglandins. *Mol. Pharmacol.* **89,** 42–52 (2016).

163. Srivastava, S. K. & Hair, G. A. Activated and unactivated forms of human erythrocite aldose reductase. *PNAS* **82,** 7222–7226 (1985).

164. D'Autréaux, B. & Toledano, M. B. ROS as signalling molecules: Mechanisms that generate specificity in ROS homeostasis. *Nat. Rev. Mol. Cell Biol.* **8,** 813–824 (2007).

165. Rotilio, G., Bray, R. C. & Fielden, E. M. A pulse radiolysis study of superoxide dismutase. *Biochim. Biophys. Acta* **268,** 605–609 (1972).

166. Hearn, A. S. *et al.* Kinetic analysis of product inhibition in human manganese superoxide dismutase. *Biochemistry* **40,** 12051–12058 (2001).

167. Moore, J. S., Sakhri, M. & Butler, J. The radiolysis of protein A. *Radiat. Phys. Chem.* **58,** 331–339 (2000).

168. Gębicka, L. & Gębicki, J. L. Redox transformations in peroxidases studied by pulse radiolysis technique. *Int. J. Radiat. Appl. Instrumentation. Part* **39,** 113–116 (1992).

169. Rodacka, A., Serafin, E. & Puchala, M. Efficiency of superoxide anions in the inactivation of selected dehydrogenases. *Radiat. Phys. Chem.* **79,** 960–965 (2010).

170. Rodacka, A. The effect of radiation-induced reactive oxygen species (ROS) on the structural and functional properties of yeast alcohol dehydrogenase (YADH). *Int. J. Radiat. Biol.* **92,** 11–23 (2016).

171. Watanabe, R. & Saito, K. Monte Carlo simulation of water radiolysis in oxygenated condition for monoenergetic electrons from 100 eV to 1 MeV. *Radiat. Phys. Chem.* **62,** 217–228 (2001).

172. Ao, S. *et al.* Characterization of a novel aldose reductase inhibitor, FR74366, and its effects on diabetic cataract and neuropathy in the rat. *Metab. - Clin. Exp.* **40,** 77–87 (1991).

173. Ruiz, F. X. *et al.* Structural Determinants of the Selectivity of 3-Benzyluracil-1-acetic Acids toward Human Enzymes Aldose Reductase and AKR1B10. *ChemMedChem* **10,** 1989–2003 (2015).

174. Terashima, H. *et al.* Effects of a new aldose reductase inhibitor on various tissues in vitro. *J. Pharmacol. Exp. Ther.* **229,** 226–230 (1984).

175. K., S., F., B. & S., F. N-[[5-(trifluoromethyl)-6-methoxy-1-naphthalenyl]thioxomethyl]-N-methylgl ycine (Tolrestat), a potent, orally active aldose reductase inhibitor. *J. Med. Chem.* **27,** 255–256 (1984).

176. Kabsch, W. *XDS*. *Acta Crystallogr. Sect. D Biol. Crystallogr.* **66,** 125–132 (2010).

177. Biadene, M. *et al.* The atomic resolution structure of human aldose reductase reveals that rearrangement of a bound ligand allows the opening of the safety-belt loop. *Acta Crystallogr. Sect. D Biol. Crystallogr.* **63,** 665–672 (2007).

178. Sheldrick, G. M. Crystal structure refinement with SHELXL. *Acta Crystallogr. Sect. C Struct. Chem.* **71,** 3–8 (2015).

179. Emsley, P., Lohkamp, B., Scott, W. G. & Cowtan, K. Features and development of Coot. *Acta Crystallogr. D. Biol. Crystallogr.* **66,** 486–501 (2010).

180. Kabsch, W. A solution for the best rotation to relate two sets of vectors. *Acta Crystallogr. Sect. A* **32,** 922–923 (1976).

181. Round, A. *et al.* BioSAXS Sample Changer: A robotic sample changer for rapid and reliable high-throughput X-ray solution scattering experiments. *Acta Crystallogr. Sect. D Biol. Crystallogr.* **71,** 67–75 (2015).

182. Grant, T. D. *et al.* The accurate assessment of small-angle X-ray scattering data. *Acta Crystallogr. Sect. D Biol. Crystallogr.* **71,** 45–56 (2015).

183. Konarev, P. V., Volkov, V. V., Sokolova, A. V., Koch, M. H. J. & Svergun, D. I. PRIMUS: A Windows PC-based system for small-angle scattering data analysis. *J. Appl. Crystallogr.* **36,** 1277–1282 (2003).

184. Zeldin, O. B., Gerstel, M. & Garman, E. F. *RADDOSE-3D* : time- and space-resolved modelling of dose in macromolecular crystallography. *J. Appl. Crystallogr.* **46,** 1225–1230 (2013).

185. Ellman, G. L. Tissue sulfhydryl groups. *Arch. Biochem. Biophys.* **82,** 70–77 (1959).

186. Jeffries, C. M., Graewert, M. A., Svergun, D. I. & Blanchet, C. E. Limiting radiation damage for high-brilliance biological solution scattering: Practical experience at the EMBL P12 beamline PETRAIII. in *Journal of Synchrotron Radiation* **22,** 273–279 (International Union of Crystallography, 2015).

187. Nakano, T. & Petrash, J. M. Kinetic and Spectroscopic Evidence for Active Site Inhibition of Human Aldose. *Biochemistry* **36,** 11196–11202 (1996).

188. Tang, W. H., Martin, K. A. & Hwa, J. Aldose reductase, oxidative stress, and diabetic mellitus. *Front. Pharmacol.* **3,** 1–8 (2012).

189. Juanhuix, J. *et al.* Developments in optics and performance at BL13-XALOC, the macromolecular crystallography beamline at the Alba Synchrotron. *J. Synchrotron Radiat.* **21,** 679–689 (2014).

190. Kuwamoto, S., Akiyama, S. & Fujisawa, T. Radiation damage to a protein solution, detected by synchrotron X-ray small-angle scattering: dose-related considerations and suppression by cryoprotectants. *J. Synchrotron Radiat.* **11,** 462–8 (2004).

191. Garman, E. F. Radiation damage in macromolecular crystallography: What is it and why do we care? *Acta Crystallogr. Sect. D* **66,** 339–351 (2010).

192. Penning, T. M. The aldo-keto reductases (AKRs): Overview. *Chem. Biol. Interact.* **234,** 236–246 (2014).

193. Lide, D. R. CRC Handbook of Chemistry and Physics, 84th Edition, 2003-2004. *Handb. Chem. Phys.* **53,** 2616 (2003).

194. Kaiserova, K. *et al.* Redox activation of aldose reductase in the ischemic heart. *J. Biol. Chem.* **281,** 15110–15120 (2006).

195. Kaiserova, K., Tang, X. L., Srivastava, S. & Bhatnagar, A. Role of nitric oxide in regulating aldose reductase activation in the ischemic heart. *J. Biol. Chem.* **283,** 9101–9112 (2008).

196. Pastina, B. & LaVerne, J. a. Hydrogen peroxide production in the radiolysis of water with heavy ions. *J. Phys. Chem. A* **103,** 1592–1597 (1999).

197. Sutton, K. A. *et al.* Insights into the mechanism of X-ray-induced disulfide-bond cleavage in lysozyme crystals based on EPR, optical absorption and X-ray diffraction studies. *Acta Crystallogr. D. Biol. Crystallogr.* **69,** 2381–94 (2013).

198. Carpentier, P., Royant, A., Weik, M. & Bourgeois, D. Raman-Assisted Crystallography Suggests a Mechanism of X-Ray-Induced Disulfide Radical Formation and Reparation. *Structure* **18,** 1410–1419 (2010).

199. Garman, E. F. & Weik, M. Radiation damage to biological macromolecules: Some answers and more questions. *J. Synchrotron Radiat.* **20,** 1–6 (2013).

200. Harrison, D. H. T., Bohren, K. M., Petsko, G. A., Ringe, D. & Gabbay, K. H. The Alrestatin Double-Decker : Binding of Two Inhibitor Molecules to Human Aldose Reductase Reveals a New Specificity Determinant. *Biochemistry* **36,** 16134–16140 (1997).

201. Hese, S. V. *et al.* Antidiabetic and allied biochemical roles of new chromeno-pyrano pyrimidine compounds: synthesis, in vitro and in silico analysis. *Med. Chem. Res.* **26,** 805–818 (2017).

202. Sun, M. *et al.* Probing the Dipeptide-Based Supramolecular Assembly as an Efficient Camptothecin Delivering Carrier for Cancer Therapy: Computational Simulations and Experimental Validations. *Nanoscale* **11,** 3864–3876 (2019).

203. Sutton, S. *et al.* Controlled release from modified amino acid hydrogels governed by molecular size or network dynamics. *Langmuir* **25,** 10285–10291 (2009).

204. Gao, Y. *et al.* Supramolecular Hydrogel of a d -Amino Acid Dipeptide for Controlled Drug Release in Vivo † . *Langmuir* **25,** 8419–8422 (2009).

205. Lorber, B. *et al.* Crystal growth of proteins, nucleic acids, and viruses in gels. *Prog. Biophys. Mol. Biol.* **101,** 13–25 (2009).

206. Gavira, A., Csic-ugr, I. & Palmeras, A. De. Current trends in protein crystallization. **602,** 3–11 (2016).

207. Garcia, A. M., Kurbasic, M., Kralj, S., Melchionna, M. & Marchesan, S. A biocatalytic and thermoreversible hydrogel from a histidine-containing tripeptide. *Chem. Commun.* **53,** 8110–8113 (2017).

208. Tan, M. *et al.* Supramolecular bimetallogels: A nanofiber network for bimetal/nitrogen co-doped carbon electrocatalysts. *J. Mater. Chem. A* **6,** 8227–8232 (2018).

209. Bai, S., Ren, P., Wang, A., Yan, X. & Li, J. One-step co-assembly method to fabricate photosensitive peptide nanoparticles for two-photon photodynamic therapy. *Chem. Commun.* (2019). doi:10.1039/c9cc00025a

210. Sakala, G. P. & Reches, M. Peptide-Based Approaches to Fight Biofouling. *Adv. Mater. Interfaces* **5,** 1–26 (2018).

211. Bury, C. S. & Garman, E. F. RIDL: A tool to investigate radiation-induced density loss. *J. Appl. Crystallogr.* **51,** 952–962 (2018).